INVESTIGATING THE EFFECTS OF DEHYDRATION ON THE

CONFORMATIONAL PREFERENCES OF BIOMOLECULES DURING THE

FINAL STAGES OF ELECTROSPRAY IONIZATION

A Dissertation

by

KELLY ANNE SERVAGE

Submitted to the Office of Graduate and Professional Studies of
Texas A&M University
in partial fulfillment of the requirements for the degree of

DOCTOR OF PHILOSOPHY

Chair of Committee,	David H. Russell
Committee Members,	Simon W. North
	Emile A. Schweikert
	Paul D. Straight
Head of Department,	Simon W. North

August 2016

Major Subject: Chemistry

ABSTRACT

Electrospray ionization (ESI) combined with ion mobility-mass spectrometry (IM-MS) provides a means to directly measure the three-dimensional shape(s) of intact biomolecular ions allowing for the structural investigation of biologically-important systems. Studies of gas-phase biomolecules remove the complicating effects of solute-solvent interactions, but understanding the conformational preferences of ions as they transition from solution to the gas phase is of critical importance to the development of "native" mass spectrometry. A number of recent studies utilizing ESI have demonstrated that gas-phase peptide and protein ions can retain memory of their solution-phase counterparts. However, the preservation of native structures is dependent on an ensemble of stabilizing interactions, specifically the interplay between inter- and intramolecular interactions that afford stability to ions. Cryogenic ion mobility-mass spectrometry takes advantage of the freeze-drying capabilities of ESI and a cold IM drift cell (80 K) to preserve extensively solvated ions of the type $[M + xH]^{x+} (H_2O)_n$, where n can vary from zero to several hundred. This affords an experimental approach for tracking the structural evolution of hydrated biomolecules en route to forming solvent-free gas-phase ions.

Studies of small ions, including protonated water clusters and alkyl diammonium cations, reveal structural transitions associated with the development of the H-bond network of water molecules surrounding the charge carrier(s). When extended to larger

peptide ions, results show that water networks are highly dependent on the charge-carrying species within the cluster. Studies on the neuropeptide substance P illustrate the ability to elucidate information about heterogeneous ion populations. Results showed that a kinetically-trapped conformer was stabilized by a combination of solvation and specific intramolecular interactions. However, upon desolvation, the kinetically-trapped conformer rearranges to form a thermodynamically-favored gas-phase ion conformation. Finally, extension of this approach to larger biomolecules revealed a water-mediated protein-binding event associated with dehydration of ubiquitin ions. Cryo-IM-MS adds a new dimension to studies of biomolecules in the ability to monitor snapshots of the structural evolution of ions during the transition from solution to gas phase, and provides insight into the intricate interplay between competing effects that dictate conformational preferences.

ACKNOWLEDGEMENTS

NOMENCLATURE

AAD	acceptor acceptor donor (referring to hydrogen bonding)
ATD	arrival time distribution
BK	Bradykinin
CCS	Collision Cross Section
CID	Collision Induced Dissociation
CRM	Charge Residue Model
Cryo-IM-MS	Cryogenic Ion Mobility-Mass Spectrometry
CT	C-terminus
D^+	dimer ion
DAD	1,10-diaminodecane
DAH	1,7-diaminoheptane
DAO	1,8-diaminooctane
DC IG	direct current ion guide
DFT	Density Functional Theory
DMA	Differential Mobility Analysis
e	elementary charge (1.602×10^{-19} C)
E	applied electric field
E/N	field strength in Townsend units
ESI	Electrospray Ionization
FAIMS	High-Field Asymmetric Waveform Ion Mobility Spectrometry

GS	Gramicidin S
H-bond	hydrogen bond
IEM	Ion Evaporation Model
IM	Ion Mobility
IMS	Ion Mobility Spectrometry
IM-MS	Ion Mobility-Mass Spectrometry
IR	Infrared Spectroscopy
K	ion mobility parameter
K_0	reduced mobility coefficient
k_B	Boltzmann constant
L	drift tube length
M^+	monomer ion
MALDI	Matrix-Assisted Laser Desorption Ionization
MeOH	Methanol
MCP	microchannel plate
MDS	Molecular Dynamics Simulations
MS	Mass Spectrometry
m/z	mass-to-charge ratio
N	buffer gas number density
NMR	Nuclear Magnetic Resonance
N-state	native state (of a protein)
NT	N-terminus

P	drift gas pressure
PF IF	Periodic Focusing Ion Funnel
QM	Quantum Mechanics
R	resolving power
SP	Substance P
SP_M	Substance P mutant
T	drift gas temperature
t_d	ion drift time
TOF	time-of-flight (mass spectrometer)
TWIMS	Traveling Wave Ion Mobility Spectrometry
μ	reduced mass of ion-neutral pair
V	Voltage
υ_d	average drift velocity
z	ion charge state
Ω	Collision Cross Section

TABLE OF CONTENTS

LIST OF FIGURES

Page

LIST OF TABLES

1. INTRODUCTION AND OVERVIEW OF METHODS

1.1 Overview of Ion Mobility-Mass Spectrometry

Ion mobility spectrometry (IMS) is a gas-phase separation technique commonly used to characterize ions based on three-dimensional shape and size. The initial theory of IMS dates back to the early 20th century with work by Langevin[1] and Thomson,[2] but the successful progress of IMS as an analytical tool has developed slowly up until the past few decades. The renewed interest in the technique coincides with technological advances to instrumentation and methods pertaining to gas-phase ion chemistry, allowing the capabilities of IMS as a structural probe to be recognized.[3-7] Typical IMS experiments involve the measurement of an ion's velocity through a drift region under the influence of a weak electric field. During this drift, an ion undergoes collisions with a neutral background gas, providing a means for separation on the basis of size/shape and charge state. Coupling IMS to mass spectrometry (MS) allows for the mass-to-charge (*m/z*) analysis of mobility-separated ions, creating a powerful hybrid technique (IM-MS) for structural studies of gas-phase ions. The separation capabilities of IM provide a way to differentiate between ions of the same *m/z* but different structural motifs, as shown in the theoretical data set in **Figure 1**. Thus, IM-MS provides a means to identify molecular ions, ranging from small molecules to large protein complexes, by their molecular structures.
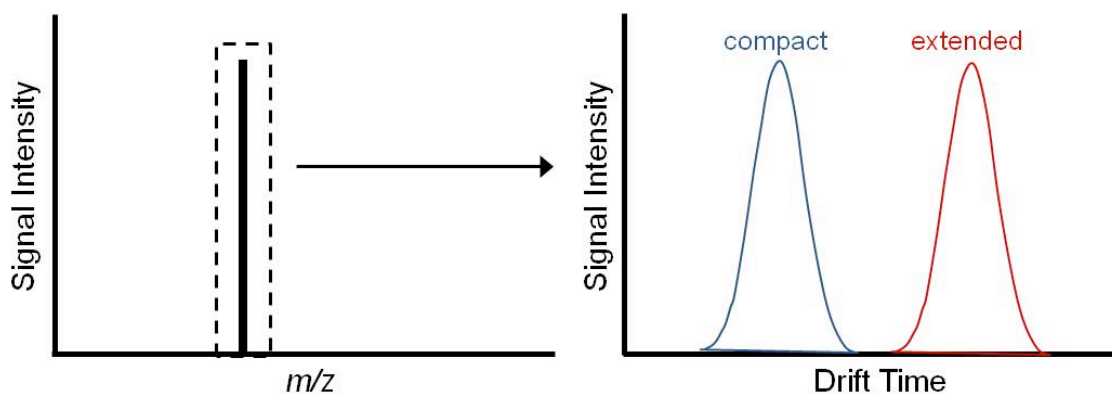
Figure 1. Theoretical data set obtained from drift tube IM-MS experiment. An advantage of coupling ion mobility to mass spectrometry is the ability to generate two dimensions of data analysis. IM arrival time distributions (ATD) will separate and differentiate ions of the same *m/z* but different structural motifs.

Multiple variations of IM techniques exist, including drift tube IMS,[7-9] traveling wave (TW) IMS,[10] overtone mobility,[11,12] differential mobility analysis (DMA),[13] and high-field asymmetric IMS (FAIMS),[14,15] each with characteristic features and advantages tailored to specific types of analytical experiments. Uniform field drift tube IMS is one of the most commonly used IM techniques owing to the ability to achieve high resolution ion separations and direct correlation to gas-phase collision cross sections (CCS).[8,16] Experiments involve the measurement of ion drift (arrival) times through a gas-filled drift tube under the influence of an electric field that is uniformly applied (**Figure 2**). Upon entering the drift tube, ions undergo collisions with a neutral buffer gas causing them to partition into groups based on differences in mobility.[17] The mobility parameter (K) depends most strongly on an ion's CCS and charge state and can be determined by the following equation,[17,18]

$$K = \frac{\upsilon_d}{E} = \frac{L}{t_d E} \tag{1}$$

where υ_d is the average drift velocity of an ion, E is the applied electric field across the drift tube, L is the length of the drift tube, and t_d is the drift time of the ion. Mobility values will vary based on experimental parameters, therefore reduced mobility values (K_0) are often reported to account for differences and provide a basis for comparison across different instrument platforms. Reduced mobility can be described by the following equation,[17]

$$K_0 = \frac{L}{t_D E} \frac{P}{760} \frac{273.15}{T} \tag{2}$$

in which P and T correspond to drift gas pressure and drift gas temperature, respectively. Further, reduced mobility can ultimately be converted to CCS (Ω) using the following expression,[17,19]

$$K_0 = \frac{3ze}{16N} \left(\frac{2\Pi}{\mu k_B T} \right)^{\frac{1}{2}} \frac{1}{\Omega} \tag{3}$$

where z is the ion charge state, e is the elementary charge, N is the buffer gas number density, μ is the reduced mass of the ion-neutral pair, k_B is the Boltzmann constant, and T is the buffer gas temperature. Based on equation (3), mobility is directly proportional to charge state and inversely proportional to CCS. Therefore, ions of higher charge states and/or smaller CCS will typically traverse the drift tube more quickly. Larger ions with increased CCS will undergo more collisions with background gas molecules resulting in increased drift times and smaller mobilities. It is important to note that experimental CCS measurements of ions provide a size measurement for different ion conformations, but molecular modeling is often needed to obtain specific structural information

corresponding to these values. CCS values can be calculated by a number of modeling methods and compared to experimental values to generate candidate structures for the ion conformations of interest.[20]
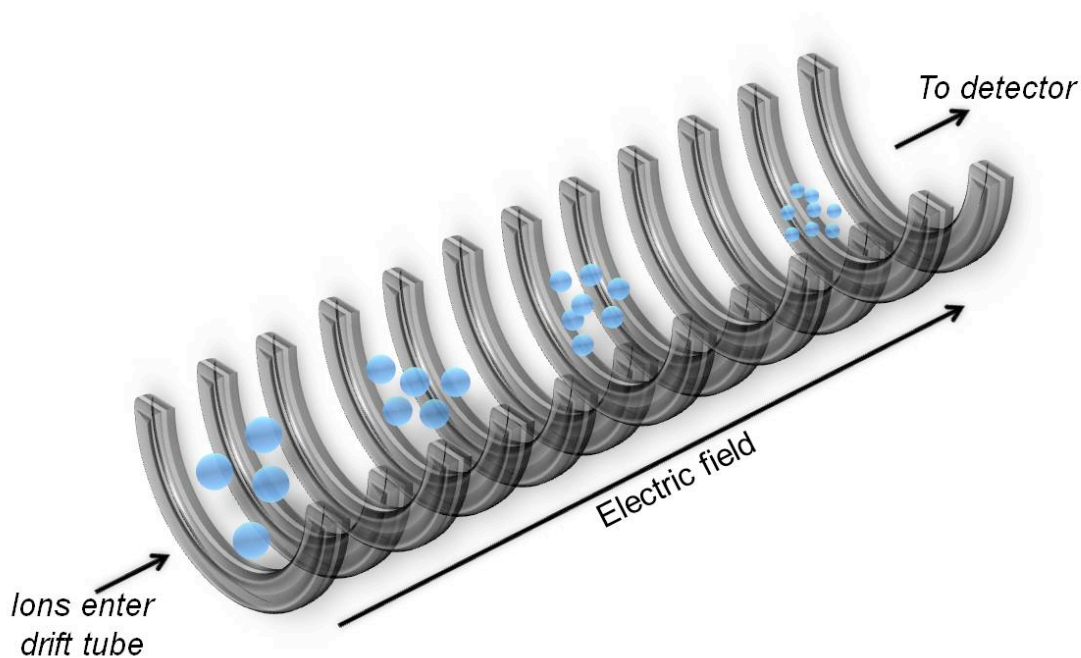
Figure 2. Schematic of a typical ion mobility uniform field drift tube experiment. Ions enter the drift tube, which is filled with a neutral buffer gas, and traverse under the influence of an applied electric field. As ions travel through the drift tube, they undergo collisions with a neutral buffer gas and separate based on differences in mobility. Mobility values are affected predominantly by charge state and size/shape. Upon exiting the drift tube, separated ion distributions can then go on to be mass analyzed.

Although the expression for calculating reduced mobility or CCS values accounts for changes in the temperature of the buffer gas, altering this temperature has been shown to have a significant effect on the observed ion drift times and separation

capabilities in the drift tube.[21-23] Initial work by May and Russell showed that low drift gas temperatures could be used to improve the separation efficiency of IM experiments for a number of small molecules.[24] This is consistent with theory, as the resolving power (R) equation at low fields is as follows,[25]

$$R = 32.33\left(\frac{LEz}{T}\right)^{\frac{1}{2}}$$

(4)

where L is the drift tube length, E is the applied electric field, z is the ion charge state, and T is the temperature of the drift gas. Therefore, the IM resolving power (R) is proportional to $(1/T)^{1/2}$ and low temperature IM experiments will increase R as a result. The analytical utility of reduced drift gas temperatures drove the initial development of the cold IM-MS instrument by May and Russell and led to the subsequent design and development of the current cryogenic-IM-MS instrument used for the studies discussed herein.[26] To our knowledge, this was the first low temperature IM-MS instrument designed specifically for studies of weakly-bound, noncovalent complexes, including extensively hydrated biomolecules, formed by electrospray ionization (ESI). Additional advantages of low temperature IM-MS experiments are outlined in the following section describing an overview of the technique.

1.2 Electrospray Ionization

As the development of IM-MS instrumentation progressed, a major limitation was the availability of robust ionization methods that could be used to transfer structurally labile molecules to the gas phase. The development of soft ionization

techniques, including electrospray ionization (ESI) and matrix-assisted laser desorption ionization (MALDI), allowed for the transfer of weakly-bound, intact biomolecular ions into the gas phase for analysis, revolutionizing the field of biological mass spectrometry. MALDI involves mixing an analyte solution with an appropriate matrix material, depositing it as a dried droplet onto a metal surface, and exposing it to a laser pulse resulting in the desorption of gas-phase ions.[27] The technique induces little to no fragmentation, but predominantly produces singly charged species, $[M + H]^+$. ESI is particularly powerful owing to the ability to produce multiply charged ions of the type $[M + zH]^{z+}$ directly from analytes in solution. It is widely accepted that ESI forms gas-phase ions by producing highly charged solvent droplets that undergo fission and evaporative events, under the influence of an electric field at ambient temperature and pressure, to yield small nanodroplets containing a single analyte ion, as shown in **Figure 3**.[28-31]
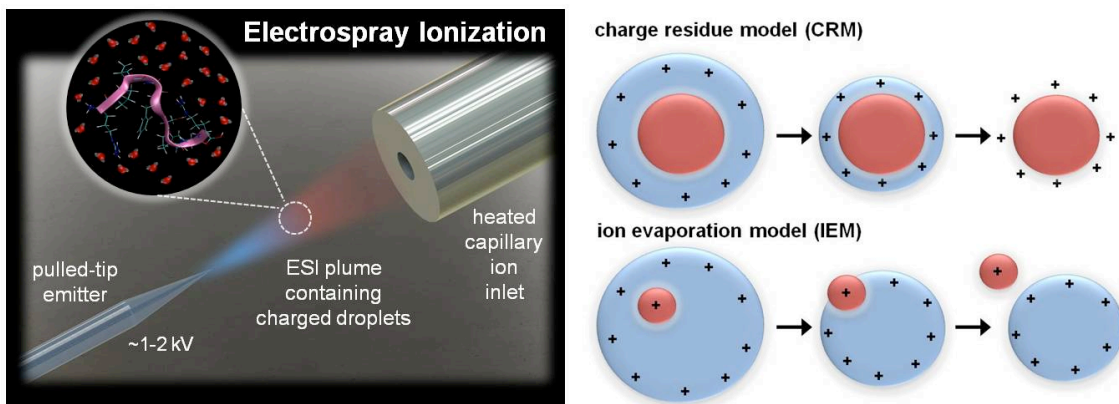
Figure 3. Schematic model depicting the formation of gas-phase ions during electrospray ionization (ESI). On left, the basic experimental setup is shown including a pulled-tip emitter, which is biased ~1 to 2 kV relative to the ion inlet on the instrument (heated capillary shown). The analyte solution is pumped through the emitter tip, and under the influence of an electric field, produces charged droplets carrying several analyte ions. These droplets undergo fission events as their surface charge overcomes the surface tension holding the droplets together. Schematics of both the charge residue model (CRM) and ion evaporation model (IEM), depicting the final stages of desolvation and production of gas-phase ions, are shown on the right.

The mechanism for formation of bare analyte ions from these small droplets is still debated and multiple models have been proposed to describe these final stages of desolvation.[32] Dole and coworkers originally proposed the charge residue model (CRM) to describe the final stages of gas-phase ion production during ESI.[30,33] The CRM is predicted to occur for large protein ions and states that small nanodroplets containing a single analyte ion undergo stepwise desolvation to produce dehydrated gas-phase ions. This implies that for certain proteins, dehydrated ions can retain native structure in the gas phase so long as cool instrument conditions are maintained, which has been shown by a growing number of recent studies.[34-37] An alternative mechanism describing the final stages of desolvation during ESI is the ion evaporation model (IEM), which was

originally proposed by Iribarne and Thompson.[38] The IEM is suggested to occur for small molecules and states that before small nanodroplets containing only a single analyte ion can be formed by evaporative and fission events, the surface charge density of the droplet can lead to ejection of an ion residing near the surface of a nanodroplet.[39] Therefore, an ion would no longer undergo stepwise desolvation until formation of a bare gas-phase ion, but would instead be ejected from a small droplet at some intermediate extent of hydration. Modeling of both mechanisms has been performed,[32] but few experimental techniques exist that can probe the final stages of desolvation during ESI. While ESI typically yields ions that are depleted of solvent, the low temperature environment of cryogenic ion mobility-mass spectrometry (cryo-IM-MS) affords the preservation and detection of solvated ions. The stabilization of extensively hydrated ions provides a means to monitor snapshots of the structural evolution of biomolecules during the final stages of desolvation during ESI.

1.3 Overview of Cryogenic Ion Mobility-Mass Spectrometry

Cryogenic ion mobility-mass spectrometry (cryo-IM-MS) incorporates a cold drift tube (80 K) to study the structures and dynamics of gas-phase ions at intermediate extents of hydration. Variable temperature IM experiments have been performed previously and cold IM drift cells, in particular, offer a number of advantages over traditional IM experiments carried out at ambient temperature. In order to preserve "native state" conformations, gentle instrument conditions must be employed which can oftentimes result in decreased resolution and ion transmission on ambient temperature

8

IM instruments.[40] However, decreasing the temperature of the IM drift gas has been shown to reduce diffusional broadening of the ion swarm through the drift cell, resulting in increased sensitivity and resolution.[24] In addition, low temperatures are required for the preservation of hydrated analyte ions on the experimental timescale, as weakly bound clusters would otherwise dissociate rapidly. Because hydrated ions can be effectively stabilized upon entering the cold drift cell, dynamic or interconverting conformers can potentially be kinetically trapped in specific structural arrangements.[41] While hydrated biomolecules have predominantly been studied using spectroscopic methods or condensed phase techniques,[42-44] recent gas-phase studies involving the sequential hydration of biomolecules have provided insights into the effect of hydration on ion structure.[45-47] A limitation of these studies is that hydrated ions are typically limited to small cluster sizes, whereas cryo-IM-MS is the first IM-MS apparatus designed specifically for structural studies of extensively hydrated cluster ions formed by ESI. Ions studied are of the type $[M + xH]^{x+}$ $(H_2O)_n$, where the number of water molecules, n, can vary from zero to several hundred depending on experimental conditions. This affords an experimental approach for tracking the structural evolution of hydrated ions en route to forming solvent-free gas-phase ions.

Figure 4 shows a typical mass spectrum produced by cryo-IM-MS. Protonated water clusters, $H^+(H_2O)_n$, were formed by ESI and the relative ion abundances observed reflect the relative stabilities of specific cluster ions. Previous work has shown that the temperature of hydrated cluster ions exiting the heated capillary falls in the range of 130 to 150 K owing to evaporative cooling.[42] Cryo-IM-MS adds further cooling (to 80 K) to

9

ions upon entering the cold drift tube, which aids in the preservation of large distributions of hydrated clusters, as shown in the mass spectrum in **Figure 4**. It is assumed that clusters are formed by evaporation of larger droplets as they traverse the heated capillary, and are captured upon entering the cold drift tube. The possibility of hydrated ions dissociating during the experiment was investigated and is discussed further in the following section. During ESI, magic number clusters for singly protonated water clusters are produced and can be preserved under cool instrument conditions.[26,42,48,49] These clusters exhibit an increased abundance relative to adjacent clusters owing to enhanced structural stability. For example, $H^+(H_2O)_n$ ($n = 21$) forms a stable, compact clathrate cage structure leading to its anomalously high abundance observed in the mass spectrum.[50,51]
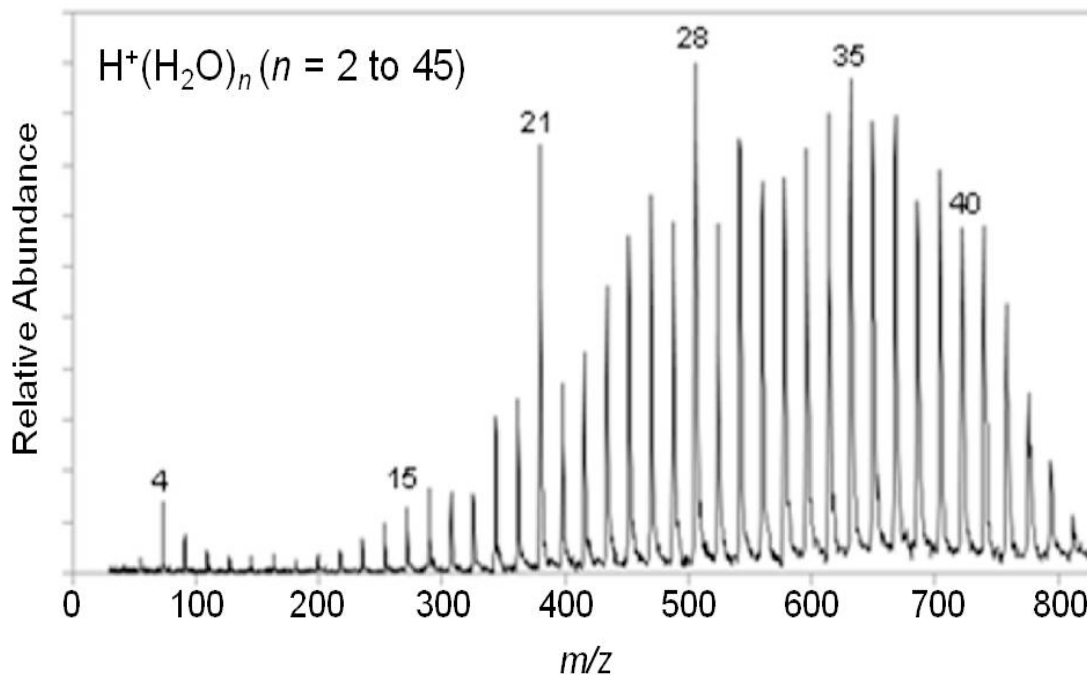
Figure 4. Typical mass spectrum generated by cryo-IM-MS of singly protonated water clusters, $H^+(H_2O)_n$ (n = 2 to 45), collected at a heated capillary temperature of 340 K. Water clusters were produced by ESI of a solution of deionized water (18 MΩ) that was acidified with HCl to a pH of 3.

Mobility data produced by cryo-IM-MS can be used to gain insight into the structure(s) and isomer distribution of the hydrated ions preserved. Plotting arrival time (drift time) versus *m/z* (**Figure 5**) generates two-dimensional (2-D) trendlines of hydrated cluster ions that can be used to track structural changes during desolvation. If the centroids of successive peaks fall along a uniform or straight trendline, it can be assumed that clusters undergo minimal, if any, structural changes during desolvation. The fairly regular decrease in arrival time between successive, (n) to (n-1), cluster ions reflects a small decrease in the overall CCS of the ion upon loss of a water monomer. However, if a deviation from a uniform trendline is observed in the 2-D mobility plots

11

generated by cryo-IM-MS, this indicates a structural change or rearrangement has occurred for the corresponding cluster. For a given ion occupying a specific charge state, a shift to shorter arrival times typically indicates formation of a more compact conformation while a shift to longer arrival times indicates conformer elongation. In the mobility plot shown in **Figure 5**, a unique signature is observed at $n = 21$, as evidenced by the shift to shorter arrival times compared to adjacent clusters.[26] This indicates that $H^+(H_2O)_n$ ($n = 21$) forms a conformer that is smaller in CCS than adjacent clusters, consistent with formation of the compact, clathrate cage structure predicted. The combination of MS and IM data generated by cryo-IM-MS provides a means to examine the extent to which desolvation alters ion structure.
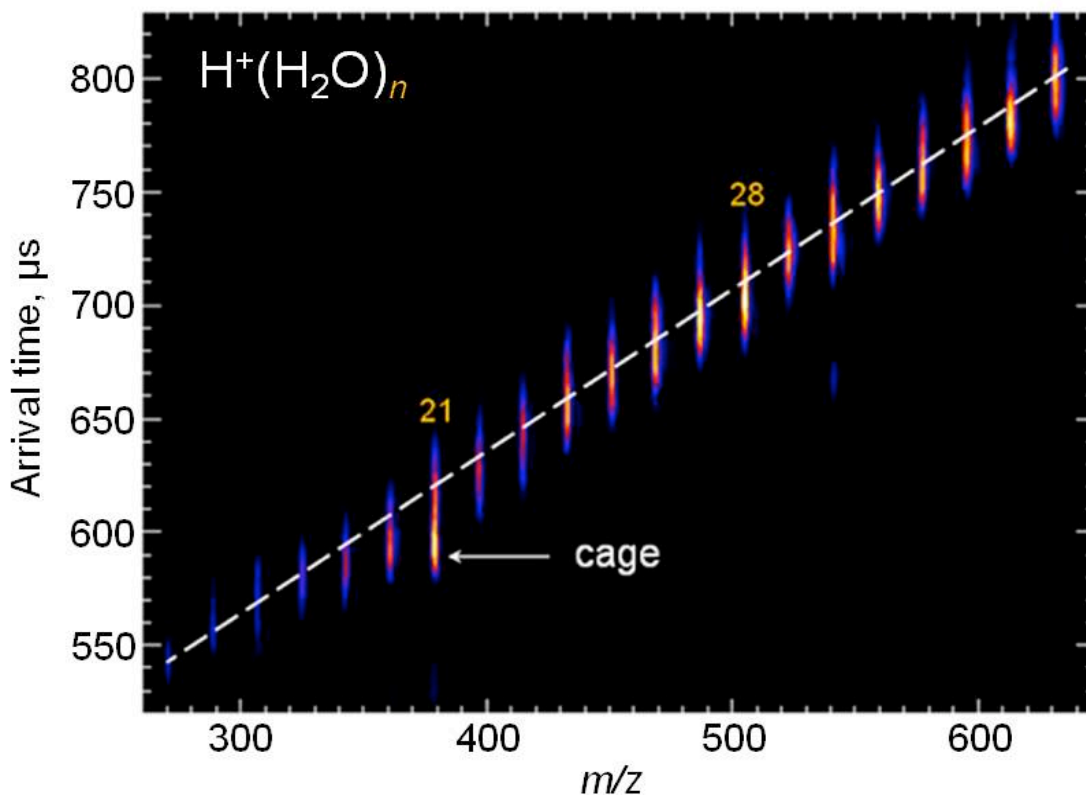
Figure 5. Typical mobility plot generated by cryo-IM-MS. Two-dimensional contour plot of arrival time (ATD) versus *m/z* for $H^+(H_2O)_n$ (n = 15 to 35) clusters, collected at a heated capillary temperature of 340 K. Data shown was collected under same conditions as data shown in Figure 4. The dashed line was inserted to guide the eye across the centroids of the IM-MS trendline shown.

1.4 Cryogenic Ion Mobility-Mass Spectrometry Instrumentation

A full schematic representation of the homebuilt cryo-IM-MS instrument is shown in **Figure 6**. Hydrated ions are generated by ESI at ambient pressure and transferred into the instrument through a heated capillary ion inlet. The heated capillary (11.4 cm in length, 400 µm inner diameter) is maintained between 50 and 100 °C to facilitate desolvation. The temperature of the heated capillary is inversely related to the number of hydrated ions preserved; decreasing the temperature results in shifting the

overall distribution of hydrated cluster ions, $[M + xH]^{x+} (H_2O)_n$, to larger numbers of n. Once ions exit the heated capillary, they are immediately focused through a skimmer cone into a DC ion guide. The skimmer cone provides differential pumping from ~1.5 Torr (region between capillary exit and skimmer cone) to ~5×10^{-4} Torr in the region housing the DC ion guide.[52,53] The ion guide consists of 43 identical lens elements (Kimball Physics Inc., Wilton, NH) with an inner diameter of 6.35 mm, thickness of 1.27 mm, and spacing of 1.27 mm between lenses. The first lens of the ion guide is isolated, while the potential of all remaining adjacent lenses alternates by ~40 V. This generates an oscillatory radial electric field, which focuses ions through a segmented lens and into a pulsed-gate electrode that is used to modulate ions entering the mobility drift cell. During IM-MS data collection, the gate electrode is briefly pulsed (for 12 μs at a frequency of 800 Hz) from 400 V (ion deflection mode) to 70 V (ion transmission mode), allowing discrete packets of ions to enter the drift tube. Once inside the drift tube, collisions with Helium buffer gas provide a means for ion separation on the basis of size/shape. An expanded view of the source region is shown in **Figure 7**.
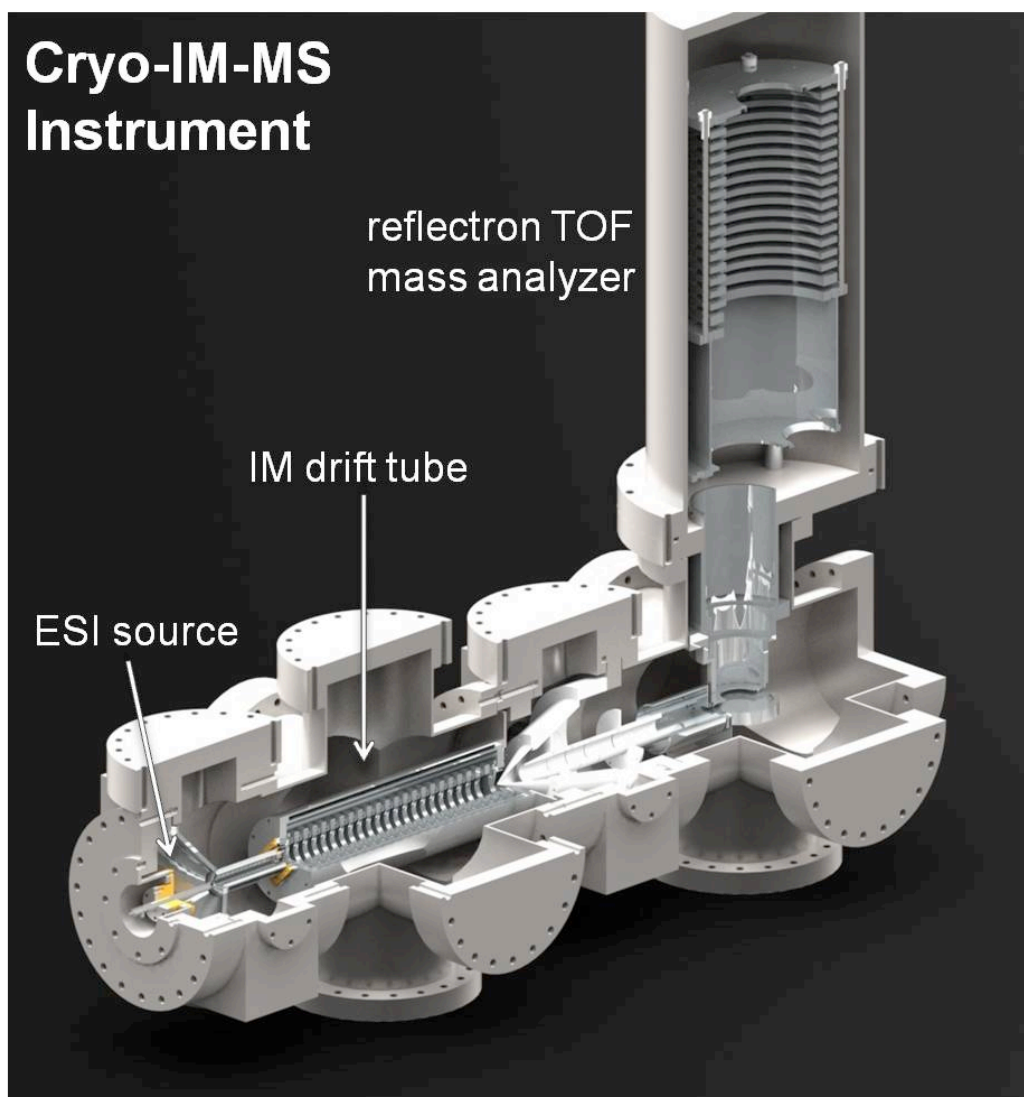
Figure 6. Full schematic view of the cryo-IM-MS instrumentation. Hydrated ions are generated by ESI at ambient pressure, enter the instrument through the heated capillary ion inlet, and are transferred through the DC ion guide into a cold (80 K) IM drift tube. Once ions exit the drift tube, they are orthogonally pulsed into a reflectron TOF mass spectrometer.
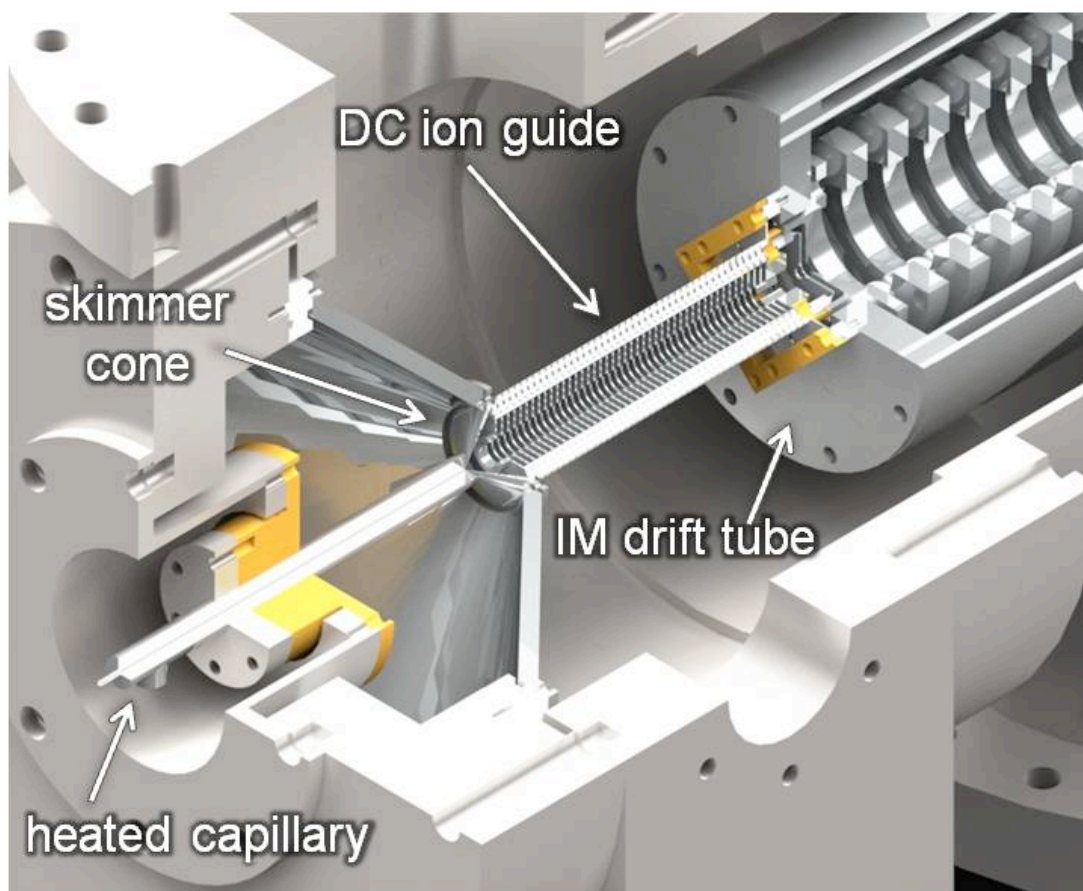
Figure 7. Expanded schematic view of the ESI source region of the cryo-IM-MS instrument. Source includes (1) a heated capillary ion inlet, (2) skimmer cone, and (3) DC ion guide.

The IM drift tube, adapted from a previous design by May and Russell,[24,54] is 30.2 cm long and comprised of a stacked ring electrode design that is made up of 24 identical stainless steel lens elements of equal width and spacing (6.35 mm). The inner diameter of each lens is 28.6 mm, achieving a uniform electric field across the drift tube, and the entrance and exit apertures are both 800 μm in size. Each lens is connected through a series of 1 MΩ resistors and spaced by a set of alumina nonporous ceramic balls (~8 mm diameter, McMaster-Carr, Aurora, OH). The entire assembly is housed

16

inside of a cryogenic dewar (**Figure 8**), which when filled completely with liquid nitrogen, can be cooled to ~80 K. The first and last electrodes are isolated from the cryogenic dewar using an insulating spacer and the entire drift tube is held in place by compression onto indium wire seals. The drift tube is filled with ultra high purity helium gas (99.999%) through stainless steel tubing (3.175 mm inner diameter), and the pressure inside the drift tube is maintained at ~1.6 Torr, based on the calibration described previously.[24] The temperature of the drift tube is maintained at 83 ± 3 K for all hydration studies and monitored by two platinum resistive temperature detectors (PT-100 ceramic encased, Omega Engineering Inc., Stamford, CT) placed at the front and back of the cell. During IM-MS data collection, ions are pulsed into the drift tube in discrete packets by the gate electrode and traverse the region under the influence of a weak electric field. Collisions with He buffer gas cool the ions to ~80 K and partition them into separate populations based on size/shape (mobility). Ions exiting the drift tube then go on for further mass analysis.
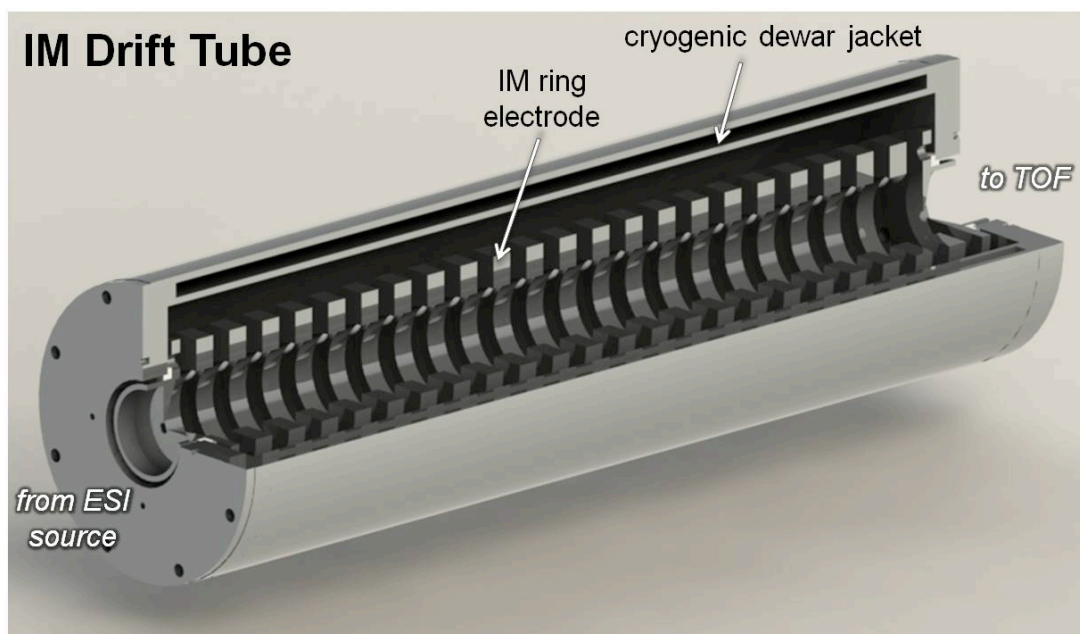
Figure 8. Schematic view of the cryogenic IM drift tube. The drift tube assembly is 30.2 cm long and consists of 24 ring electrodes encased inside of a cryogenic dewar. The drift tube is maintained at ~80 K for all experiments by filling the dewar jacket completely with liquid nitrogen.

The IM field strength is operated below the dissociative limit for all studies described herein, with < 10 V cm^{-1} applied across the drift tube. The effect of IM field strength on cluster ion preservation was initially investigated to establish the dissociative "low-field" limit for operation of the drift tube.[26] Mass spectra of protonated water clusters in the region $H^+(H_2O)_n$ (n = 2 to 45) were collected at IM field strengths ranging from 9.1 to 15.1 V cm^{-1} (**Figure 9**). The heated capillary temperature was maintained at 340 K to ensure that any heating ions encountered was field-induced, resulting from the increased field strengths applied. At low electric fields, magic number clusters (n = 21 and 28) are observed in high abundance relative to adjacent clusters owing to enhanced structural stability. As the field strength across the drift tube is increased, the abundances

18

of these ions decrease noticeably as water monomers are lost due to collision induced dissociation (CID) in the drift tube. The exact onset of CID, for ($n = 21$) specifically, is shown in **Figure 10** by plotting the percent abundance of clusters $H^+(H_2O)_n$ ($n = 20$ to 22) versus IM field strength. Beginning at 5.8 Td, the sharp increase in the abundance of ($n = 20$) coupled with the decrease in the abundance of ($n = 21$) suggests the onset of CID, which is expected to proceed via the loss of water monomers.[55] Therefore, maintaining a weak IM electric field ($E/N < 5.8$ Td) prevents the loss of water monomers to CID in the drift tube, emphasizing the importance of minimizing effective ion temperature throughout the experiment. Additionally, this ensures that drift time is directly proportional to the ion-neutral collision cross section (CCS).[17]
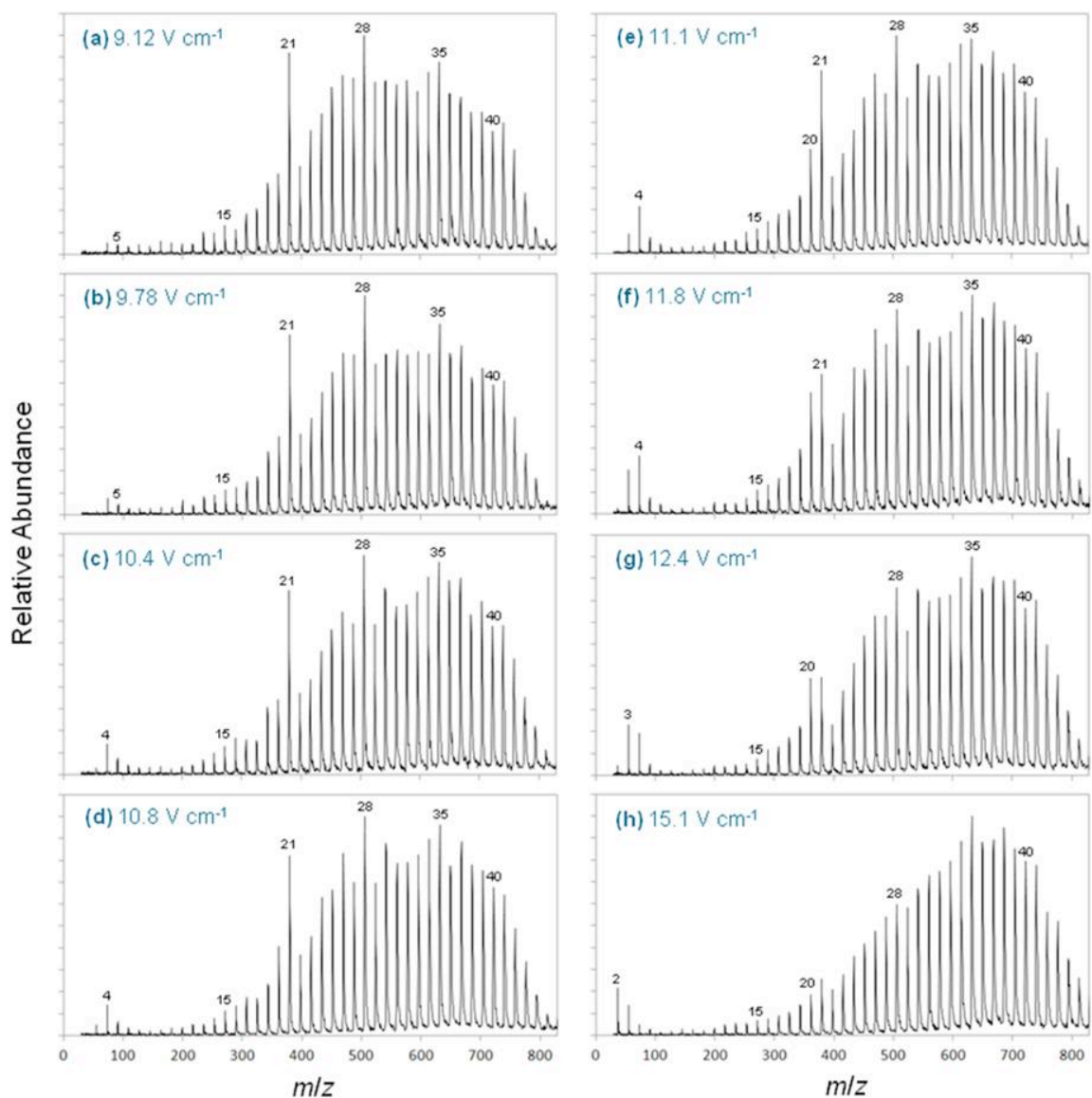
Figure 9. Mass spectra of protonated water clusters, $H^+(H_2O)_n$ (n = 2 to 45), as a function of electric field applied across the IM drift cell (9.1 to 15.1 V cm^{-1}). These conditions correspond to field strengths ranging from 5.0 to 8.4 Td. The temperature of the heated capillary ion inlet was maintained at 340 K for all spectra.
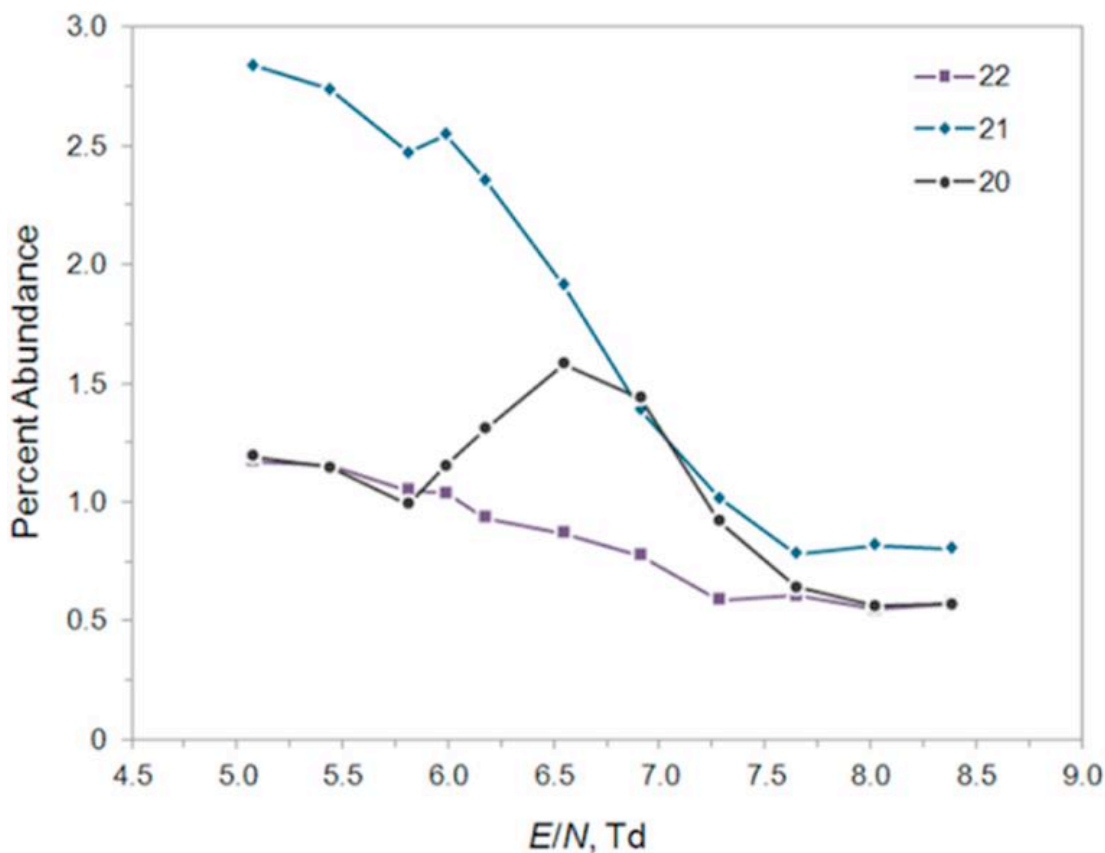
Figure 10. Percent abundance of $H^+(H_2O)_n$ (n = 20 to 22) plotted as a function of IM field strength. Percent abundances were calculated from the mass spectra shown in Figure 9. Beginning at 5.8 Td, the IM field strength exceeds the "low-field" limit and the onset of CID is observed resulting in the dissociation of weakly bound water monomers from cluster ions.

After ions exit the drift tube, they are immediately focused through a skimmer cone and set of Einzel focusing lens elements before being orthogonally pulsed (12-15 kHz) into the reflectron time-of-flight (TOF) mass spectrometer (**Figure 11**). The TOF was adapted from a commercial instrument (Vestec Mariner TOF) and is maintained at 1×10^{-7} Torr (**Figure 12**).[56] The TOF push plate voltage is typically operated at 3.5 kV while the reflectron back ring is maintained between 4-5 kV. Ions are detected using a 40 mm dual microchannel plate assembly (Photonis, Sturbridge, MA). Pulse

synchronization of the IM gate electrode and TOF extraction source is used for IM-MS data collection and is achieved through the use of custom 2-D acquisition software (Ionwerks, Houston, TX).
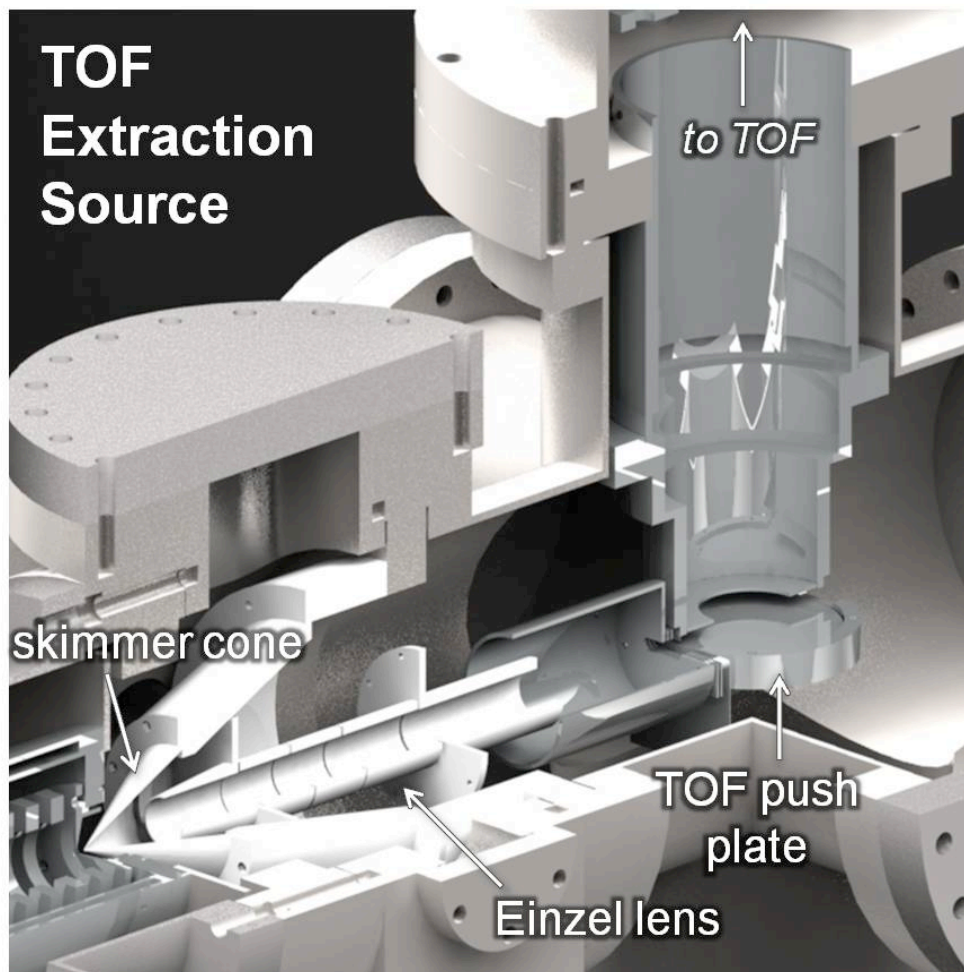
Figure 11. Expanded schematic view of the TOF extraction source region of the cryo-IM-MS instrument. After ions exit the drift tube they are focused through a skimmer cone and set of Einzel lens elements before being orthogonally pulsed into the TOF mass spectrometer.
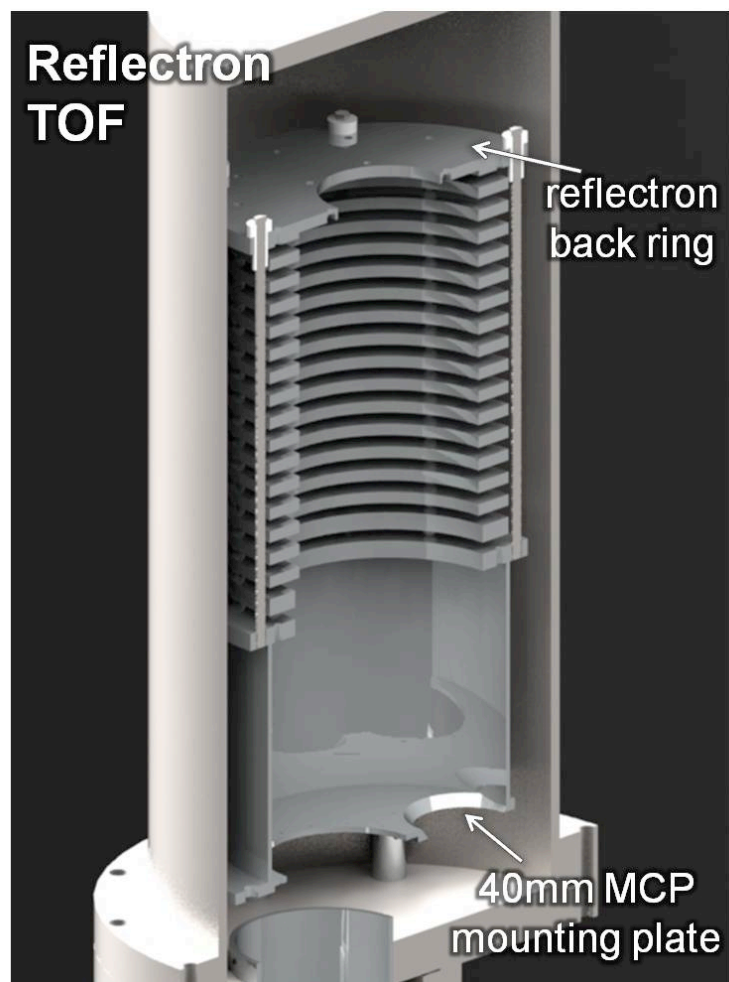
Figure 12. Expanded schematic view of the reflectron time-of-flight (TOF) mass spectrometer on the cryo-IM-MS instrument. The region is maintained at a pressure of ~1x10^{-7} Torr via differential pumping and ions are detected using a 40mm dual microchannel plate (MCP) assembly.

2. EVOLUTION OF HYDROGEN-BOND NETWORKS IN PROTONATED WATER CLUSTERS STUDIED BY CRYOGENIC ION MOBILITY-MASS SPECTROMETRY[*]

2.1 Background

The fundamental importance of understanding the hydrogen bond networks in water has led to the extensive exploration of the structure and dynamics of protonated water clusters, $H^+(H_2O)_n$. To date, most studies have relied upon matching computational methods with spectroscopic signatures to assign vibrational bands. In particular, the free-OH spectral region (~3700 cm^{-1}) has provided insight into questions regarding magic and anti-magic number phenomena,[42,48,57] H-bond coordination,[50,51,58-62] the existence of unique clathrate structures,[50,51,63-67] the location and nature of the charge,[62,63,68-71] and the temperature dependence of the structures.[61,72-75] However, because gas-phase spectroscopic methods are not structurally dispersive, conformational heterogeneity of the cluster population becomes a significant source of spectral congestion, particularly in the H-bonded OH stretching region (~2800-3500 cm^{-1}).[76] Because spectroscopic data reflect a superposition of the spectral contributions from different conformers, as the sizes of molecules increase, many questions remain regarding the isomeric composition of a given cluster population. In addition to

---

[*] Reprinted with permission from "Evolution of Hydrogen-Bond Networks in Protonated Water Clusters $H^+(H_2O)_n$ (n = 1 to 120) Studied by Cryogenic Ion Mobility-Mass Spectrometry" by Servage, K. A.; Silveira, J. A.; Fort, K. L.; Russell, D. H., 2014. *J. Phys. Chem. Lett.*, 5, 1825-1830, Copyright 2014 American Chemical Society.

conformational heterogeneity, the extent of thermal broadening also contributes to spectral complexity.[43,44] Even if the molecules are kept vibrationally cool, IR spectra appear unresolved in the H-bonded region owing to the similar local H-bonding environments for many of the water molecules within a protonated cluster.[44] Moreover, computational methods for describing large protonated water clusters are limited owing to increased computational costs coupled with the complex potential energy surface inherent in H-bonded clusters.[66,67,77]

The development of cryogenic ion mobility-mass spectrometry (cryo-IM-MS) was outlined in Chapter 1 and initial studies demonstrated that the technique could be used to generate and preserve solvated ions produced by electrospray ionization (ESI).[26,78] The initial work showed that protonated water clusters, generated by ESI, could be preserved in the gas-phase for IM-MS analysis so long as cool instrument conditions were maintained. The structural preferences of hydrated ions were shown to be highly dependent on the type of charge carrier present and cool instrument conditions allowed for the retention of "magic number" clusters possessing enhanced stability. Because the relative ion abundances observed in the mass spectra are correlated to stability, particularly stable clusters will exhibit enhanced abundance over adjacent clusters in the distribution. This "magic" stability arises from energetically favorable structural arrangements of the water network surrounding the proton. As was shown, the anomalously abundant $n = 21$ cluster adopts a more compact structure than adjacent clusters in the distribution, consistent with formation of a clathrate cage structural motif.[50,51] In the present work, we expand on previous studies to broaden the region of

interest to include both the small $H^+(H_2O)_n$ (n = 1 to 30), and large, (n = 31 to ~120), cluster regions.[79] The results from cryo-IM-MS are complementary to past spectroscopic and computational results and provide clear insight into the isomeric composition of each species at 80 K.

2.2 Experimental Methods

The instrumentation used for these studies has been previously described in detail and was outlined in Chapter 1.[26] Protonated water clusters were produced by electrospray ionization (ESI) of deionized water (18 MΩ) that was acidified to a pH of 3 using HCl. The heated capillary ion inlet temperature was varied (326 to 356 K) to control the extent of hydration. Cluster ions produced in the source region were transferred into the cold (80 K) drift tube using an electrostatic ion guide. Inside the drift tube, clusters are separated on the basis of their mobility and are subsequently pulsed into the time-of-flight mass spectrometer. For these studies, the He (g) inside the drift tube was maintained at 80 +/- 2 K via liquid nitrogen cooling. The field strength was operated below the previously established dissociative limit (E/N < 5.8 Td) due to the low field strength requirements for cryo-IM-MS hydration studies.[26] Collision cross sections were estimated for the $H^+(H_2O)_n$ (n = 6) species using the simulation program MOBCAL.[18,80,81] DFT calculations were performed at the B3LYP/3-21G level to obtain optimized structures and theoretical estimations of collision cross sections were then calculated using MOBCAL software. Initial structures for both the Eigen- and Zundel-

centered isomers were estimated based on the low energy structures determined by Jiang *et al.* via ab initio calculations.[61]

2.3 Results and Discussion

Figure 13 contains ESI mass spectra of protonated water clusters $H^+(H_2O)_n$ (n = 2 to ~160) that were collected by varying the ESI capillary temperature. The low temperature (80 K) environment of cryo-IM-MS preserves the extensive hydrogen bond network surrounding the excess proton, specifically when inlet conditions are kept cold, while the relative abundance of a particular species reflects its structural stability. Evidence for the enhanced stability of magic number clusters n = 4 and 21, revealed in the mass spectra through an intensity anomaly relative to adjacent clusters, is observed at heated capillary temperatures between 326 and 356 K. Decreasing the temperature of the heated capillary to 326 K shifts the distribution to larger values for n (~160) while preserving the H-bond network around the proton produced during the ESI process. The ability to precisely control the extent of hydration affords the investigation of both the small (n = 1 to 30) and large size regions (n = 31 to ~120).
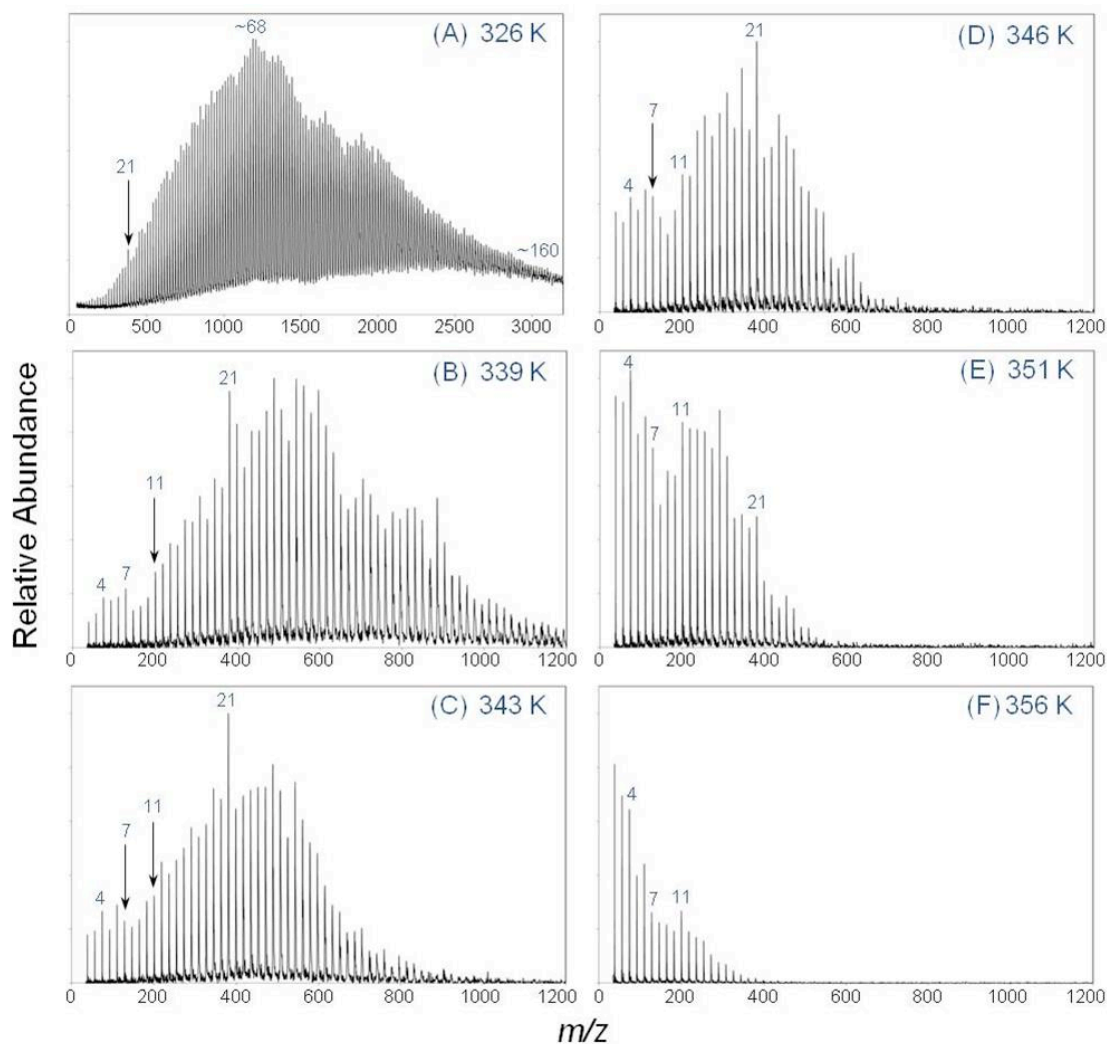
Figure 13. Mass spectra of protonated water clusters, $H^+(H_2O)_n$, collected at various heated capillary temperatures ranging from (A) 326 K up to (F) 356 K. Increasing the temperature of the heated capillary promotes evaporation of water monomers and shifts the distribution of cluster ions to lower numbers of n.

2.3.1 Structural Transitions of Protonated Water Clusters

The 2-D contour plot of arrival time distribution (ATD) vs. m/z shown in **Figure 14** reveals distinct structural transitions that occur in the small size range, $H^+(H_2O)_n$ ($n = 1$ to 30). It is evident that the ATDs for ($n = 1$ to 7) fall along a uniform trendline which

is distinctly different from that for (n = 8 to 20). Lee, Chang, and coworkers first predicted that the hydrogen-bond network surrounding the proton evolves from chain-type structures into 2-D net structures from ($\sim n$ = 6 to 8).[58,59,61] Miyazaki *et al.* found spectroscopic evidence for this transition by probing the OH stretches and analyzing the contributions from 1-, 2-, and 3-coordinated (coord) water molecules in the (n = 4 to 27) size region.[50] Coordination numbers assigned to specific water molecules within a cluster are consistent with previous spectroscopic studies.[50,51,61] A 1-coord water molecule simply refers to a molecule in a single H-bond accepting configuration with two free hydrogen atoms. The existence of chain-type structures was attributed to the presence of free-OH stretching bands corresponding to 1-coord water molecules that terminate the H-bond chain. Beginning at n = 7, the authors observed a decrease in the OH stretching bands of 1-coord water molecules until the eventual disappearance of such bands at $\sim n$ = 10. In addition, the simultaneous appearance of the OH stretching bands attributed to 3-coord water molecules (double acceptor-single donor, AAD) was first observed at n = 7 in the spectra. AAD water molecules are expected to exist in net- or cage-like structures and thus the authors concluded that the two synchronous spectral features indicated that the transition from chain to 2-D net structures occurs over the size range ($\sim n$ = 7 to 10).[50] This would suggest a bridging of the chain type structure for n = 7 into a net structure, absent of 1-coord water molecules, upon the addition of several water monomers.
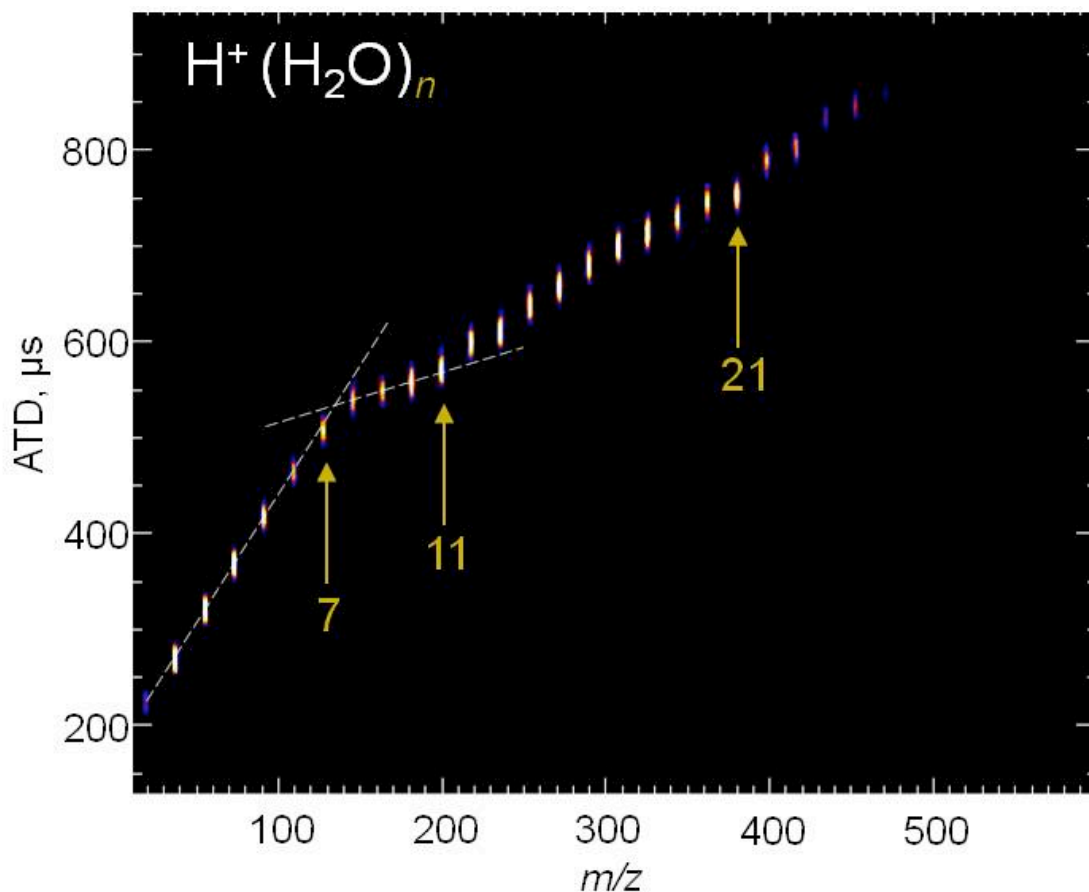
Figure 14. Two-dimensional contour plot of ATD versus m/z for $H^+(H_2O)_n$ ($n = 1$ to 25) collected at a capillary temperature of 346 K. The dashed lines are included to guide the eye along the IM-MS trendlines for regions ($n = 1$ to 7) and ($n = 8$ to 11).

Figure 14 clearly shows that a distinct structural transition occurs at $H^+(H_2O)_n$ ($n = 7$) from a region ($n = 2$ to 7) in which the centroid of each peak falls along a uniform trendline to a region ($n = 8$ to 11) in which the difference in drift time between adjacent clusters is greatly reduced. The region $H^+(H_2O)_n$ ($n = 12$ to 20) also appears to follow a unique trendline, deviating only for the $n = 21$ cluster.[26] On the basis of previous studies, clusters in the size range ($n = 12$ to 21) are dominated by 3-coord water molecules,[50,51] consistent with 2-D net structures and subsequent formation of the compact clathrate

cage for $n = 21$. Clusters in this range have been shown to possess no 1-coord water molecules, meaning all isomers are stabilized by a network of interconnected H-bonds. Miyazaki *et al.* proposed that the H-bond network of water molecules can preserve a 2-D net structure up to $\sim n = 19$, at which point the formation of the cage-like structure(s) begins.[50] While the regions ($n = 8$ to 11) and ($n = 12$ to 20) both consist of 2-D net structures, it is clear from the trendline shown in **Figure 14** that the evaporation of water molecules induces very different structural changes in the two regions. Beginning at $H^+(H_2O)_n$ ($n = 11$), the loss of each water monomer should indicate an increase in 1-coord water molecules within a given species until formation of a stable chain-like structure. The uniform trendline observed for smaller clusters, $H^+(H_2O)_n$ ($n = 1$ to 7), suggests that these cluster populations exist as chain-type structural motifs and possess no 3-coord water molecules, consistent with previous studies. The changes in ATD observed in **Figure 14** for the ($n = 8$ to 11) species clearly show that the loss of each successive water molecule is accompanied by rearrangement reactions to yield structural isomers that undergo minimal changes to the overall size of the molecule. The clusters in the range ($n = 8$ to 11) reveal an average difference in arrival time between adjacent clusters of ~ 10 μs as compared to ~ 48 μs over the range ($n = 1$ to 7). This suggests that the loss of water monomers by evaporation promotes opening of the 2-D net structures into chain-like structures over the range ($n = 8$ to 11), which allows the cluster to expand and maintain a similar overall size. This is the first evidence observed via IM-MS of the transformation of net structures into chain-like structures upon desolvation of protonated water clusters over the range ($n = 8$ to 11).

31

2.3.2 Eigen versus Zundel Cations

Perhaps the main advantage to studying clusters via IM-MS as opposed to spectroscopic methods is the ability to elucidate information about the isomeric composition of a given cluster population. The number of structural isomers for a protonated water cluster distribution has been predicted to increase exponentially with cluster number,[61,82,83] and that appears evident in **Figure 15** as the ATDs become broad and non-Gaussian as the cluster number increases. There does, however, appear to be a unique feature for the $H^+(H_2O)_n$ ($n = 6$) cluster, which as previously stated, should correspond to a chain-type structure, similar to adjacent clusters. The mass-selected ATD for the $n = 6$ cluster ion shown in **Figure 16** reveals a second, slightly less abundant population shifted to shorter drift times centered around 464 μs. Protonated water cluster ions can exist as Eigen cations (H_3O^+-centered) or Zundel cations ($H_5O_2^+$-centered), depending on the extent of solvation.[61,82,84-86] Previously, we showed evidence for the enhanced stability of the $n = 4$ isomer and attributed this to a fully solvated H_3O^+-centered structure, having one water monomer H-bonded to each of the central hydrogen atoms.[26] Assuming similar hydration, the fully solvated Zundel cation should correspond to an $H_5O_2^+$-centered isomer bound to four water monomers. Thus, the two distinct populations observed in **Figure 16** are assigned to a fully solvated Zundel cation ($H_5O_2^+(H_2O)_4$) in addition to the extended chain-type structure ($H_3O^+(H_2O)_5$) expected in this range. Spectroscopic evidence for the coexistence and stabilization of both structures in the gas-phase, within the isomer population $H^+(H_2O)_n$ ($n = 6$), has been reported by Jiang and coworkers through a comparison of spectroscopic data with ab

initio calculated spectra,[61] whereas Fujii *et al.* confirmed that the $n = 6$ cluster is the smallest system to include both Eigen- and Zundel-centered structures.[87] Very recently, Heine *et al.* utilized IR-IR double resonance spectroscopy to generate isomer-specific spectra corresponding to both the Eigen and Zundel cations for the $H^+(H_2O)_n$ ($n = 6$) species.[88] Representative structures of the corresponding low energy isomers determined by Jiang and coworkers are shown in **Figure 16**. In order to accurately assign both populations in the ATD profile, collision cross section (CCS) values were estimated using MOBCAL. The calculated CCS for the Eigen-centered structure was determined to be 46.46 $Å^2$ whereas the Zundel-centered isomer is slightly larger, 47.97 $Å^2$, corresponding to a difference of ~3%. This result suggests that the population centered at longer drift times corresponds to the fully solvated Zundel cation. Jiang and coworkers determined that the Zundel isomer for $H^+(H_2O)_n$ ($n = 6$) is ~1 kcal/mol more stable than the Eigen cation,[61] which is consistent with the relative abundances of each population shown in **Figure 16**; the population shifted to shorter drift times has a relative abundance of ~50%. Hence, the population centered at shorter drift times is assigned to the Eigen cation, and the larger population is assigned to the fully solvated Zundel cation. While the results shown here suggest that $H^+(H_2O)_n$ ($n = 6$) is the smallest cluster in which Eigen and Zundel conformers coexist, we cannot rule out the possibility that both isomers could be present for smaller cluster ions ($n < 6$) as well. Improved IM resolution capabilities would be needed to determine this definitively.
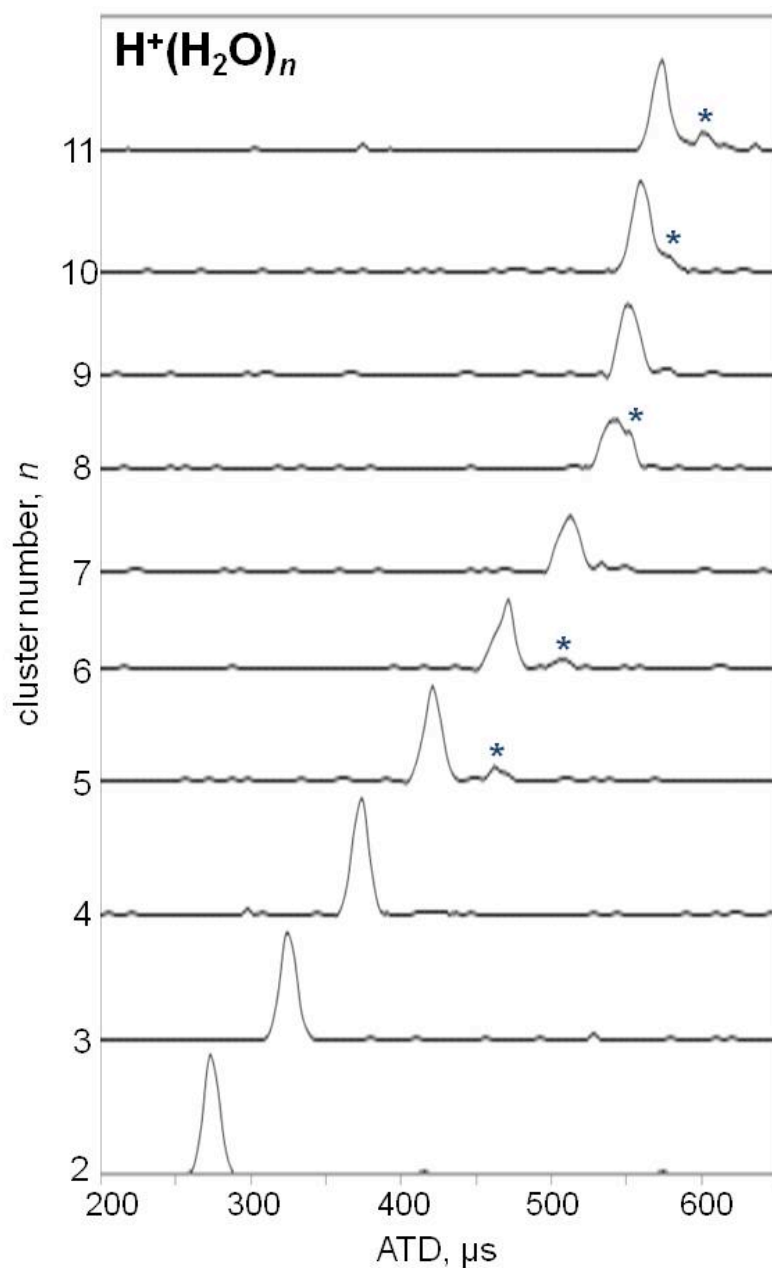
Figure 15. Mass-selected ATD profiles for clusters $H^+(H_2O)_n$ (n = 2 to 11) collected at a heated capillary temperature of 346 K; data was extracted from data set shown in Figure 14. The peaks labeled with asterisks result from post IMS loss of a water monomer by collision induced dissociation of the $H^+(H_2O)_{n+1}$ species.
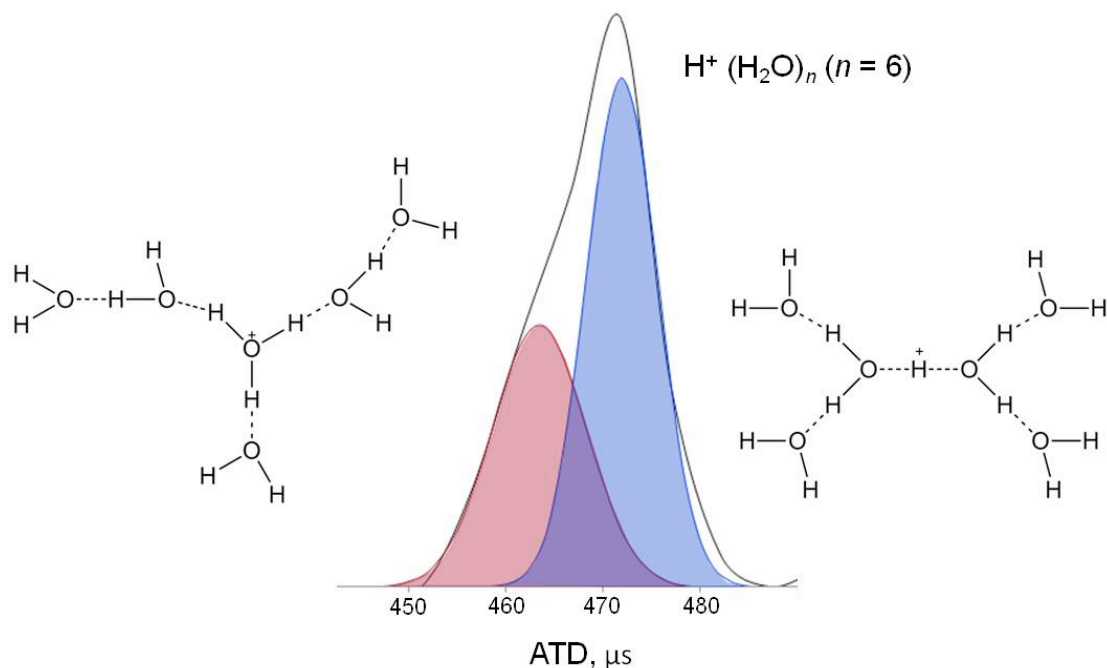
Figure 16. Expanded view of the mass-selected ATD for $H^+(H_2O)_n$ ($n = 6$); peak fitting was performed using Origin 7.5 software. Conformer population centered at 464 μs and shown in red corresponds to H_3O^+-centered structures, while the population falling at longer drift times, 472 μs and shown in blue, is attributed to the $H_5O_2^+$-centered structures solvated by four water monomers. Structures shown are schematic representations of the two lowest energy isomers for the $H^+(H_2O)_n$ ($n = 6$) cluster determined by Jiang *et al.* via ab initio calculations.[61]

2.3.3 Transition from Clusters to Bulk Water

Although spectroscopic techniques have the ability to yield tremendous insight into the structures of H-bonded water networks for small clusters ($n = 1$ to 30), there is very little known about larger systems owing to the difficulty in producing resolved spectra. For some time, the structural analysis of small clusters has been treated as a model for bulk systems, but a clear notion of the number of water molecules necessary to exhibit bulk properties remains elusive. It has been predicted that large water clusters

35

($n > 100$) can begin to exhibit interior crystallization similar to that of hexagonal ice, which consists of a crystalline network made up of 4-coord water molecules.[77,89-92] If this is the case, a deviation indicative of a structural transition should be observed in the IM-MS data corresponding to the onset of crystallization within a given species. The dominance of 4-coord water molecules in bulk systems contributes to the spectral congestion for large $H^+(H_2O)_n$ clusters.[77,93] Four-coord water molecules do not possess free-OH stretches, meaning any structural analysis must come from the spectral features buried in the H-bonded OH stretching region, which often cannot be distinguished from 2- and 3- coord contributions. Fujii and coworkers were able to generate IR spectra of the OH stretching region for mass-selected protonated water clusters up to $n = 200$ and identify a broad spectral signature assigned to 4-coord water molecules.[93] They observed a decrease in the intensity of the free-OH stretch with increasing cluster size, owing to the transition from 3-coord water molecules to 4-coord, but never observed complete disappearance of the band.

Figure 17 shows the plot of ATD vs. *m/z* of stable $H^+(H_2O)_n$ clusters up to $\sim n = 120$, collected at a heated capillary temperature of 326 K. Operating under cool inlet conditions allows for the production and stabilization of large cluster ions on the experimental time scale while preserving the unique structural features present in the low-mass region: specifically the trendline deviations previously discussed for ($n = 21$) and ($n = 8$ to 11). Though the high mobility of the proton in water lends itself to several structural isomers for a given species, the centroids of ATDs in the large size region, ($n = 30$ to ~ 120) appear to fall along a uniform trendline with no sharp structural

transitions. Although detection of small structural changes becomes more difficult for large numbers of n, the trendline suggests that clusters in this range closely resemble adjacent clusters in size. Therefore, either the threshold for water exhibiting bulk properties has not been reached or the transition to bulk occurs not at any one particular species, but rather a gradual evolution into clusters containing only 4-coord water molecules and more closely resembling ice. Although spectroscopic techniques have typically been employed to investigate these systems, such methods are not structurally dispersive and thus become limited for large species, which are made up of several isoenergetic structural motifs. Cryo-IM-MS facilitates the preservation of large H-bonded clusters and provides the ability to separate these clusters based on structure in order to investigate the isomeric composition of each species at 80 K. This capability makes cryo-IM-MS a useful tool, complementary to spectroscopic and computational methods, that can be used to elucidate any structural changes associated with the transition to bulk water.
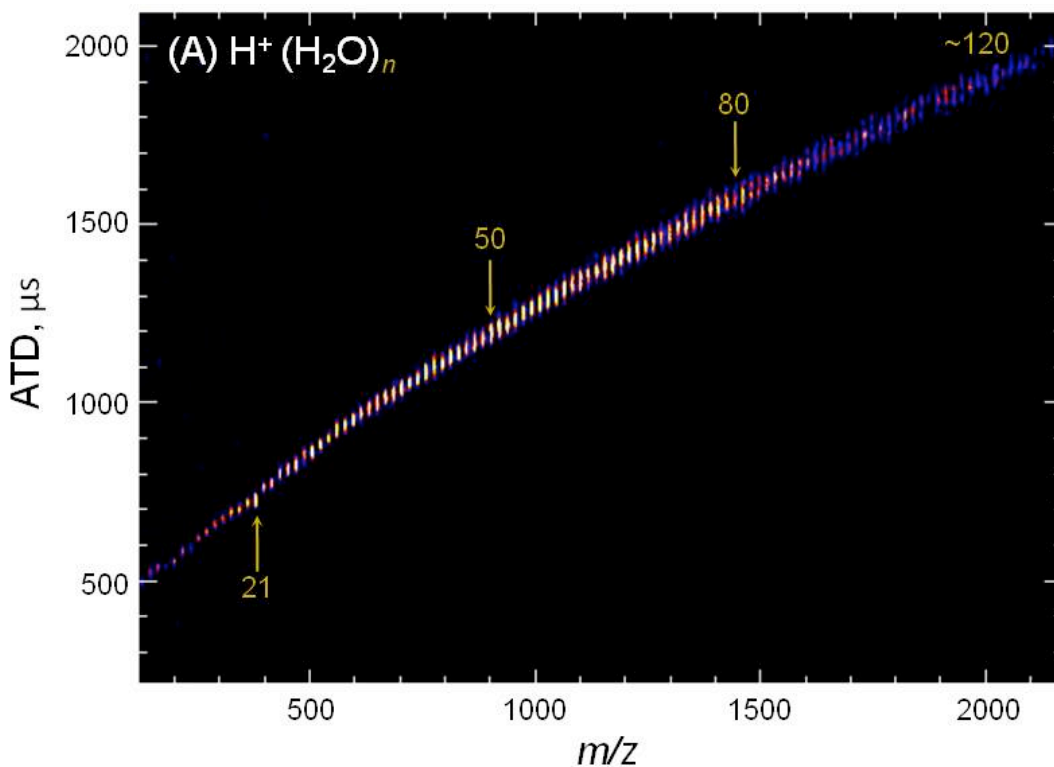
Figure 17. Two-dimensional contour plot of ATD versus *m/z* for $H^+(H_2O)_n$ ($n = 1$ to ~120) collected at a heated capillary temperature of 326 K.

2.4 Conclusions

Protonated water clusters produced by ESI and cryogenically cooled in the drift tube to ~80 K are investigated via cryo-IM-MS in both the small, ($n = 1$ to 30), and large, ($n = 30$ to 120), regions. Evidence for unique structural transitions is elucidated in the low mass region corresponding to the changes associated with the evolution of the H-bond network around the excess proton. Upon desolvation, this evolution occurs via the transition from 2-D net structures ($n = 12$ to 20) into chain-type structures ($n = 1$ to 7) over the range ($n = 8$ to 11). Cryo-IM-MS results reveal evidence for two unique populations for the $H^+(H_2O)_n$ ($n = 6$) system, which are attributed to the coexistence of

Eigen- and Zundel-centered structural motifs. These results show excellent agreement with previous spectroscopic and computational studies. Typically, spectroscopic methods are employed to investigate these systems, as opposed to IM-MS, owing to the difficulty in stabilizing weakly bound cluster ions on the experimental time scale. However, spectroscopic techniques become limited for large clusters due to spectral congestion, while the gentle instrument conditions of cryo-IM-MS provide a new means of probing the isomer distributions of large-scale water clusters and elucidating structural information on the extensive H-bond networks. Although it has been previously suggested that protonated water clusters possess bulk character at $\sim n = 100$, no significant structural changes were observed for clusters up to $n = 120$. While the exact onset of bulk properties within a protonated water cluster remains elusive, we have shown that cryo-IM-MS has the ability to elucidate information about the isomeric composition of a wide range of species at 80 K and provides a realistic approach to address the issue. Analysis of protonated water clusters by cryo-IM-MS illustrates the utility of the technique as a structural probe for hydrated ions and establishes a basis for studying the structural effects of water bound to larger biological molecules.

3. UNFOLDING OF HYDRATED ALKYL DIAMMONIUM CATIONS REVEALED BY CRYOGENIC ION MOBILITY-MASS SPECTROMETRY[*]

3.1 Background

A number of competing effects dictate the conformer preferences of biomolecules as they transition out of solution and into the gas phase, including solute-solvent interactions,[46,78,94-97] Coulombic repulsion of like-charges,[68,98-100] and intramolecular charge-solvation.[34,35,37,44,47,78,101-103] As a result, a multitude of studies utilizing a variety of theoretical and experimental techniques have focused on determining the specific effects of solvation on peptide and protein structure with an objective of deconvoluting the many contributions to structural preferences. It has been established that for most biological molecules, the preferred water binding sites are the accessible hydrogen bond donors or acceptors and the charged side chains.[94,104] Sequential hydration studies of ammonium, guanidinium, and carboxylate ion groups reveal the size of the first solvation shell(s),[42,105-109] preferences for self-solvation and salt-bridge formation,[110-113] and in a number of cases, binding energies of the first few water molecules have been determined.[104,114-120] Perhaps the most significant perturbation to the H-bond network of water clusters results from the charge-carrying species within the cluster. It is of interest therefore, to consider how the structure of

water would be affected by the presence of various charge-carrying groups, and simultaneously, how the structures of these ions adapt in response to a dynamic hydration environment.

Previous cryo-IM-MS studies on exclusively lysine- (or ornithine) or arginine-containing peptides have been compared to highlight differences between hydration of the ammonium ion and guanidinium ion, respectively.[26] Water networks surrounding the ammonium ion have been shown to exhibit specific solvation behavior (magic number clusters), similar to what is observed for the hydronium ion (Chapter 2).[26,42,44,47] However, hydration of the guanidinium ion does not appear to promote formation of magic number clusters. Mobility data shown in **Figure 18** for the peptide bradykinin (BK) (Arg-Pro-Pro-Gly-Phe-Ser-Pro-Phe-Arg), for which no magic number clusters were observed in the mass spectrum, clearly show that $[BK + 2H]^{2+}(H_2O)_n$ ions form a uniform trendline of hydrated ions. While the ATDs of these ions are broad, reflecting some degree of conformer heterogeneity, the uniformity of the trendline suggests that the ion population retains structural stability throughout the final stages of desolvation. The lack of deviation in the trendline reflects the absence of clusters possessing special stability for an arginine-containing peptide ion. Alternatively, hydration of gramicidin S (GS) (cyclo(-Pro-Val-Orn-Leu-DPhe-)$_2$) shows evidence for formation of magic number clusters ($n = 8$, 11, and 14) in the mass spectrum, resulting from favorable arrangements of water around the ammonium ion of ornithine.[26,47] This is apparent in the mobility data shown in **Figure 18**, as evidenced by deviations in the $[GS + 2H]^{2+}(H_2O)_n$ trendline. The special stability of specific ions in the cluster population results in structural changes

during desolvation that are revealed in the 2-D mobility plot, particularly in regions surrounding the aforementioned magic number clusters. Certainly other factors contribute to the hydration behavior of peptides during the transition from solution to the gas phase, but the effects of specific versus nonspecific hydration on the formation of solvent-free ions are discernible from cryo-IM-MS and largely dependent on the ionic groups present.
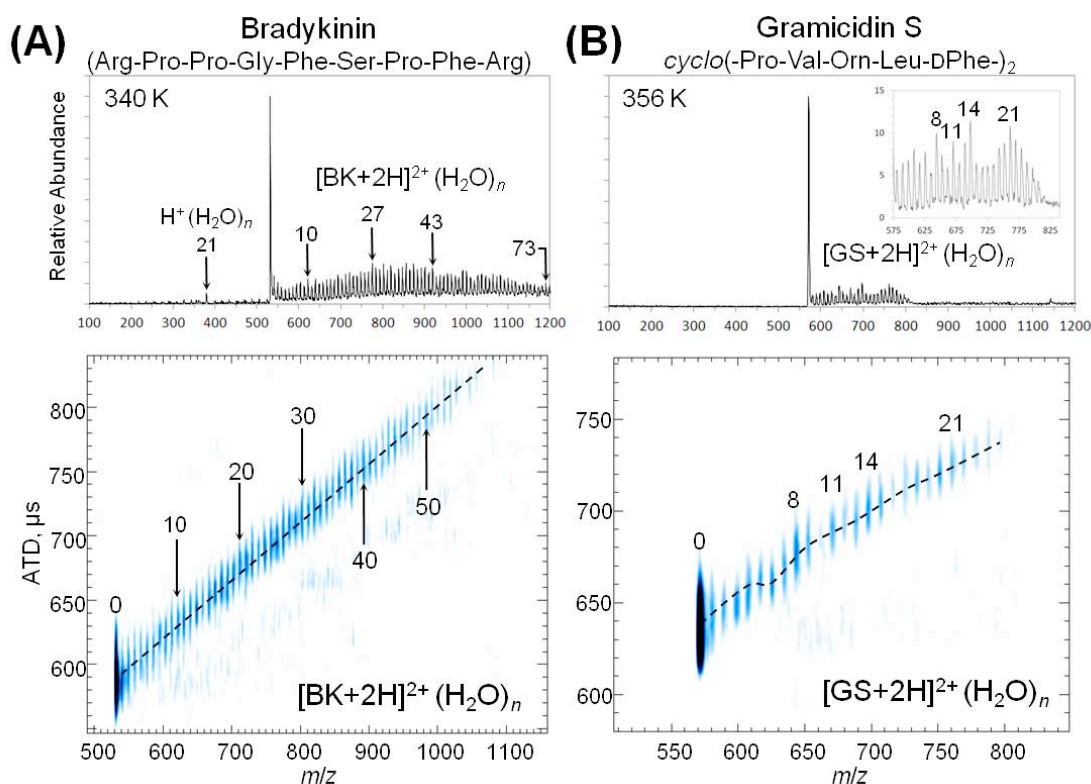
Figure 18. Mass spectra and 2-D contour plots of ATD versus *m/z* of hydrated [M + 2H]$^{2+}$ peptide ions of (A) bradykinin (BK) and (B) gramicidin S (GS). Hydration of bradykinin reveals a uniform trendline of hydrated clusters reflecting nonspecific hydration of the guanidinium ion of arginine. Hydration of gramicidin S reveals specific hydration of the ammonium ion of ornithine, as evidenced by the observation of magic number clusters and deviations in the dehydration IM trendline. The dashed lines were inserted to guide the eye along the IM-MS dehydration trendlines.

42

For biological molecules, hydration behavior will be dependent on not only the type of charge carrier present but also the number of charge sites and proximity to one another on the molecule. For multiply charged ions, Coulombic effects begin to complicate hydration behavior even further and can have a dominating effect on structure. Doubly-protonated diaminoalkanes provide an excellent model system to study the effects of Coulombic repulsion on hydration of the ammonium ion because the aliphatic chain length separating the two charged groups can be varied in a systematic manner without altering the overall structure of the molecule in any major way. As a result, multiple groups have previously performed hydration studies on alkyl diammonium cations. Kebarle and coworkers first showed evidence for the sequential attachment of the first few water molecules to alkyl diammonium cations and based on the binding energies found, determined that water molecules bind to both charged groups in an alternating fashion.[121,122] The formation of larger hydrated clusters revealed a preference for forming magic number clusters for hydrated ammonium ions, $NH_4^+(H_2O)_n$, as well as primary amines; specifically, $n = 20$ has been attributed to the formation of a clathrate cage structure similar to the compact structure of $H^+(H_2O)_n$ ($n = 21$).[69,123-127] However, the magic number cluster $n = 40$ has been absent from the spectra of many doubly protonated diammonium ions such as 1,12-diaminododecane and 1,7-diaminoheptane, suggesting that both charged groups on the ion may favor solvation by a single water droplet as opposed to separate solvation spheres.[123,128] Williams and coworkers used IRPD spectroscopy to analyze the sequential hydration of 1,7-diammoniumheptane with up to 30 water molecules attached and through a comparison

with the singly-protonated heptylamine ion, the authors determined that for clusters with >14 water molecules bound, the linear molecule begins to fold and a single droplet bridges both charged groups;[128] the suberate dianion exhibits similar behavior.[129] Computational studies confirmed such a folding transition exists for alkyl diammonium cations, but reports on the exact size of the droplet required to bridge the two charged groups have varied. Janhangiri *et al.* reported a similar water-induced folding transition using molecular dynamics (MD) simulations, but found evidence for this transition occurring at 22 water molecules for 1,7-diammoniumheptane and varying as a function of alkyl chain length.[130]

Cryogenic ion mobility-mass spectrometry (cryo-IM-MS) has previously been used to capture hydrated ions formed by electrospray ionization (ESI) for structural analysis.[26] Here, cryo-IM-MS is employed to measure changes in the structures of a series of hydrated doubly charged ions including 1,7-diaminoheptane (DAH), 1,8-diaminooctane (DAO), and 1,10-diaminodecane (DAD), as a function of the numbers (n) of attached water molecules. The cold cryo-IM-MS drift tube (80 K) facilitates the preservation of hydrated gas-phase ions and provides a way to track the structural evolution of these ions during the final stages of desolvation. Results presented herein show that hydrated alkyl diammonium cations undergo an abrupt unfolding transition upon stepwise desolvation over a narrow range of water molecules: ($n = 21$ to 23) for 1,7-DAH, ($n = 24$ to 26) for 1,8-DAO, and ($n = 27$ to 29) for 1,10-DAD.[131]

3.2 Experimental Methods

Heptylamine, 1,7-diaminoheptane (DAH), 1,8-diaminooctane (DAO), and 1,10-diaminodecane (DAD) were obtained from Sigma Aldrich (St. Louis, MO) and stored at -20 °C before being used without further purification. All solutions used for the studies discussed herein were prepared at a concentration of 500 μM with pure water (18 MΩ) containing 0.1% formic acid. The cryo-IM-MS instrument used for these studies has been described in detail previously and in Chapter 1.[26] Briefly, ions are generated via electrospray ionization and guided into the cryogenic IM drift tube, which is maintained at 80 ± 2 K via liquid nitrogen cooling, before being orthogonally pulsed into a time-of-flight mass spectrometer for detection and analysis. This approach is used to capture hydrated ions formed by ESI that are separated on the basis of size-to-charge (IM) and mass-to-charge (*m/z*). Cryogenic cooling of the drift tube to 80 ± 2 K is required for the preservation of these weakly bound hydrated cluster ions that have been shown to evaporate under ambient conditions.[26] The heated capillary ion inlet temperature was maintained between 338 and 349 K for all studies in order to control the extent of desolvation.

3.3 Results and Discussion

Figure 19(a-c) contains ESI mass spectra of 1,7-DAH, 1,8-DAO, and 1,10-DAD $[NH_3(CH_2)_xNH_3]^{2+}(H_2O)_n$ ions, where x = 7, 8, or 10, respectively. Spectra were collected at a heated capillary temperature between 338 and 349 K to facilitate desolvation. The relative abundances of the hydrated ions observed in the mass spectra

reflect the relative stabilities of specific cluster ions, as discussed in Chapter 1. Note that magic number clusters are not detected for the alkyl diammonium cations shown because both charged groups on the molecules prefer to be solvated by a single droplet at large numbers of n.[128] The peaks labeled with asterisks (see **Figure 19(a-c)**) fall at m/z values that correspond to either the dehydrated singly charged $[M + H]^+$ ion or a proton-bound dimer ion, $[2M + 2H]^{2+}$. Regardless, these ions appear to be formed by a different mechanism because hydrated forms of the ions are not observed in the mass spectra. A plausible mechanism for formation is by a charge reduction reaction to form $[M + H]^+$ ions, as was reported previously,[103] i.e., loss of $H^+(H_2O)_n$ ions via proton transfer from $[M + 2H]^{2+}(H_2O)_n$ ions.
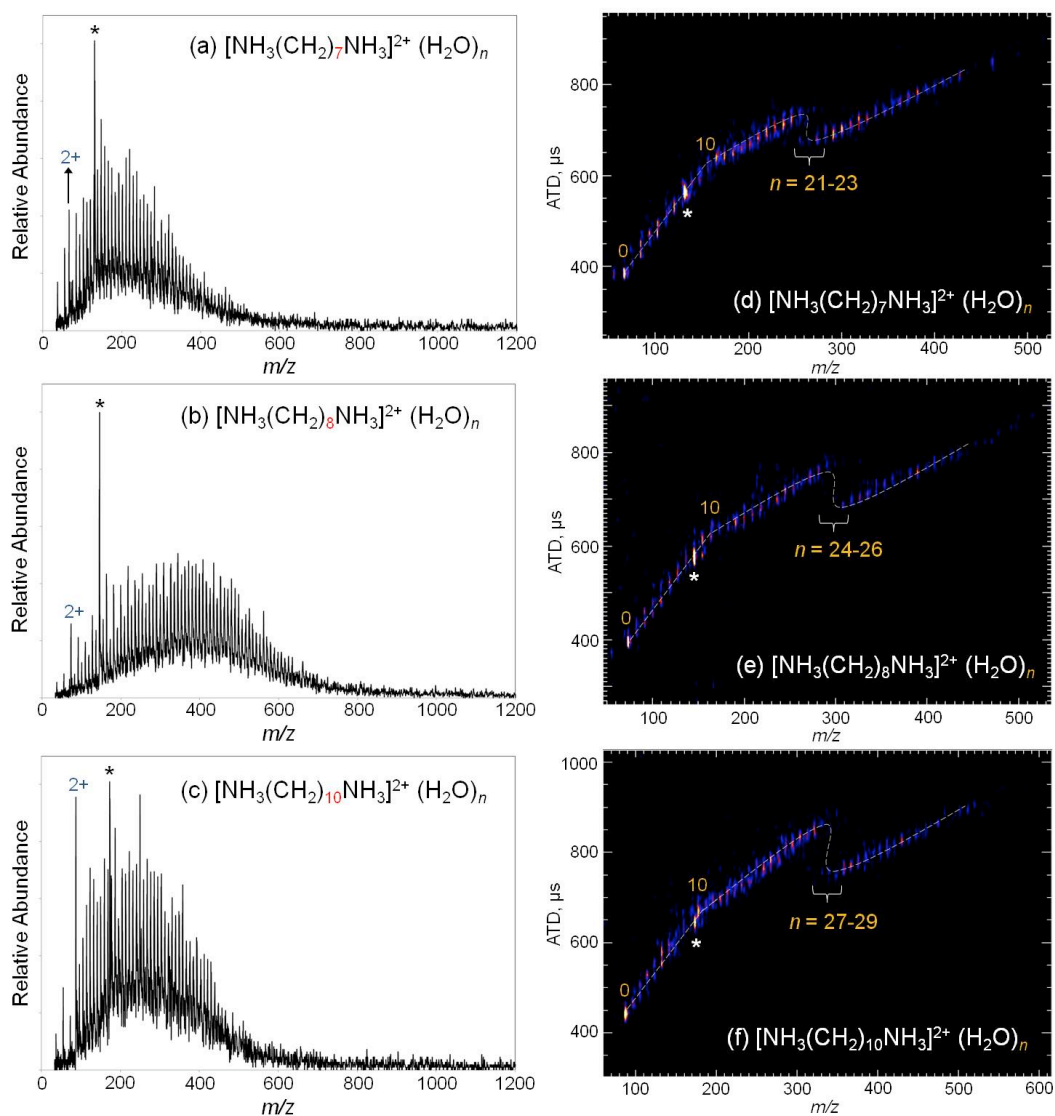
Figure 19. ESI mass spectra and 2-D contour plots of ATD versus m/z for $[M + 2H]^{2+}(H_2O)_n$ ions of (a, d) 1,7-DAH, (b, e) 1,8-DAO, and (c, f) 1,10-DAD. All solutions were prepared at a concentration of 500 μM with pure water (18 MΩ) containing 0.1% formic acid and the heated capillary ion inlet temperature was maintained between 338 and 349 K in order to control the extent of desolvation. The dashed lines are included to guide the eye along the IM-MS trendlines. The peaks labeled with an asterisk correspond to either the $[M + H]^+$ ion or a proton-bound dimer, $[2M + 2H]^{2+}$.

In order to investigate the conformational preferences of the doubly charged ions

as a function of the number of attached water molecules, two-dimensional contour plots

of ion mobility arrival time distribution (ATD) versus *m/z* were generated (**Figure 19(d-f)**). The mobility plots reveal a rather obvious discontinuity in the $[M + 2H]^{2+}(H_2O)_n$ ATD trendlines over a narrow range of water molecules for each dication. This deviation is consistent with an unfolding event upon stepwise dehydration for the $[M + 2H]^{2+}(H_2O)_n$ ions of each dication. For 1,7-DAH (**Figure 19(d)**), the ATDs for clusters *n* > 23 fall along a uniform trendline and the structures of these ions are attributed to a folded conformation in which both ammonium ions are solvated by a single droplet. The folded structure is stabilized on the surface of the droplet because energetically favorable solute-solvent interactions compensate for the Coulombic repulsion between the two charged groups and the water molecules effectively bridge between the two ammonium ions.[128] In this region, loss of sequential water monomers to evaporation results in minor changes to the overall structure of the molecule, as evidenced by the uniform trendline of hydrated cluster ions observed in the 2-D mobility plot. However, as the droplet continues to evaporate, it shrinks in size and repulsive Coulombic interactions between the charge sites force the solvated ion to elongate, splitting the water droplet into two clusters which solvate each ammonium ion separately. The resulting elongated ion conformation is accompanied by an increase in arrival time for the "unfolded" hydrated clusters, clearly evident in the mobility trendline shown in **Figure 19(d)**. An oversimplified cartoon demonstrating the unfolding transition for alkyl diammonium cations is shown in **Figure 20** for clarity. For 1,7-DAH, this transition occurs over the range (*n* = 21 to 23), consistent with the computational studies reported by Peslherbe and coworkers.[130] The longer alkyl chain lengths of 1,8-DAO and 1,10-DAD result in a shift

of the unfolding transition to larger cluster ions owing to the increased separation of charged groups in the molecule and subsequent increase in water molecules required to bridge between the ammonium ions. The 2-D plots shown in **Figure 18(e-f)** confirm that this is the case for 1,8-DAO and 1,10-DAD, as an identical transition is observed over the range ($n = 24$ to 26) and ($n = 27$ to 29), respectively.
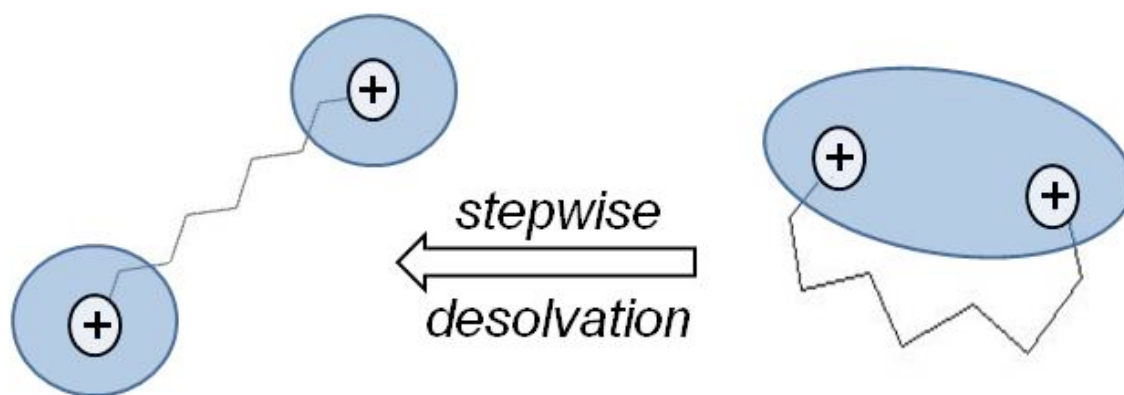
Figure 20. Schematic cartoon of unfolding transition undergone by $[M + 2H]^{2+}(H_2O)_n$ ions of 1,7-DAH, 1,8-DAO, and 1,10-DAD. Prior to unfolding, both ammonium ions are solvated by a single droplet (right). After the droplet solvating the ion undergoes stepwise desolvation during ESI and becomes smaller in size, the water droplet eventually undergoes a fission event and splits into two distinct droplets, solvating each charge site separately. This results in the observed elongation of the hydrated ion (left). The size threshold for this droplet fission event varies depending on alkyl chain length; longer alkyl chain lengths require larger numbers of water molecules to bridge between the ammonium ions.

The proposed transition, from a folded structure in which both ammonium ions are solvated by a single water cluster at larger numbers of n to an elongated structure in which the ammonium ions are solvated separately, was tested by comparing the hydration of heptylamine. The heptylammonium ion, $[CH_3(CH_2)_6NH_3]^+$, has a single ammonium group that will serve as the primary site of hydration; consequently, this ion

should not adopt a folded hydrated structure as was observed for the three diammonium cations.[128] The mass spectrum of heptylamine is shown in **Figure 21(a)** and both the $[CH_3(CH_2)_6NH_3]^+(H_2O)_n$ and $H^+(H_2O)_n$ series of hydrated clusters are formed by ESI and present in the spectrum. The 2-D mobility plot of $[CH_3(CH_2)_6NH_3]^+(H_2O)_n$ ions (**Figure 21(b)**) generated by cryo-IM-MS reveals a single hydration trendline tracing to the dehydrated ion. This trendline appears uniform in the region of ($n = 20$ to 30), indicating similarly structured conformer populations in this range that are consistent with elongated ion structures hydrated by a single solvation droplet around the ammonium ion.
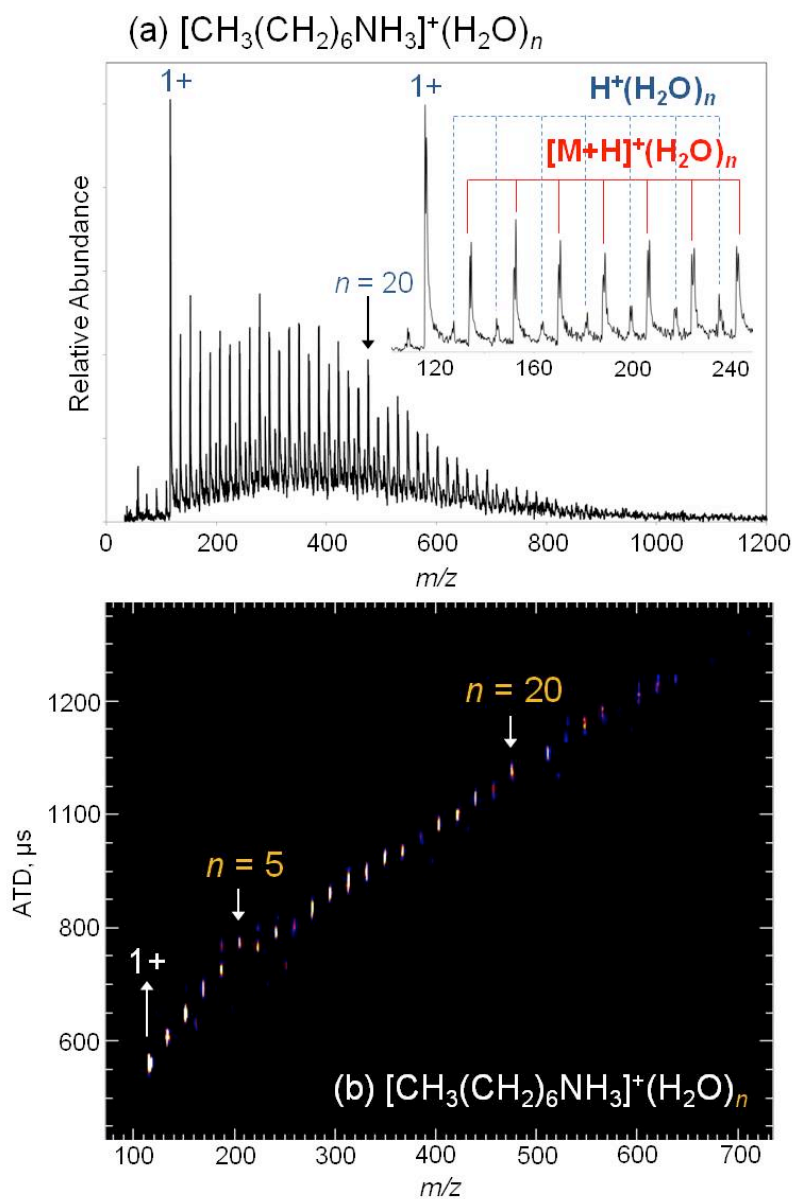
Figure 21. (A) ESI mass spectrum and (B) 2-D contour plot of ATD versus *m/z* for heptylamine $[CH_3(CH_2)_6NH_3]^+(H_2O)_n$ ions. The inset in panel (A) contains an expanded view of the region surrounding $[CH_3(CH_2)_6NH_3]^+(H_2O)_n$ (*n* = 0 to 7). In addition to hydrated heptylammonium ions, protonated water clusters are formed from ESI in small abundance.

The 2-D plot of the heptylammonium ion reveals a more subtle deviation in the trendline at (*n* = 5 to 6) that may shed light on a similar deviation observed in the low-

mass region of the spectra for the diammonium cations shown in **Figure 19**. There, a second structural transition is observed at ($n = 10$ to 11), evident from the abrupt change in slope observed for ATDs falling on the $[M + 2H]^{2+}(H_2O)_n$ trendlines. Previous cryo-IM-MS studies of protonated water clusters, $H^+(H_2O)_n$, elucidated structural transitions for small ions corresponding to changes associated with the evolution of the hydrogen-bond network around the excess proton.[79] Upon desolvation, clusters transitioned from 2-D net-type structures into elongated chain structures over the range ($n = 8$ to 11). This transition was characterized by the change in slope observed for ATDs along the hydration trendline indicating structural differences in the two types of clusters. Such a transition is predictable from spectroscopic results,[51,61,62] but the structural implications are directly revealed in the cryo-IM-MS hydration trendlines. The transition observed at $n = 10$ for 1,7-DAH, 1,8-DAO, and 1,10-DAD may result from a similar development of the H-bond network around the ammonium ion.

The deviation in the trendline of hydrated clusters is observed at ($n = 10$ to 11) for the diammonium cations whereas a similar deviation is observed at ($n = 5$ to 6) for the heptylammonium ion, a difference that is consistent with symmetric solvation of the two charged groups. This supports the assignment of these deviations to structural changes in the H-bond network surrounding the ammonium ion, consistent with interpretation of spectroscopic data. Williams and coworkers probed the free-OH stretch spectral regions of 1,7-DAH hydrated clusters and showed that bands associated with one-coordinated water molecules, which are present in chain-like structures, dropped off sharply at $n = 10$, whereas the band attributed to three-coordinated water molecules,

present in larger 2-D net structures, began to grow in simultaneously at $n = 9$.[128] This suggests that, for 1,7-DAH, the transition from chain-like structures into net-like structures should occur around $n = 10$, with five water molecules surrounding each charged group separately. IRPD spectra of hydrated heptylammonium clusters revealed a similar decrease in intensity of the free-OH stretches corresponding to one-coordinated water molecules at $\sim n = 5$ to 6.[128] Again, this is consistent with the transitions observed in the 2-D plots for the diammonium cations shown in **Figure 19**, as well as the deviation observed at $n = 5$ for the heptylammonium ion (**Figure 21**), which possesses only a single charged group.

Collectively, results indicate that the structural evolution of 1,7-DAH upon desolvation is characterized by multiple transitions. While the water-induced unfolding transition was predicted based on spectroscopic studies, results presented here definitively establish that the transition occurs at a specific, narrow range of water molecules. When greater than 23 water molecules are bound to the ion, it adopts a folded conformation in which both charged groups are brought into close proximity by solvation from a single droplet of water. Loss of water monomers through evaporation coupled with Coulombic repulsion then promotes the elongation and separation of the ammonium ions located on opposite ends of the molecule. This unfolding occurs abruptly over the range ($n = 21$ to 23) for 1,7-DAH and varies as a function of alkyl chain length. Clusters smaller than $[M + 2H]^{2+}(H_2O)_n$ ($n = 21$) exist as extended structures in which both charged groups are solvated by separate droplets. In this range, the water molecules solvating the ammonium ions form an interconnected network of H-

bonds made up of two- and three-coordinated water molecules. Beginning at $n = 10$, loss of water monomers results in expansion of the net-type hydrated ions into chain-like structures possessing one-coordinated water molecules. This transition has been previously observed for protonated water clusters, $H^+(H_2O)_n$, but is shown to occur over a different range indicating subtle differences between hydration of the ammonium and hydronium ions.

3.4 Conclusions

Cryo-IM-MS is employed to study the structural evolution of a series of alkyl diammonium cations during the final stages of desolvation. Results indicate that the dications transition from a folded conformation hydrated by a single water droplet to an extended conformation hydrated by two separate droplets across a narrow range of water molecules. While this unfolding transition is driven by Coulombic repulsion of the two charged groups, it is shown to vary as a function of alkyl chain length as unfolding occurs at ($n = 21$ to 23), ($n = 24$ to 26), and ($n = 27$ to 29) for 1,7-DAH, 1,8-DAO, and 1,10-DAD, respectively. In addition to gaining insight into the Coulombic effects on the hydration behavior of multiply charged ions, the investigation of these systems using cryo-IM-MS elucidated the structural changes associated with the evolution of the H-bond network around the ammonium ion. The transitions observed at $n = 10$ and $n = 5$, for the dications and monocation respectively, reveal that water molecules bound to the ammonium ion evolve from chain-like structures for small clusters ($n < 5$) into 2-D net structures for larger clusters. The ammonium ion is present in a wide range of peptides

54

and proteins and plays an essential role in the structural preferences of these molecules, especially in the presence of water. Understanding the hydration behavior and conformational changes of small systems as a function of the number of waters attached will provide a simple system to model the behavior of more complex biological molecules.

4. FROM SOLUTION TO THE GAS PHASE: CRYOGENIC ION MOBILITY-MASS SPECTROMETRY REVEALS ORGIN OF PEPTIDE CONFORMATIONS PRODUCED DURING ELECTROSPRAY IONIZATION

4.1 Background

As biomolecules transition from solution to the gas phase via ESI, a number of competing effects, including both inter- and intramolecular interactions, will dictate structural preferences. Recent studies have shown that under cool instrument conditions, gas-phase biomolecular ions can retain the solution phase structure(s) of their hydrated counterparts,[35,36,44,97,132,133] suggesting that the evaporative cooling effects of ESI can lead to the kinetic-trapping of ions in local minima along their potential energy surface. However, this observation will be dependent on the specific interactions contributing to the stabilization of different peptides/proteins, and whether these interactions will retain stability in the absence of solvent. Although efforts have been made to model the final stages of the ESI process using molecular dynamics (MD) simulations,[32] the exact mechanism by which gas-phase ions emerge from solution is still debated due to limited experimental techniques available to probe this process. Cryo-IM-MS provides a means to capture extensively hydrated biomolecules and elucidate any conformational changes that may occur during the desolvation process of ESI. When coupled with molecular modeling, it becomes a very powerful approach for studying the evaporative dynamics of biomolecular ions. In the case of the neuropeptide substance P (SP) (Arg-Pro-Lys-Pro-Gln-Gln-Phe-Phe-Gly-Leu-Met-NH$_2$), initial hydration data revealed that a solution-

like structure could be preserved in the gas phase by means of kinetic trapping, despite the existence of a more extended, energetically favorable gas-phase conformation.[78,102]

4.2 Experimental Methods

4.2.1 Sample Preparation

Substance P (SP) (RPKPQQFFGLM-NH$_2$) was purchased from American peptide (95% purity, Sunnyvale, CA) and used without further purification. Substance P mutant peptides Q5A (80% purity), Q5,6A (83% purity), F7,8A (84% purity), and Q5,6A F7,8A (95% purity) were purchased from either Mocell Biotech Co. (Shanghai, China) or Gen Script (Piscataway, NJ). The notation used for SP mutant peptide ions (SP$_M$) denotes the original residue and position number, followed by the new, substituted residue. For example, the notation Q5A denotes that glutamine at position 5 has been replaced by alanine (RPKPAQFFGLM-NH$_2$). A list of substance P mutant peptides with each corresponding sequence is shown in **Table 1**. Each peptide was diluted in 1 mL of deionized water (18 MΩ) and stored at -20 °C before solutions were prepared. For room temperature studies, solutions were prepared at concentrations ranging between 10 and 50 μM in solutions of 89:10:1 H$_2$O:MeOH:acetic acid. For cryogenic studies, solutions were prepared at 50 μM in pure water with 0.1% formic acid.

Table 1. A list of substance P mutant peptides, including peptide abbreviations and sequences. Native amino acid residues that have been mutated with alanine are shown in red and underlined.

Peptide	Sequence
SP	RPKPQQFFGLM-NH$_2$
Q5A	RPKP<u>A</u>QFFGLM-NH$_2$
Q5,6A	RPKP<u>AA</u>FFGLM-NH$_2$
F7,8A	RPKPQQ<u>AA</u>GLM-NH$_2$
Q5,6A F7,8A	RPKP<u>AAAA</u>GLM-NH$_2$

4.2.2 Instrumentation

The cryo-IM-MS instrument is described in detail in Chapter 1. All room temperature, collisional activation studies were carried out on a high-resolution home-built IM-MS instrument.[134] The instrument consists of an ESI source, periodic focusing ion funnel (PF IF), 1.38 m long periodic focusing drift tube, and orthogonal time-of-flight mass analyzer. For collisional activation studies, ions were activated in the PF IF, prior to entering the drift tube for IM separation. The electric field in the ion funnel ranged from 11 to 43 V cm^{-1} Torr^{-1}. Collision cross section (CCS) values from a periodic focusing field were determined using a method described elsewhere,[135] and all values

reported show excellent agreement (within 2%) with ion-helium CCS values measured using a high-resolution uniform field IM-MS instrument.[136]

4.2.3 Molecular Dynamics Simulations

AMBER 11 and GAUSSIAN 03 were used to perform molecular dynamics (MD) simulations and quantum mechanics (QM) simulations. GAUSSIAN 03 (HF/6-31+) was used to optimize the structure of custom residues and charge fitting was performed using the R.E.D. III program.[137] The AMBER FF99SB force field was used for common residues. For the triply charged SP ion, protonation sites were the N-terminus, the guanidine group of arginine, and the ε-amino group of lysine. MD simulations were carried out at temperatures between 300 and 550 K. Candidate structures were also generated via multiple simulated annealing runs that involved multiple heating and cooling cycles that involved ramping the temperature between 300 and 1000 K over the course of 5 ns. Clustering statistical analysis was performed on the structures generated,[138] and CCS values for the simulated structures were calculated using MOBCAL.[81]

4.3 Results and Discussion

4.3.1 Substance P Hydration Behavior

An ESI mass spectrum of substance P (SP) is shown in **Figure 22(a)**. Both the doubly and triply charged ions are present, hydrated by a significant number of water molecules ($n = \sim 50$) each. To gain insight into the structural evolution of SP ions during

dehydration, cryo-IM-MS is employed. Mobility data for $[SP + 2H]^{2+}(H_2O)_n$ reveals a single conformer population, the structure of which does not appear to vary as a function of dehydration (data not shown). Mobility data for $[SP + 3H]^{3+}(H_2O)_n$, however, shows two distinct conformer populations (**Figure 22(b)**), one that traces from a trendline of hydrated ions (labeled **A**) and a second at longer drift times that has no associated hydrated ions (labeled **B**). The compact conformer **A** appears to be formed by stepwise evaporation of extensively hydrated ions, and the uniform trendline suggests that the structure of the bare-ion closely resembles the structure of its hydrated counterparts. Conformer **B** falls at longer drift times and is therefore more elongated, but its origin is initially unclear. The absence of a dehydration trendline tracing to conformer **B** suggests that there are two possibilities for formation of the elongated conformer population. The first possibility is that conformer **B** could be formed by an alternate mechanism of ESI, the ion evaporation model (IEM).[32,38,39] As discussed in Chapter 1, the IEM involves the ejection of an ion from an intact nanodroplet, as opposed to the sequential dehydration process of the charge residue model (CRM).[30,33] Therefore if conformer **B** were formed by the IEM, there should be no hydrated ions associated with the 3+ ion in the range shown in **Figure 22(b)**. Alternatively, a second possibility for ion formation is that conformer **B** originates from a structural rearrangement of conformer **A** that occurs after complete desolvation. Both scenarios are depicted in the schematic shown in **Figure 23**.
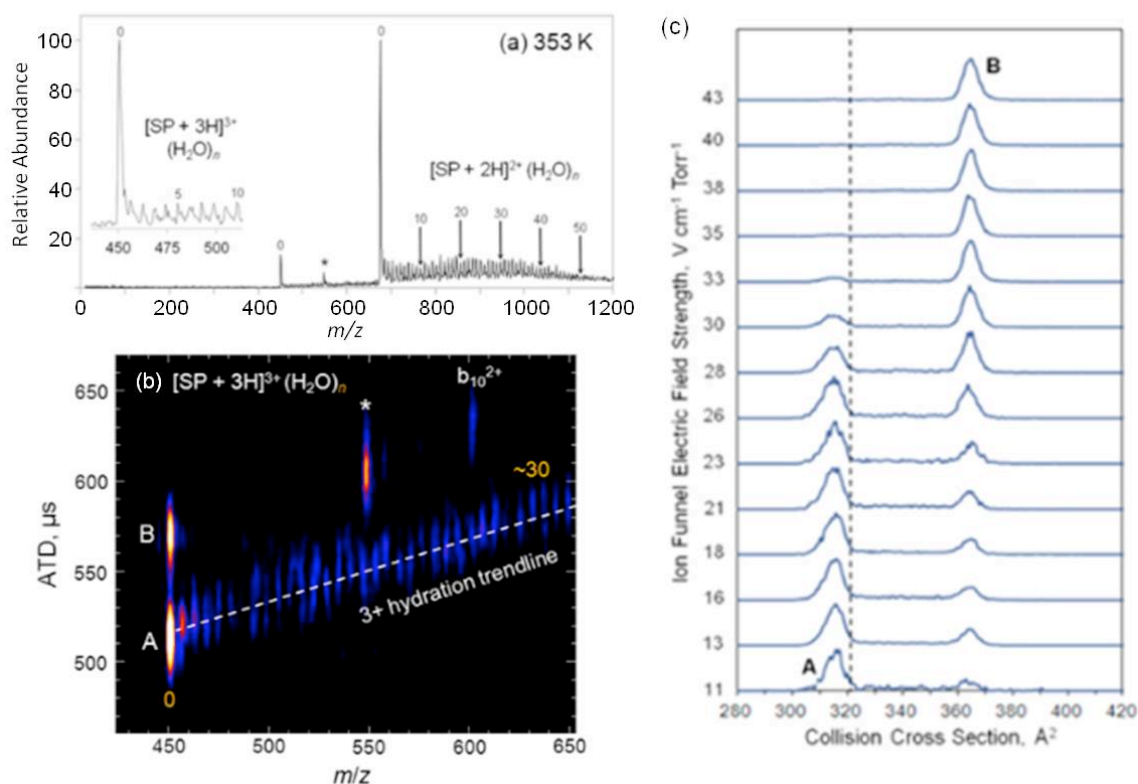
Figure 22. IM-MS data for substance P (SP) $[M + 3H]^{3+}$ ions. (a) Mass spectrum of SP ions collected at a heated capillary temperature of 353 K; the inset contains an expanded view of the region $[SP + 3H]^{3+}(H_2O)_n$ ($n = 0$ to 10). (b) Two-dimensional plot of ATD versus m/z for $[SP + 3H]^{3+}$ ions collected at a heated capillary temperature of 356 K. Conformer assignments are denoted **A** and **B** and the trendline of hydrated ions is traced with a dashed line to guide the eye. The peak labeled with an asterisk is a contaminant ion. (c) Mass-selected collision cross section profiles (CCS) for $[SP + 3H]^{3+}$ ions obtained on an ambient-temperature high-resolution IM-MS instrument. Ions were activated in a periodic focusing ion funnel via collisions with He buffer gas prior to IM analysis; CCS profiles are shown as a function of electric field in the ion funnel. At low field strengths, the kinetically-trapped conformer **A** is observed, and upon collisional activation, the elongated conformer **B** is formed. The dashed line at 321 Å^2 represents the theoretical random coil trendline for reference.
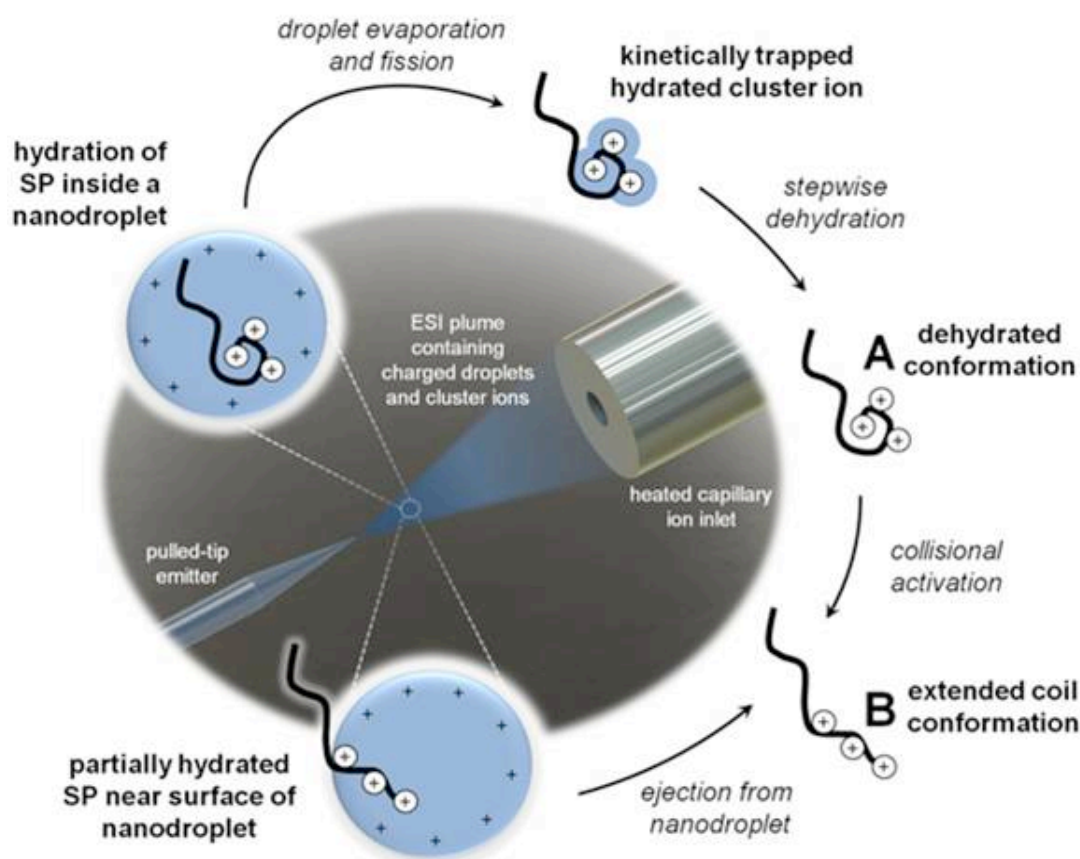
Figure 23. Schematic of two potential mechanisms for the dehydration of $[SP + 3H]^{3+}$ ions from bulk solution via ESI. The charge residue model (CRM), shown in the top route, describes the production of gas-phase ions by fission of large droplets followed by stepwise evaporation of solvent from $[SP + 3H]^{3+}$ ions. In this model, conformer **A** retains stability through complete desolvation before converting to conformer **B**. The ion evaporation model, shown in the bottom route, is favored for small molecules and produces ions by a field desorption process. In this hypothetical model, conformer **B** is formed via ejection from a nanodroplet. In both cases, charged nanodroplets containing SP are produced in the ESI plume and ultimately yield solvent-free gas-phase ions.

In order to test the latter hypothesis, collisional activation studies were carried out at ambient temperature on a home-built 1.38-m IM-MS instrument.[134] $[SP + 3H]^{3+}$ ions were collisionally heated in a periodic focusing ion funnel (PF IF) prior to IM-MS analysis. Results from the heating studies depicted in **Figure 22(c)**, show that primarily

conformer **A** is formed at low field strengths and upon activation, conformer **A** (318 Å) depopulates and elongates to form conformer **B** (368 Å). The experimentally determined CCS values show good agreement to previous studies.[135,139] The collective results suggest that conformer **B** is formed by a structural rearrangement of conformer **A** and not by an alternative ESI mechanism, although it is worth noting that we were unable to experimentally test whether or not ions could be formed by the IEM mechanism. Therefore, $[SP + 3H]^{3+}$ ions are shown to be formed by the CRM mechanism and the transition from bulk solution to the gas phase involves the formation of a compact conformer (**A**) that is kinetically trapped and remains stable throughout the desolvation process (loss of last ~50 water molecules). Upon complete desolvation and subsequent activation, the kinetically-trapped conformer rearranges and elongates to form the more extended conformer **B**, a thermodynamically stable gas-phase ion conformation. The presence of multiple conformations of $[SP + 3H]^{3+}$ ions is consistent with previous NMR and mass spectrometry studies.[140-143]

4.3.2 Factors that Influence Kinetic Trapping of Substance P Ions

    The high-degree of stability observed for the compact conformer population **A** throughout the desolvation process suggests that the structure must be stabilized by interactions other than hydrogen bonds (H-bond) with surrounding water molecules. Due to the localization of the three charge sites near the N-terminus of the molecule (R^1, K^3, and N-terminus), we hypothesize that the protonated side chains of both lysine and arginine may participate in H-bonding interactions with glutamine (Q^5/Q^6) or pi-cation

interactions with phenylalanine (F^7/F^8). Such interactions would stabilize a highly localized charge center on a small peptide ion and would explain the observed kinetic trapping of conformer **A** on the timescale of the experiment (several milliseconds). One way to experimentally determine the contribution of each residue to stability, through the participation in intramolecular charge solvation, is to perform systematic mutations of native amino acids in the sequence for alanine. Replacement by alanine should effectively eliminate the possibility of H-bonding at that site and will introduce minimal steric effects to the peptide.[102,139] A series of SP mutant ions were purchased in which residues Q^5/Q^6 and F^7/F^8 were replaced by alanine (**Table 1**). Mutant Q5,6A eliminates glutamine in positions 5 and 6 as possible H-bonding sites, while mutant F7,8A does the same for phenylalanine in positions 7 and 8. Mutant Q5,6A F7,8A should combine the two effects and eliminate all possible interactions with those residues.

CCS profiles for $[M + 3H]^{3+}$ ions of SP and SP mutants (Q5,6A, F7,8A, and Q5,6A F7,8A) are shown in **Figure 24**, as a function of field strength in an ion funnel where activation occurs. All spectra were collected on the 1.38-m IM-MS apparatus at ambient temperature.[102] The bottom plot for each peptide ion shows the CCS profile collected under moderate activation conditions. As shown previously, SP initially forms primarily conformer **A** from desolvation, and upon activation, conformer **A** rearranges and elongates to form conformer **B**. When both glutamines are mutated out in Q5,6A, the abundance of conformer **A** decreases substantially relative to SP. When the glutamines are eliminated as possible interaction sites, the compact conformer **A** is destabilized resulting in the formation of primarily conformer **B**. The small remaining

abundance of $\mathbf{A}$ indicates that while Q^5/Q^6 contribute to the stability of $\mathbf{A}$ significantly, other interactions must help stabilize the kinetically-trapped conformation as well. It is likely that these other interactions include pi-cation interactions between the charge sites and F^7/F^8. In the CCS profile for mutant F7,8A, the abundance of conformer $\mathbf{A}$ is again decreased relative to SP, but not as severely as was seen for the Q5,6A mutant. This suggests that the charge sites can interact with both Q^5/Q^6 and F^7/F^8, but interactions with the latter provide less stability than those with the former. The data also reveal that the peak widths for conformer $\mathbf{A}$ are reduced upon mutation (both Q5,6A and F7,8A) reinforcing the notion that the conformational heterogeneity of $\mathbf{A}$ decreases once specific interaction sites are removed. It is worth noting that single-point mutations, including Q5A, Q6A, F7A, F8A, were also analyzed to determine the individual residue contributions to stability, but the results are not shown here as the double residue mutations had a larger effect on destabilization in both cases.[102] Data for the mutant Q5,6A F7,8A reveal only a single conformer population (**Figure 24**), and due to the lack of variance upon activation, it was assigned to an elongated conformer similar in structure to conformer $\mathbf{B}$ for SP.
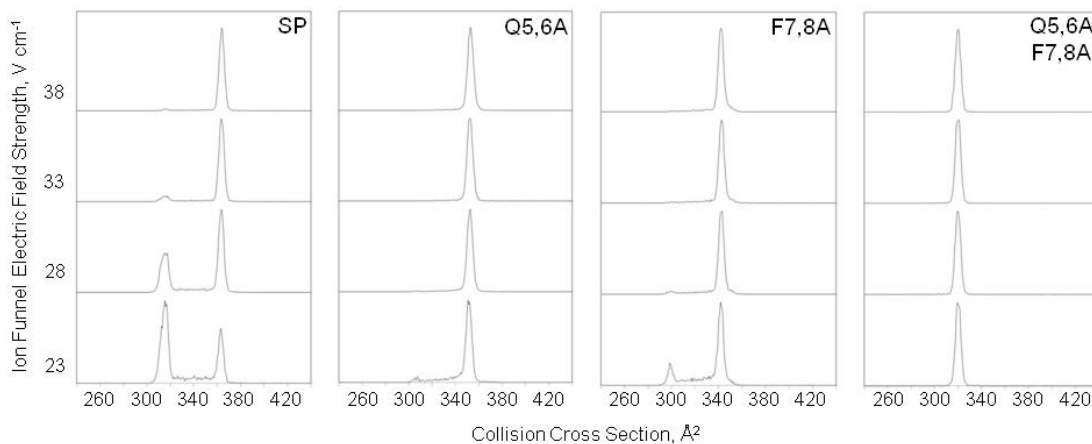
Figure 24. The CCS profiles of SP and mutant ions Q5,6A, F7,8A, and Q5,6A F7,8A shown as a function of electric field in a periodic focusing ion funnel (PF IF). For Q5,6A F7,8A, the absence of any structural variation upon collisional activation indicates that the profile observed represents the extended conformer **B**. Mutation of glutamines and phenylalanines results in the destabilization of conformer **A**.

Interestingly, mass spectra of SP mutant ions (discussed further in Chapter 5) reveal a decrease in the abundance of the $[M + 3H]^{3+}$ ions upon mutation indicating that the intramolecular interactions between the charge sites and Q^5/Q^6 and F^7/F^8 may be critical to formation of the $[M + 3H]^{3+}$ ion during ESI. It is likely that intramolecular solvation of the charge sites by glutamine and phenylalanine serves to stabilize the three localized charges on the N-terminus of SP ions. Once the ions are subjected to mild collisional activation, the intramolecular interactions are disrupted leading the compact conformer **A** to elongate and form conformer **B**. The elimination of intramolecular interactions by mutation will undoubtedly increase the Coulombic repulsion between charge sites in the triply charged ion, which may ultimately result in decreased structural stability. The implications of this on the evaporative dynamics of SP ions are discussed further in Chapter 5.

66

MD simulations were performed to generate candidate structures for both conformers **A** and **B** of SP and the mutant Q5,6A.[78,102] The structures generated for SP (conformer **A**) (**Figure 25(a)**) reveal H-bond interactions between K^3 with Q^5/Q^6 (highlighted in red) in addition to interactions between the ammonium ion on the N-terminus with the amide C-terminus. While not visible here, alternate structures generated showed evidence for H-bond interactions between the guanidinium ion of R^1 with Q^5/Q^6. The structure for Q5,6A (**Figure 25(c)**) shows that once the glutamine residues are replaced and no longer available as interaction sites, the ammonium ion of K^3 now prefers to interact with phenylalanine residues F^7 or F^8. There also still appears to be interaction between the N-terminus ammonium ion with the amide C-terminus. Representative structures for conformer **B** for both SP (**Figure 25(b)**) and Q5,6A (**Figure 25(d)**) show that elongation results from disruption of intramolecular interactions and projection of the side chains of R^1 and K^3 outward from the molecule. It is likely that this elongation results from Coulombic repulsion between charge sites once they cease to be stabilized through intramolecular solvation.

67
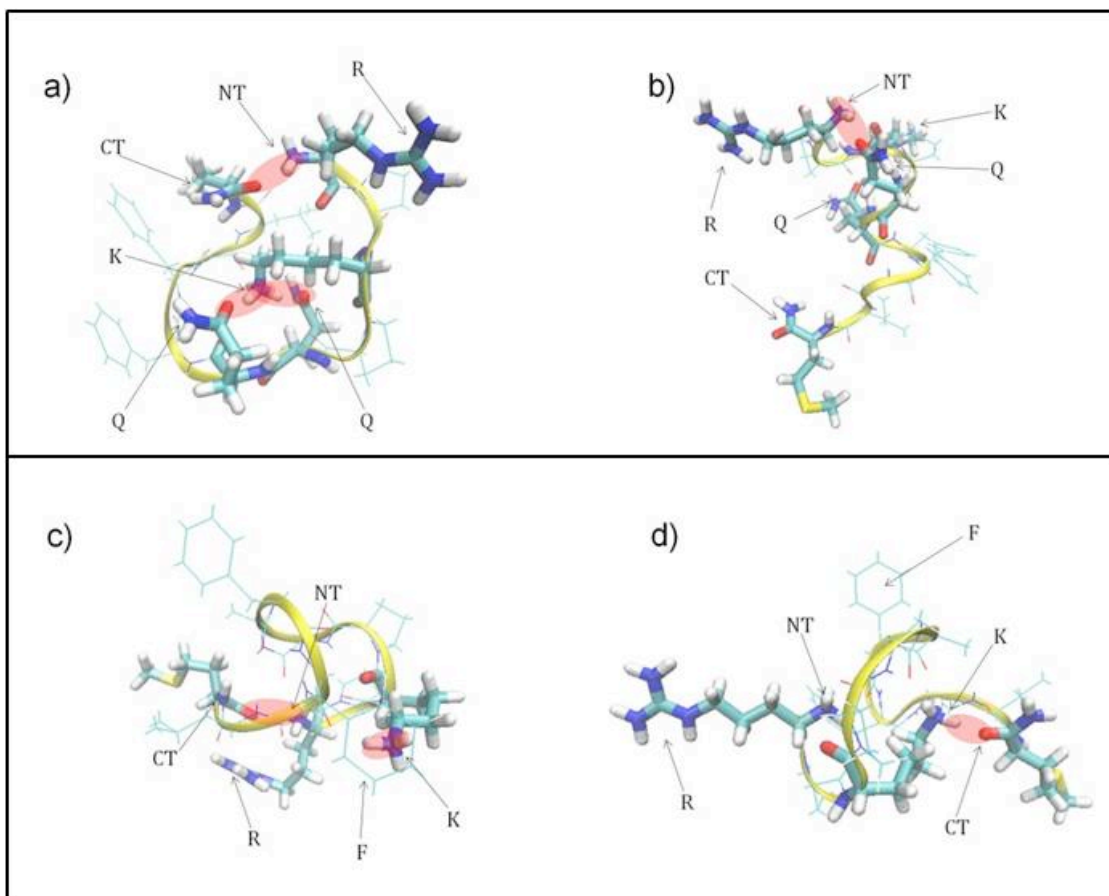
Figure 25. Representative structures determined by molecular modeling for conformers **A** and **B** for SP and Q5,6A $[M + 3H]^{3+}$ ions: (a) $\mathbf{A}_{SP}$, (b) $\mathbf{B}_{SP}$, (c) $\mathbf{A}_{Q5,6A}$, and (d) $\mathbf{B}_{Q5,6A}$. Conformer $\mathbf{A}_{SP}$ is compacted due to stabilization from interactions between K^3 and Q^5/Q^6 and also the N-terminus (NT) and C-terminus (CT). When glutamine is substituted for alanine in the Q5,6A mutant, the compact conformer is only stabilized by interactions between the NT and the CT and between K^3 with F^7/F^8. In both cases, Coulombic repulsion leads to disruption of these stabilizing interactions and the ions rearrange to form the more extended conformer **B** (shown in b and d). The intramolecular interactions discussed are highlighted in red on the structures and important residues participating in such interactions are labeled.

4.4 Conclusions

A combination of cryo-IM-MS and site-specific amino acid mutation has been utilized to trace the origins of peptide conformations for $[SP + 3H]^{3+}$ ions. Results

showed that a kinetically-trapped, compact conformer could be stabilized through complete desolvation owing to strong intramolecular interactions present. Upon activation, this dehydrated conformer population elongates to form an energetically favorable gas-phase conformation. Analysis of a series of mutant ions in which native amino acid residues were replaced by alanine revealed that the kinetically-trapped conformer was stabilized by interactions between the charge sites (R^1, K^3, and the N-terminus) and Q^5/Q^6 or F^7/F^8. Glutamine residues Q^5/Q^6 appear to contribute to the stability of conformer **A** to a greater extent than phenylalanine residues F^7/F^8. However, all four residues were crucial, in varying extents, to formation of the kinetically-trapped conformer as each mutation resulted in an observed decrease in the abundance of the conformer **A** population relative to native SP. This was due to a decrease in conformer heterogeneity that arises from elimination of specific intramolecular interactions through mutation. Overall, the collective results indicate that intramolecular charge solvation can play a dominating role in stabilizing ion structure during desolvation and cryo-IM-MS provides a method that can be used to unravel these contributions and track the structure(s) of biomolecules during this process.

5. FROM SOLUTION TO THE GAS PHASE: THE IMPLICATIONS OF INTRAMOLECULAR INTERACTIONS ON THE EVAPORATIVE DYNAMICS OF SUBSTANCE P DURING ELECTROSPRAY IONIZATION[*]

5.1 Background

Gas-phase techniques, including ion mobility-mass spectrometry (IM-MS), can generate an abundant amount of structural information about biological molecular ions, but interpreting the relevance of these structural features and relating them to solution phase structures can be quite complicated.[9,35,36,44,97,132,133,144-146] For studies of peptide/protein ion structure, a key question aims at determining the extent to which solution or "native-like" structure(s) can be retained upon transfer to the gas phase by electrospray ionization (ESI).[34,37,78,100,101,147] A number of factors govern the structural evolution of peptide/protein ions during the transition from solution, via the evaporative processes of ESI, to the formation of solvent-free, gas-phase ions. During the early stages of the ESI process, solute-solvent interactions are likely the major determinants of structure, but as the numbers of solvent molecules are reduced, the importance of intramolecular interactions is expected to increase. Although previous molecular dynamics (MD) simulations and experimental studies have provided evidence that peptide and protein ions can retain their solution structure upon transfer to the gas

phase,[34,37,101] this is critically dependent on the factors that stabilize these structures, specifically, the interplay between the intermolecular interactions provided by solvent and co-solvents and electrostatic intramolecular interactions (hydrogen bonds and/or salt bridges) that afford stability to solvent-free ions.

The combination of ESI and cryogenic ion mobility-mass spectrometry (cryo-IM-MS) adds a new dimension to studies of biomolecule ions, *viz.* the ability to generate ions that are hydrated by specific numbers of solvent molecules while maintaining the ability to measure the size/shape of the individual ions. It is generally agreed that ESI produces "cold" ions by evaporative cooling during desolvation, a process similar to freeze-drying, and that in the absence of post-ESI heating, ions can remain "cold" for long periods of time.[42,72,148] The cryo-IM-MS drift cell, which is maintained at 80 K, captures the "freeze-dried" ions and provides additional cooling upon entering the drift cell. The low temperature environment affords detection of solvated gas-phase ions for IM analysis.[26,78] This approach provides a means to experimentally monitor snapshots of the structural evolution of biomolecule ions during the final stages of the evaporative processes of ESI.

The exact mechanism by which ESI produces gas-phase ions and whether structural changes occur as a result of desolvation are still debated. According to the charge residue model (CRM), which is predicted to occur for large protein ions, charged analyte droplets undergo fission events to yield small nanodroplets containing a single analyte ion and stepwise dehydration of these small droplets produces dehydrated gas-phase ions.[30-33,149,150] By preserving hydrated analyte ions for study, cryo-IM-MS

provides a way to experimentally determine the effect of dehydration on the structures of biomolecules. We have previously shown that $[M + 3H]^{3+}$ ions of substance P (SP) are formed by the CRM and that these ions do not undergo significant structural changes during the final steps of desolvation (**Scheme 5**).[78]

$$[SP + 3H]^{3+}(aq.) \xrightarrow{droplet\ evaporation\ and\ fission} [SP + 3H]_A^{3+}(H_2O)_{n\lesssim30}$$

$$\xrightarrow{stepwise\ dehydration} [SP + 3H]_A^{3+} \xrightarrow{activation} [SP + 3H]_B^{3+} \xrightarrow{activation} fragments \tag{5}$$
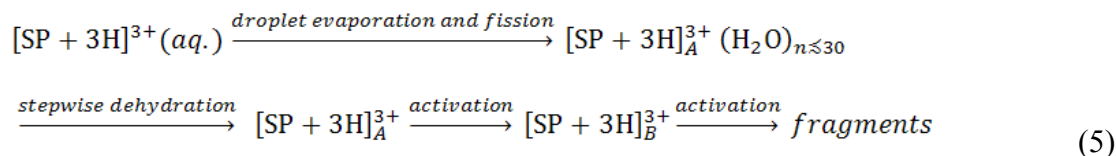
Although SP has been shown to be largely unstructured in bulk solution,[141] evaporative cooling ("freeze-drying") upon solvent evaporation kinetically traps a compact population of conformers, which are stabilized via intramolecular interactions.[78] These compact, kinetically-trapped conformers retain stability until stepwise desolvation to form the dehydrated ion; however, upon collisional heating in the gas phase, these conformers rearrange to form a thermodynamically stable extended conformation.[102,151] The most important intramolecular interactions that facilitate kinetic trapping of the compact conformers were shown experimentally to involve the charge sites and the side chains of the glutamine residues located at positions five and six.[102] The structural evolution of SP during the evaporative processes of ESI is driven by the interplay between the intermolecular solvation provided by water in solution and the intramolecular interactions that are formed as the water molecules evaporate. Here, amino acid mutations that are designed to eliminate key intramolecular interactions are used to better understand the evaporative dynamics and conformational preferences of SP ions during the final stages of desolvation en route to forming the solvent-free ion.[103]

5.2 Experimental Methods

5.2.1 Sample Preparation

     SP was purchased from American Peptide (95% purity, Sunnyvale, CA) and the SP mutant peptides Q5A (80% purity), Q5,6A (83% purity), and Q5,6A F7,8A (95% purity) were purchased from either Mocell (Shanghai, China) or Gen Script (Piscataway, NJ). The notation and sequences of SP and SP mutant peptides are outlined in **Table 1**. Each peptide was diluted in 1 mL of deionized water (18 MΩ) and stored at -20°C before 50 μM solutions of each were prepared with pure water containing 0.1% formic acid.

5.2.2 IM-MS Measurements

     All arrival time distributions (ATDs) and mass spectra (MS) presented herein were collected on the home-built cryo-IM-MS instrument that has been described in detail in Chapter 1.[24,26,79] Briefly, hydrated ions are produced from an electrospray source and guided into a variable-temperature drift tube that is maintained at 80 K via N_2 (*l*) cooling. The cold conditions preserve hydrated ions on the timescale of the experiment and the ion inlet (heated capillary) temperature is used to control the extent of hydration. Once inside the drift tube, ions are separated based on their respective mobility and orthogonally pulsed into a time-of-flight mass spectrometer for detection and analysis.

5.3 Results and Discussion

The intramolecular interactions that lead to kinetic trapping of the compact conformer population (denoted **A**) for $[SP + 3H]^{3+}$ ions have previously been identified using molecular dynamics (MD) simulations and amino acid mutations and are elaborated on in Chapter 4.[78,102] The most important interactions involve the charge sites, i.e., the N-terminus and the side chains of arginine and lysine, with the side chains of glutamine residues at positions five and six. At reduced drift fields, **A** can be preserved in small abundance even when the glutamine residues are replaced by alanine, which is interpreted as evidence for additional stabilization provided by π-cation interactions involving phenylalanine residues at positions seven and eight. At ambient temperatures, the destabilization of these intramolecular interactions promoted conversion to the elongated conformation **B**; however, the reduced temperatures provided by cryo-IM-MS (80 K) appear to have a more pronounced effect on the formation of $[SP + 3H]^{3+}$ ions during the final stages of desolvation.

5.3.1 Evaporative Dynamics of Substance P and Substance P Mutant Ions

Figure 26 contains mass spectra of SP and SP mutant ions Q5A, Q5,6A, and Q5,6A F7,8A. The notation used for SP mutant peptide ions (SP_M) was described in Chapter 4; for example, the notation Q5A denotes that glutamine at position five has been replaced by alanine (RPKPAQFFGLM-NH$_2$).[102] Extensive amino acid mutations were previously employed to determine the contribution of each residue to the overall stability of the kinetically-trapped conformers of $[SP + 3H]^{3+}$.[102] Based on those results,

the mutant ions shown in **Figure 26** best illustrated the stepwise destabilization of the kinetically-trapped species. The mass spectra collected on the cryo-IM-MS instrument reveal that mutation of the glutamine and phenylalanine residues results in a significant decrease in the abundance of $[SP_M + 3H]^{3+}$ ions relative to that of $[SP_M + 2H]^{2+}$ ions. Clearly, the intramolecular interactions involving Q^5/Q^6 as well as F^7/F^8 afford stabilization of conformer **A**, and elimination of these interactions reduces, even eliminates, the ability to produce $[SP_M + 3H]^{3+}$ ions. This effect is most evident at low temperatures (80 K) where the rate of desolvation is slow, thus dehydration and the mechanism for formation of $[SP_M + 3H]^{3+}$ ions may be directly linked.
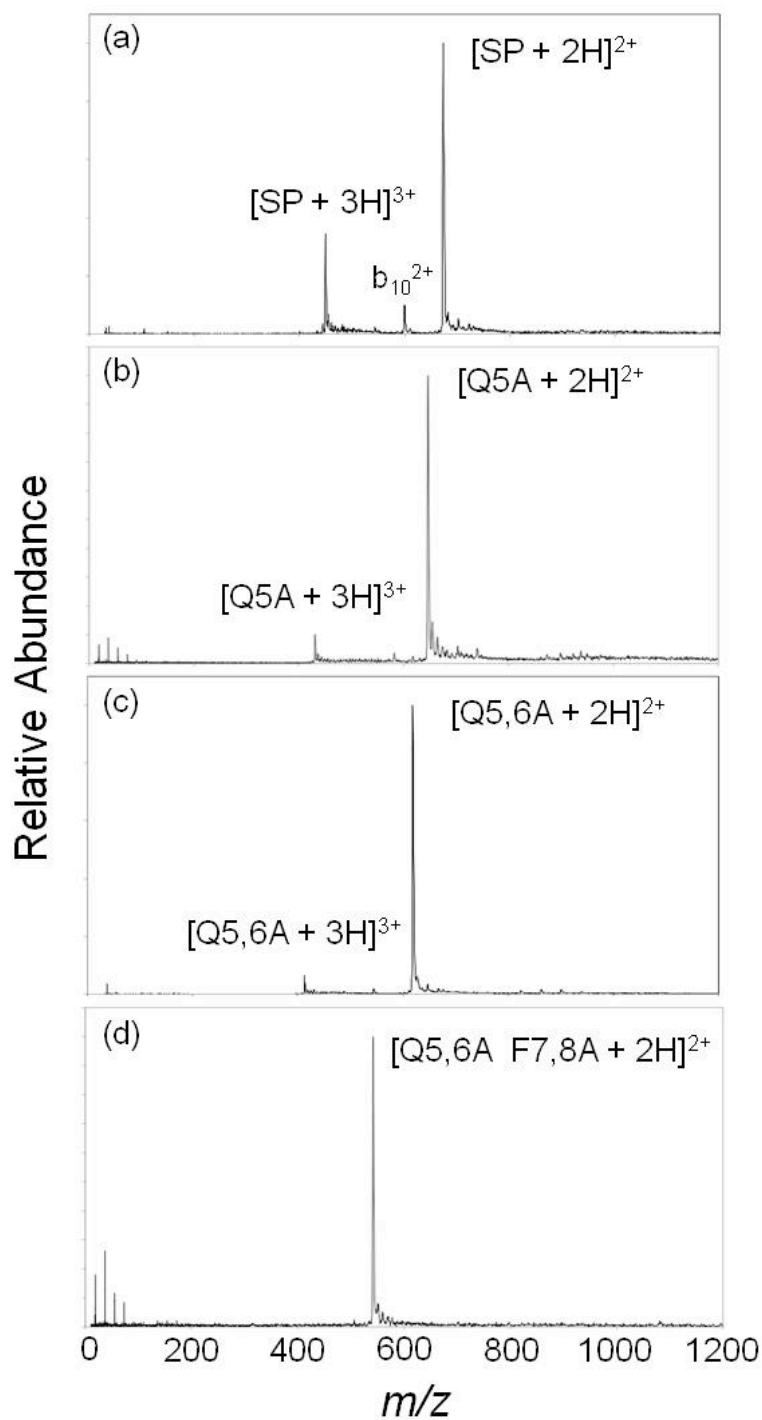
Figure 26. ESI mass spectra of substance P and mutant ions, (a) SP, (b) Q5A, (c) Q5,6A, and (d) Q5,6A F7,8A collected at a heated capillary temperature of 366 K. Stepwise mutation of the glutamine and phenylalanine residues in positions five through eight results in the observed reduced abundance of the $[SP_M + 3H]^{3+}$ ions.

Cryo-IM-MS may provide new insight into both dehydration and the structural evolution of $[SP_M + 3H]^{3+}$ ions during the final stages of ESI. Two-dimensional plots of arrival time (ATD) versus m/z for $[SP + 3H]^{3+}(H_2O)_n$ and $[SP_M + 3H]^{3+}(H_2O)_n$ ions are contained in **Figure 27**. The 2-D plot for $[SP + 3H]^{3+}(H_2O)_n$ ions yields a uniform trendline of hydrated cluster ions that trace to the dehydrated conformer **A**; a result that was interpreted as evidence that intramolecular interactions stabilize a distribution of compact conformations. Conversely, the ATDs for hydrated $[SP_M + 3H]^{3+}$ ions are much broader than those of $[SP + 3H]^{3+}$ ions and the hydration trendlines for Q5A and Q5,6A no longer trace solely to conformer **A**, but appear to trace to both **A** and **B**. The observed broadening in the ATDs appears more pronounced for the Q5,6A mutant relative to Q5A, which is consistent with increased destabilization afforded by mutating out both glutamine residues. It should be noted, however, that for both Q5A and Q5,6A, the hydrated mutant ions in the region $[SP_M + 3H]^{3+}(H_2O)_n$ ($n = \sim30$) appear to maintain a fairly narrow ATD consistent with the presence of compact conformers. As water molecules are lost to evaporation, the compact conformer population appears to be less stable and $[SP_M + 3H]^{3+}(H_2O)_n$ ions can elongate to form a structure comparable to conformer **B** with ~12 and ~23 water molecules attached for Q5A and Q5,6A respectively. Thus, elimination of intramolecular interactions that favor kinetic trapping of conformer **A** allows the peptide to become much more dynamic during the final ($n < 30$) stages of desolvation and the IM data suggests that waters solvating the mutant ions become much more disordered compared to hydration of SP. This added flexibility of

$[SP_M + 3H]^{3+}$ ions during the late stages of ESI will undoubtedly have an effect on the conformational preferences of the solvent-free ion.
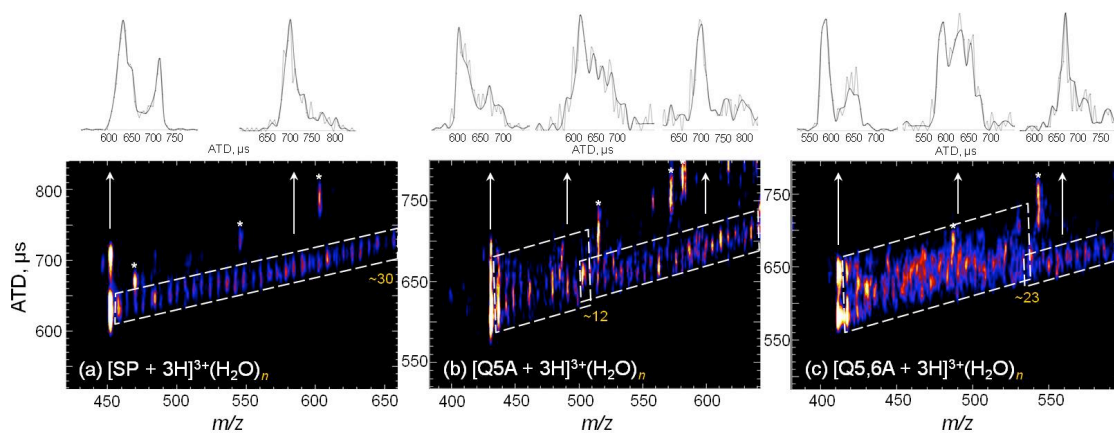
Figure 27. Two-dimensional contour plots of ATD versus m/z for $[M + 3H]^{3+}(H_2O)_n$ ions of (a) SP, (b) Q5A, and (c) Q5,6A collected at a heated capillary temperature of 356 K. Extracted ATDs from each outlined region of the hydration trendlines are shown above the plots. The first ATD shown (left) for each peptide corresponds to the $[M + 3H]^{3+}$ dehydrated ion. All other ATDs shown were extracted from the corresponding regions of the spectra, designated by arrows. The black line depicting the ATDs is the result of plotting every other data point; full data set is shown in gray. All peaks labeled with an asterisk correspond to fragment ions observed at higher capillary temperatures.

5.3.2 Evidence for Charge Reduction of Substance P Mutant Ions

For SP, it was proposed that the elongation from **A** to **B** is driven by Coulombic repulsion owing to the localization of charge sites near the N-terminus of the peptide, i.e., the N-terminus, R^1 and K^3. The close proximity of the charge sites on the $[SP + 3H]^{3+}$ ion should not be favored owing to the high degree of Coulombic repulsion. Therefore, the yields of $[SP + 3H]^{3+}$ ions appear to be directly linked to the stabilization of the charge sites provided by interactions with the glutamine and phenylalanine side chains. While these intramolecular interactions facilitate kinetic trapping of conformer

A, they also appear to be crucial to the production of $[SP + 3H]^{3+}$ ions and final charge state distribution observed. Disrupting these interactions and exposing the charge sites increases Coulombic repulsion in the peptide and can lead to a reduction in the gas-phase basicity of the charge sites.[99] At low temperatures (80 K), it appears that the preservation of solvent molecules around the charge sites coupled with the effects of Coulombic repulsion can drive a charge reduction reaction of $[SP_M + 3H]^{3+}$ ions resulting in the observed decrease in relative abundance shown in the mass spectra contained in **Figure 26**. Gas-phase ion-ion and ion-molecule reactions, including proton transfer, have previously been reported and shown to result in charge reduction of highly charged biomolecules formed by ESI.[152-157] Smith and coworkers invoked gas-phase proton transfer reactions to explain the observed change in charge state distribution of cytochrome *c* ions upon post-ESI addition of water.[158] Adding H_2O to the protein as a reactive gas after ESI into the gas phase promoted a reduction in the resultant average charge state distribution, which the authors reasoned was due to proton transfer from the multiply-charged protein ions to water molecules to form the H_3O^+ ion. The loss of a proton from a protonated amino acid to water should be unfavored owing to the fact that the proton affinity of water (~165 kcal/mol)[159,160] is much less than a basic amino acid residue (~230 kcal/mol).[99,161] However, certain factors can effectively reduce the proton affinity of amino acids in peptide or protein ions including intramolecular solvation interactions and Coulombic repulsion.[99,158] Ridge and coworkers previously showed that the apparent proton affinities of protonated basic residues in a biomolecule decreased as Coulombic repulsion increased.[99] Therefore, the removal of solvent during the ESI

process and subsequent increase in Coulombic repulsion between charge sites in a biological molecule may promote proton transfer to water molecules when they are present around the charge sites.

While this type of charge reduction reaction was previously proposed for a protein ion with a large number of charge sites and high degree of Coulombic repulsion, **Figure 28** contains cryo-IM-MS evidence for this type of reaction occurring during the electrospray process for $[SP_M + 3H]^{3+}$ ions Q5A and Q5,6A. As stated before, SP mutant ions are much more flexible or dynamic during the final stages of desolvation during ESI owing to the disruption of stabilizing intramolecular interactions. This, coupled with the prolonged exposure of the charge sites to solvent during the slow evaporative processes during cryo-IM-MS, appear to facilitate a proton transfer reaction from the peptide to a water cluster, $(H_2O)_n$, by the following mechanism:

$$[SP_M + 3H]^{3+} (H_2O)_n \longrightarrow \begin{array}{l} [SP_M + 3H]^{3+} \textit{(dehydrated ion)} \\ \\ [SP_M + 2H]^{2+} (H_2O)_{n-x} + H^+(H_2O)_x \end{array} \qquad (6)$$
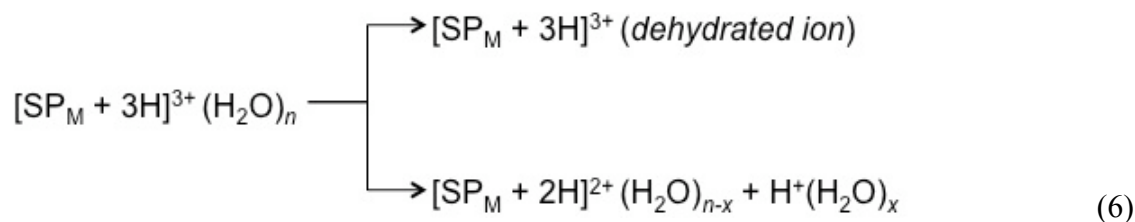
Cryo-IM-MS results clearly show that $[SP_M + 3H]^{3+}(H_2O)_n$ ions can proceed via two pathways: (1) stepwise dehydration to form the dehydrated triply-charged ion and/or (2) a proton on the $[SP_M + 3H]^{3+}$ ion can be transferred to water to form a $H^+(H_2O)_n$ cluster ion prior to complete desolvation. Evidence for charge reduction is shown in the 2-D mobility plots of ATD versus m/z for SP, Q5A, and Q5,6A shown in **Figure 28**. The ATD of an ion that entered the ion mobility drift tube as a $[M + 3H]^{3+}$ ion and was charge reduced during IMS to form a $[M + 2H]^{2+}$ ion would possess an arrival time

which falls along the $[M + 3H]^{3+}$ trendline but have a *m/z* corresponding to a $[M + 2H]^{2+}$ ion. Therefore, the enhanced signal falling below and tracing upwards to the $[M + 2H]^{2+}$ trendline corresponds to products of charge reduction. As shown in **Figure 28**, the extent of charge reduction is much more pronounced for Q5,6A compared to that for Q5A, owing to the enhanced destabilization of conformer **A** for the mutant ion upon mutation of both glutamines. These results suggest that $[SP_M + 3H]^{3+}$ ions are being lost to charge reduction via a proton transfer reaction to water, resulting in the observed decrease in relative abundance of these ions with respect to $[SP + 3H]^{3+}$ in the mass spectra shown in **Figure 26**.
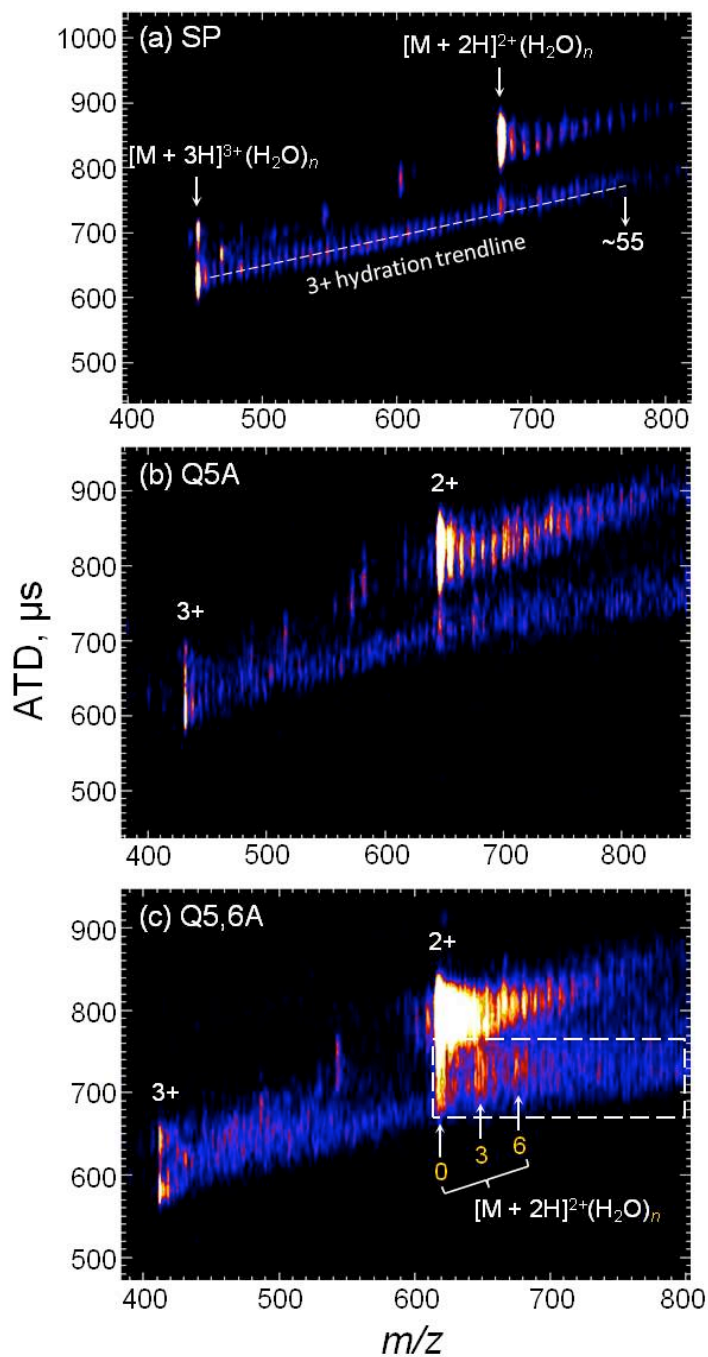
Figure 28. Two-dimensional contour plots of ATD versus *m/z* for $[M + 3H]^{3+}(H_2O)_n$ and $[M + 2H]^{2+}(H_2O)_n$ ions of (a) SP, (b) Q5A, and (c) Q5,6A collected at a heated capillary temperature of 356 K. The trendline produced for $[SP + 3H]^{3+}(H_2O)_n$ clusters is shown with a dashed line to guide the eye. Products of charge reduction are highlighted in the dashed box. The most prominent products of charge reduction for Q5,6A are highlighted and correspond to $[Q5,6A + 2H]^{2+}(H_2O)_n$ ($n = 0$, 3, and 6).

Further evidence supporting this mechanism of charge reduction is revealed in the mass spectra of Q5,6A and Q5,6A F7,8A mutants collected at various capillary temperatures (**Figure 29**). The proposed proton transfer reaction to form protonated water clusters (**Scheme 6**) should give rise to abundant signals for $H^+(H_2O)_n$ ions in the mass spectra of the mutant ions. For both mutants shown in **Figure 29**, the signal for $[SP_M + 2H]^{2+}$ ions is in 100% relative abundance and the abundances of $[SP_M + 3H]^{3+}$ ions are markedly diminished relative to $[SP + 3H]^{3+}$ ions. Protonated water clusters, $H^+(H_2O)_n$, can be seen in the low mass region of the spectra for each mutant peptide and decreasing the ion inlet temperature from 366 K to 351 K facilitates the preservation of larger clusters as expected. The increased abundance of $H^+(H_2O)_n$ clusters in the spectra for Q5,6A F7,8A compared to those for Q5,6A is further evidence for destabilization of $[SP_M + 3H]^{3+}$ ions upon mutation of the phenylalanine residues in addition to the glutamines. Collectively, these data support the hypothesis that elimination of intramolecular interactions that facilitate kinetic trapping of conformer **A** for SP negatively impacts the yield of $[SP_M + 3H]^{3+}$ ions formed by ESI. Thus charge solvation by polar side chains negates the effects of Coulombic repulsion and serves to stabilize the highly localized charge sites on SP, and elimination of these interactions facilitates the loss of $[SP_M + 3H]^{3+}$ ions to charge reduction during the final stages of desolvation.
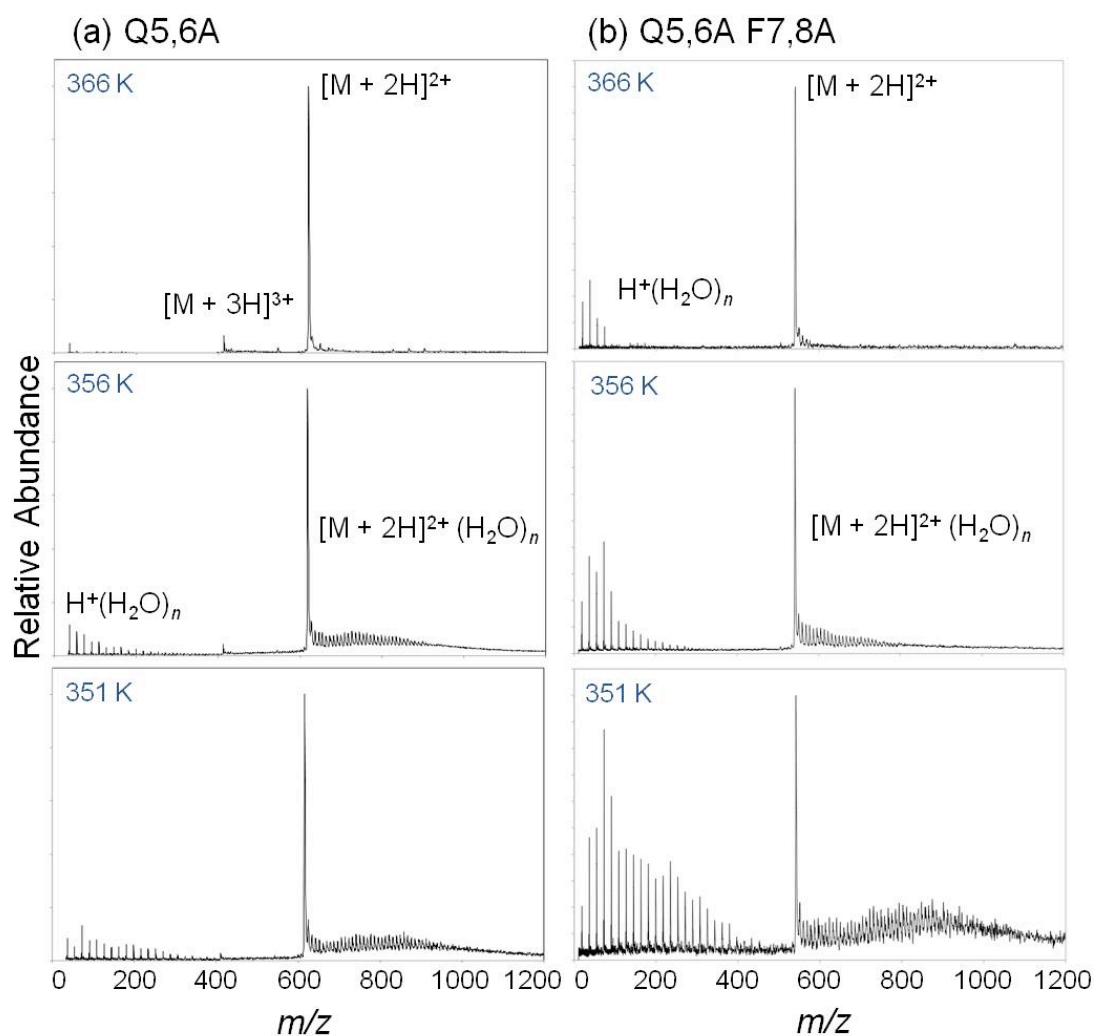
Figure 29. ESI mass spectra of SP mutant ions (a) Q5,6A and (b) Q5,6A F7,8A captured at various extents of hydration. Protonated water clusters, $H^+(H_2O)_n$, can be seen growing in the low mass region of the spectra upon reduction of the ion inlet temperature from 366 K to 351 K.

5.4 Conclusions

It was previously shown that the kinetically-trapped conformer population **A** of $[SP + 3H]^{3+}$ ions is stabilized via intramolecular interactions and upon collisional activation these interactions are disrupted leading to elongation to form the preferred

gas-phase conformation **B**. The destabilization of the intramolecular interactions via amino acid mutations results in a decrease in the relative abundance of $[SP_M + 3H]^{3+}$ ions relative to SP at cold temperatures (80 K). While the structure of $[SP + 3H]^{3+}$ ions remains fairly constant during the evaporative process owing to a uniform trendline of hydrated clusters tracing to conformer **A**, cryo-IM-MS data reveals a deviation from this uniform hydration trendline for mutants Q5A and Q5,6A reflecting the dynamic nature of these hydrated mutant ions as compared to SP. When the main intramolecular interactions of SP are disrupted by mutation of the glutamine residues, conformer **A** is stabilized by weaker interactions and is therefore more easily converted to conformer **B** upon activation. Thus the conversion from conformer **A** to **B** for mutant ions appears to occur before complete dehydration, unlike what was previously reported for SP.

The decreased stability of SP mutant ions results in the observed loss of $[SP_M + 3H]^{3+}$ ions to charge reduction at cold temperatures. Hydration data of mutants Q5A, Q5,6A, and Q5,6A F7,8A reveal that $[SP_M + 3H]^{3+}$ ions are lost during the ESI process to charge reduction that is occurring via proton transfer from the peptide to a water cluster. The reduction in the rate of droplet evaporation afforded by cryo-IM-MS coupled with Coulombic repulsion of highly localized charge sites promotes this reaction. A similar proton transfer reaction has been previously proposed for highly charged protein ions, but it is experimentally observed for small peptide ions owing to the cold conditions of cryo-IM-MS. The collective results suggest that the structural stability of SP during the evaporative processes of ESI is highly dependent on the stabilizing interactions compacting the kinetically-trapped conformer population **A**, and

disruption of these interactions can lead to a proton transfer reaction within the droplet which, in some cases, prevents formation of the $[M + 3H]^{3+}$ ion completely.

6. WATER-MEDIATED DIMERIZATION OF UBIQUITIN IONS CAPTURED BY CRYOGENIC ION MOBILITY-MASS SPECTROMETRY[*]

6.1 Background

Water plays two important roles in determining protein structure, stability, dynamics, and function by (i) inducing the hydrophobic effect, which is reasonably well understood, and (ii) mediating hydrophilic intra- and intermolecular interactions that are important not only in structural determination, but also in self-assembly and aggregation. Therefore, both long- and short-range interactions between water and biological molecules have been extensively studied both by experiment and theory.[162-167] Early studies of protein-water interactions treated water as simply an inert environment, but recently, both experimental and theoretical approaches have provided new understanding into the dynamic and active role water plays in many biological systems.[166,168] However, a detailed understanding of the effects of water on protein structures, stabilities, dynamics, and functions is largely limited to the effects of bulk solvent and specific cases where a limited number of localized water molecules strongly interact with the protein backbone and/or specific amino acid side chains.[169-173] The ability to experimentally probe the effects of solvation on peptide or protein structure will provide a better understanding of the role water plays in biological structure and functionality.

In a series of recent papers we have exploited the evaporative cooling inherent to electrospray ionization (ESI) and the low operating temperature of cryogenic ion mobility-mass spectrometry (cryo-IM-MS) as a means of directly determining changes in the conformational preferences of biomolecules as a function of the numbers of attached water molecules.[26,78,79,103,131] The cold drift cell (80 K) facilitates the preservation of hydrated gas-phase ions formed by ESI for structural analysis, providing a means to directly capture the evaporative dynamics of biological molecules as they transition from solution to the gas phase. For example, cryo-IM-MS studies of protonated water clusters revealed distinct changes in the size/shape of ions as the H-bond network of waters develops from small chain-like structures into 2D-net and stable clathrate cage structures (Chapter 2).[26,79] Similarly, the structure(s) of alkyl diammonium cations were shown to depend on the numbers of hydrating waters, as ions undergo distinct unfolding transitions during desolvation at a critical cluster size, revealing the effects Coulombic repulsion can have on ion solvation (Chapter 3).[131] For larger peptide ions, cryo-IM-MS affords the ability to relate gas-phase conformations to their solution-phase counterparts and in certain cases, kinetically-trapped species stabilized by specific intramolecular interactions can be preserved for analysis (Chapters 4 and 5).[78,102,103] Here, we use cryo-IM-MS to investigate the effects of hydration on ubiquitin ions formed under "native" electrospray (ESI) conditions.[174] On the basis of prior work on lysine- and arginine-containing peptide ions, we expect cold ubiquitin ions to be hydrated by large numbers of water molecules. Previous gas-phase studies on the hydration of small peptides showed that the number of charged functional groups

correlated well with the number of water adducts observed,[26,104] but as the size of the ion increases so do the number of hydrophilic sites present, increasing the capacity for hydration. The results presented herein are somewhat surprising in that we observe relatively few water molecules adducted to ubiquitin $[M + 7H]^{7+}$ monomer ions, but instead, we observe abundant solvated dimer ions of the type $[2M + 14H]^{14+}$. Additionally, dimer ions appear to undergo near-complete desolvation before dissociating into monomers, indicating the successful capture of a water-mediated binding event responsible for dictating the conformational preferences of ubiquitin ions.

Ubiquitin is a 76 amino acid regulatory protein that is conserved in all eukaryotic cells in all species. Its function varies and is determined by a process called ubiquitination, in which the protein covalently attaches to a target protein, tagging it for a specific cellular process dependent on both the protein and the binding site.[175,176] In aqueous solution, ubiquitin occupies low charge states in the native (N-state) conformation, which has been characterized by NMR and X-ray crystallography as a compact, folded structure made up of α–helix and β–sheet structural elements.[177,178] The N-state is stable over a large pH range, from 1.2 to 8.4;[179] however, in acidic solutions (pH ~2) containing high concentrations (~60%) of methanol, ubiquitin unfolds to form the A-state conformation, which has substantially more α-helical character and is believed to have a more elongated conformation.[180,181] Due to the known stability of the N-state conformer, ubiquitin has been the focus of many recent studies aimed at determining the extent to which native protein structure can be retained in the gas phase.[100,101,179,182-184]

6.2 Experimental Methods

The homebuilt cryo-IM-MS instrumentation has been described in detail in Chapter 1.[26,78,79] Briefly, hydrated ions are generated via electrospray ionization and guided into the variable temperature ion mobility drift tube, which is cooled to 80 K via liquid nitrogen cooling. Once inside the drift tube, ions are separated on the basis of size/shape and detected using an orthogonal time-of-flight mass spectrometer. The extent of hydration observed for ions is controlled by the temperature of the heated capillary ion inlet. Ubiquitin (bovine erythrocytes, >90% purity) was purchased from Sigma-Aldrich, diluted in deionized water (18 MΩ), and stored at -20 ºC before specific solutions were prepared. All solutions were prepared at 10 μM in pure water containing 0.1% formic acid, unless otherwise noted.

6.3 Results and Discussion

Figure 30 shows two-dimensional plots of arrival time distribution (ATD) versus *m/z* for ubiquitin ions collected at two different heated capillary temperatures. Spraying from native state conditions (pure water containing 0.1% formic acid) produces primarily $[M + 7H]^{7+}$ ions of ubiquitin (*m/z* 1224), as shown by the mass spectrum in **Figure 30(b)**, and conformations of these ions have been previously attributed to stable, compact structures.[101,179,182] However, the plots shown in **Figure 30** reveal two distinct conformer populations for $[M + 7H]^{7+}$ ions of ubiquitin, one that originates from a trendline of hydrated ions and a second observed at significantly longer arrival time with no associated hydrated ions. Upon initial observation, one might propose that the two [M

+ 7H]$^{7+}$ conformer distributions correspond to a compact state formed by evaporation of hydrated ions and a fully elongated state formed by either heat-induced unfolding[179] or by a different mechanism of ESI.[32] However, production of an unfolded state of ubiquitin [M + 7H]$^{7+}$ ions under cold instrument conditions is unlikely considering the broad stability of the tightly folded N-state conformer that has been observed over a wide range of experimental conditions.[101] Even under denaturing conditions, [M + 7H]$^{7+}$ ions of ubiquitin have been shown to adopt mainly compact, N-state, structures that resist unfolding upon collisional activation of >100 V.[179] To rule out the possibility of an elongated conformer being formed by an alternative mechanism during the desolvation process, heating studies were performed and are discussed below. Collectively, the experimental data presented herein clearly show that ions falling along the hydrated trendline in **Figure 30(a)** correspond to a noncovalent dimer of the type [2M + 14H]$^{14+}$(H$_2$O)$_n$ ($n = 1$ to ~285). The fact that these ions retain a high degree of hydration, whereas relatively few numbers of water molecules are adducted onto the [M + 7H]$^{7+}$ monomer ions suggests that the dimer is stabilized in some way by the presence of water. Data shown in **Figure 30(b)**, collected at an increased heated capillary temperature, provide additional evidence that [2M + 14H]$^{14+}$ dimer ions undergo near-complete desolvation upon heating before dissociating to form monomer ions. Increasing the heated capillary temperature from 363 K to 378 K promotes evaporation of the hydrating waters tracing to the bare [2M + 14H]$^{14+}$ dimer ion. While the dimer appears to retain stability with relatively few numbers of water molecules attached, the streaking, i.e., low abundance signals, observed in the 2-D plot (**Figure 30(b)**) between the bare

dimer and monomer populations suggests that upon heating, dimer ions dissociate within the IM drift cell to form $[M + 7H]^{7+}$ monomer ions.
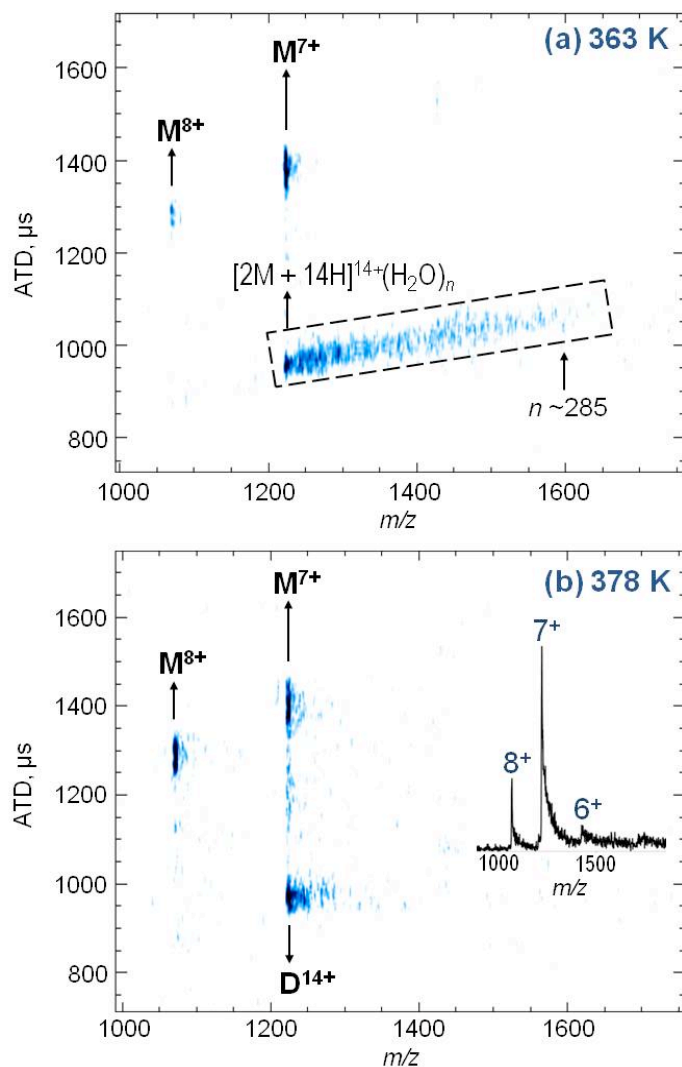
Figure 30. Two-dimensional contour plots of ATD versus *m/z* for ubiquitin ions collected at a heated capillary ion inlet temperature of (a) 363 K and (b) 378 K. Solutions of ubiquitin were prepared at a concentration of 10 μM in pure water containing 0.1% formic acid. A representative mass spectrum is shown as an inset in panel (b) reflecting the typical charge state distribution produced from native state ESI conditions. Assignments of monomer and dimer ions are labeled in the spectra. Under cool inlet conditions, a trendline of hydrated ions is detected tracing to the $[2M + 14H]^{14+}$ dimer.

Further evidence supporting the conformer assignment of hydrated, noncovalently bound dimer ions is derived from data taken at different solution concentrations of ubiquitin. Assuming the population falling at shorter arrival time in the mass-selected ATDs (**Figure 31(A)**) corresponds to the $[2M + 14H]^{14+}$ dimer, increasing the sample concentration should result in an observed increase in the abundance of dimer ions relative to the monomer ion population. **Figure 31(A)** shows that increasing the concentration of ubiquitin from 10 μM to 25 μM and 50 μM resulted in an increase in the relative abundance of the dehydrated dimer population from 11% to 44% and 63%, respectively. The most plausible explanation for this dramatic increase is the attribution of the population to dimers, which are known to increase in solution with increasing concentration. Note that these plots do not represent the total ion abundances of the dimer population due to the fact that the extracted ATDs show signal for dehydrated ions only, and do not account for hydrated ions present in the spectrum. Additional data for 75 μM samples acquired at even higher capillary temperature (366 K) provide further support for the peak assignment (**Figure 32**). Finally, we note the shape of the longer ATD peak for the +7 charge state is consistent with what is expected for monomer ions. The peak shape for the higher mobility ions, observed at ~1000 μs, is much narrower than expectations for the $[M + 7H]^{7+}$ monomer ions, even under cold conditions; the sharpening of the peak is consistent with an increase in the effective drift force associated with the more highly charged $[2M + 14H]^{14+}$ species.
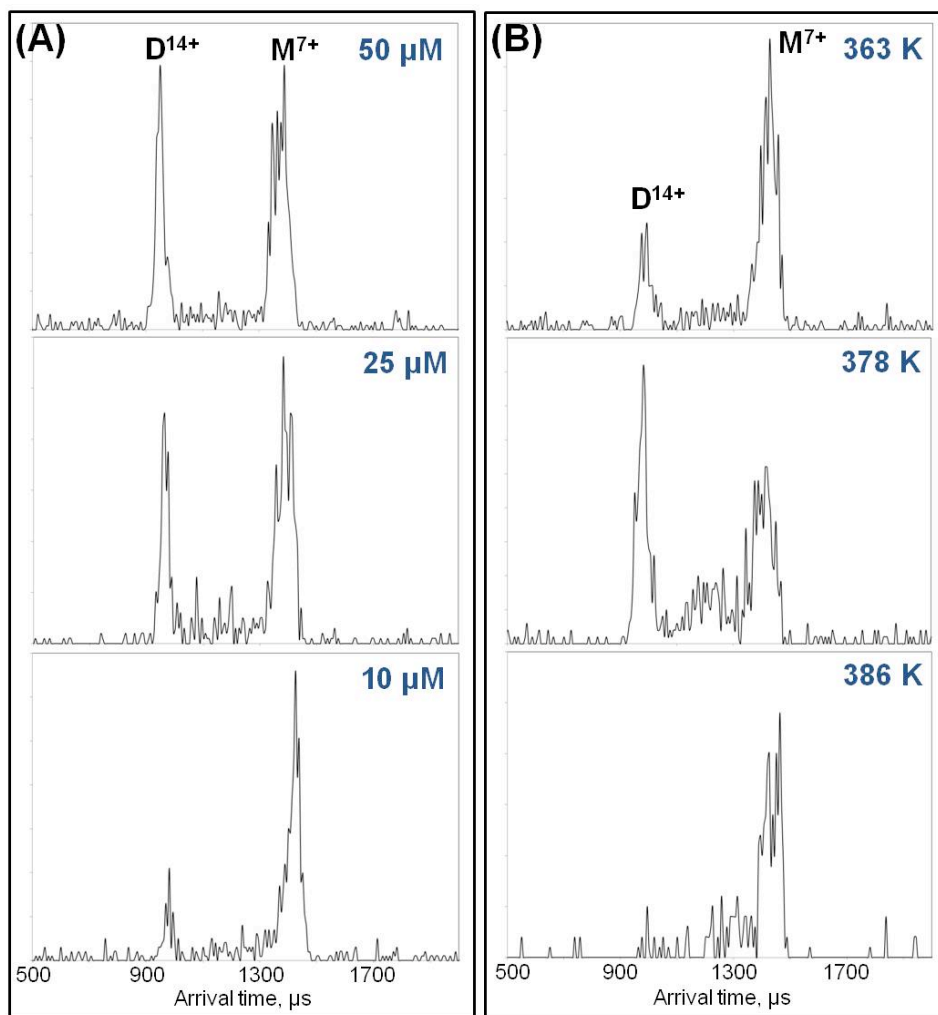
Figure 31. (A) Mass-selected arrival time distributions (ATD) of the +7 charge state of ubiquitin (*m/z* 1224) obtained by electrospraying 50 μM, 25 μM, and 10 μM solutions from pure water with 0.1% formic acid. All spectra were collected at a heated capillary temperature of 356 K. (B) Mass-selected ATDs of the +7 charge state of ubiquitin collected at heated capillary temperatures ranging from 363 K to 386 K. Identical solution conditions were maintained for all spectra shown (10 μM from pure water with 0.1% formic acid).

94
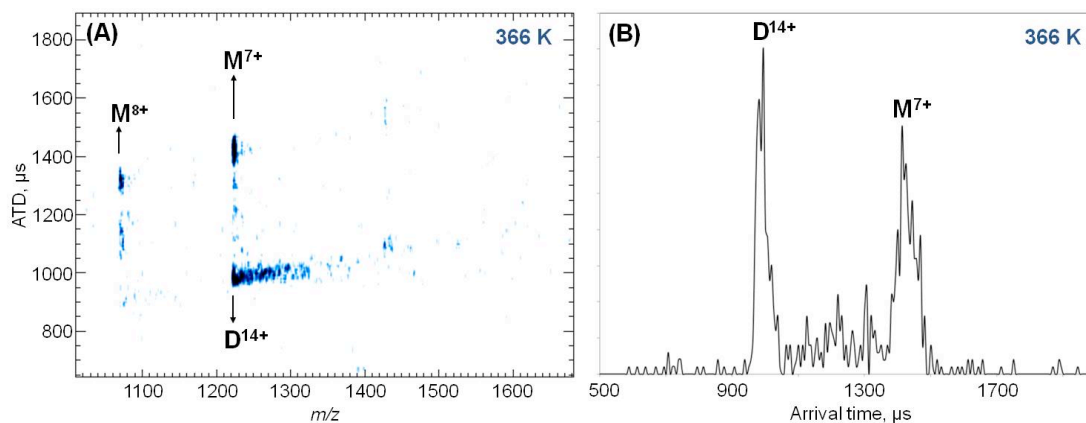
Figure 32. (A) 2-D contour plot of ATD versus *m/z* for ubiquitin ions collected at a concentration of 75 μM. (B) Mass-selected ATD of the +7 charge state extracted from the data shown in (A). Solution conditions are the same as those shown in Figure 31 (pure water with 0.1% formic acid). Increasing the concentration to 75 μM results in the observed increase in abundance of the dimer ion population relative to that of the monomer, consistent with our assignment of peaks.

Heating studies were also performed by varying the temperature of the heated capillary ion inlet, as shown in **Figure 31(B)**, in order to elucidate the role water plays in stabilizing the interactions at the binding interface. Upon heating, the dimer first loses virtually all of its hydrating water, as evidenced by the truncation of the hydration trendline in **Figure 31(B)**, before dissociating to form monomer ions, as evidenced by the streaking observed between the dehydrated dimer and monomer populations (across the mobility axis). It appears from the mass-selected ATDs shown in **Figure 31(B)** that the relative abundance of the dimer population increases initially upon heating before dissociating completely to form monomer ions. This can be explained by the desolvation pathway undergone by ubiquitin ions during ESI. After minimal heating, hydrated dimer ions undergo stepwise desolvation to lose the weakly bound H-bond network of water molecules solvating and stabilizing the ion. Since it is likely that less energy will be

95

required to drive off these hydrating waters than the amount required to induce dissociation, upon initial heating, the dehydrated state of the dimer will appear to increase in abundance relative to the monomer, as observed in the mass-selected ATDs shown in **Figure 31(B)**. Upon additional heating, the dehydrated dimer ions begin to dissociate in the drift cell forming monomers, as indicated by the streaking observed between the two conformer distributions as the ion inlet temperature is increased. Eventually, the $[2M + 14H]^{14+}$ dimer population disappears completely leaving a single conformer distribution for $[M + 7H]^{7+}$ ions that we attribute to the stable, compact N-state monomer. Increasing the effective ion temperature of the dimer to induce dissociation during the IM measurement can also be achieved by operating at high field strengths in the drift tube (**Figure 33**). Additional evidence supporting the peak assignments of dimer and monomer ions, including the observation of an asymmetric dimer ion at high concentrations, is included in **Figure 34**.
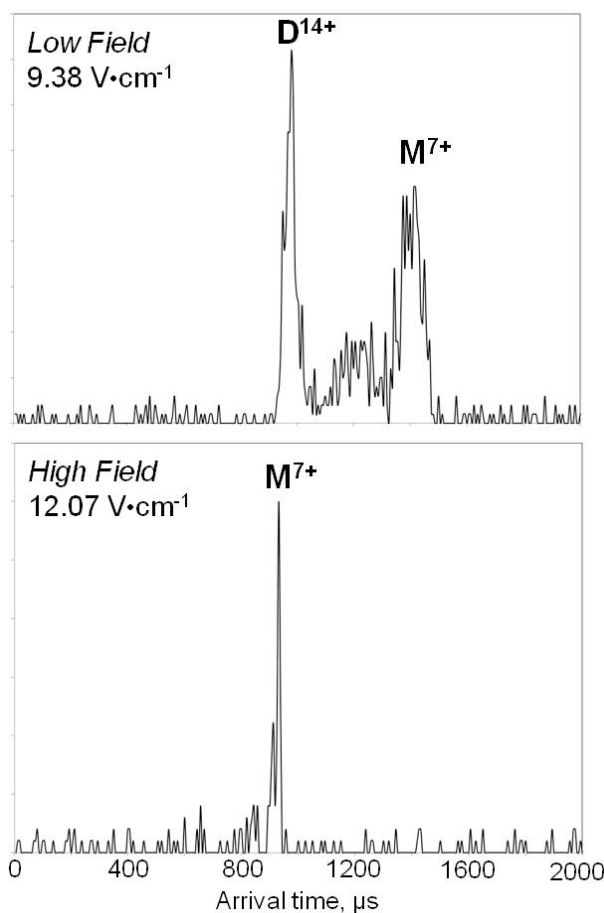
Figure 33. Mass-selected ATDs of the +7 charge state of ubiquitin ions collected under low field strength conditions across the drift tube (9.38 V•cm^{-1}) compared to high field (12.07 V•cm^{-1}). The "low-field limit" for the cryo-IM-MS instrument was previously established and it was shown that at higher fields (>10.4 V•cm^{-1}), collision induced dissociation resulted in the dissociation of weakly bound species during the IM measurement.[4] The data shown here is consistent with this finding, as the ATD of the monomer ion expectedly shifts to shorter drift time with increased field strength and the peak assigned to the dimer ion disappears completely. By increasing the field strength across the drift tube, the effective ion temperature of the dimer is increased and CID of the weakly bound species results in dissociation of the ion.
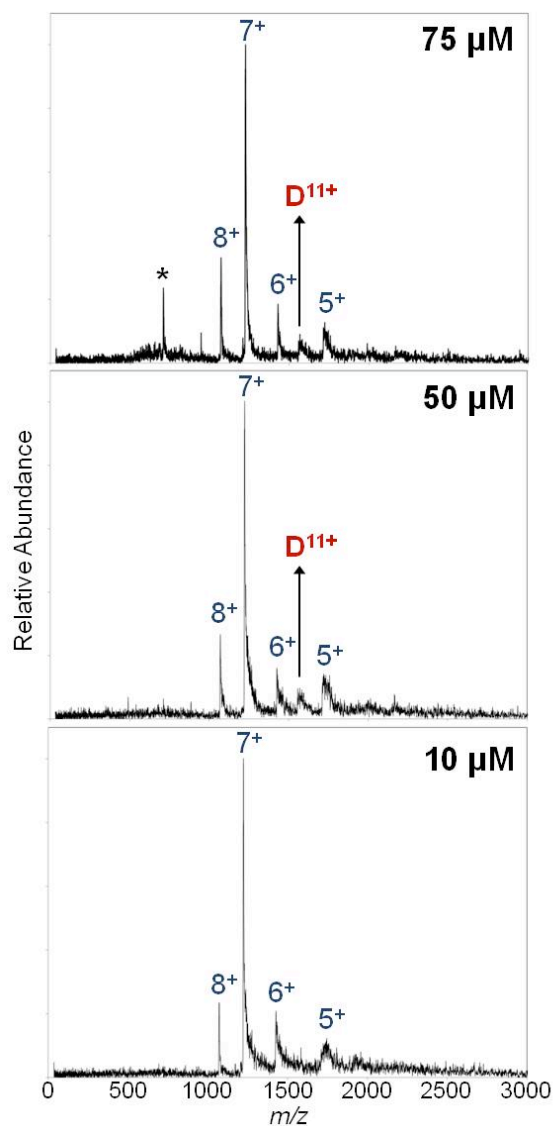
Figure 34. Mass spectra of ubiquitin ions collected at concentrations of 10 μM, 50 μM, and 75 μM. All solutions were prepared in pure water with 0.1% formic acid to produce the "native" charge state distribution for ubiquitin, centered on the $[M + 7H]^{7+}$ ion. The spectra clearly show the presence of an asymmetric dimer, $[2M + 11H]^{11+}$, in low abundance at increased concentrations (50 μM and 75 μM). The formation of asymmetric dimers is not unexpected at high concentrations and supports the notion that noncovalently bound dimers of ubiquitin are being preserved in the experiment. The peak labeled with an asterisk is an unidentified contaminant ion.

Collectively, the cryo-IM-MS results indicate that the presence of water mediates a protein-protein binding event resulting in formation of hydrated dimer ions that remain stable until near-complete desolvation. Because the dimer ions retain stability throughout the desolvation process, this suggests that while water may drive association, it is not essential to the preservation of the noncovalently bound species. Therefore, additional interactions must serve to stabilize the binding interface in the absence of water. Evidence for such interactions was recently reported by Liu *et al.* in which NMR data showed that free ubiquitin dimerizes noncovalently in solution at high concentrations and upon doing so, forms a hydrophobic interface between portions of the β-sheet regions of two ubiquitin molecules.[185] While such an interface may be weakly interacting in the absence of water, buried hydrophobic surfaces have been shown to contribute significantly to the stability of protein-protein interfaces. Brunori *et al.* estimated the free energy gain associated with burying hydrophobic residues on the surface of a protein through protein-protein binding to be ~15 cal/mol per square angstrom of surface area buried.[186] Simulated annealing calculations performed by Liu *et al.* suggest that noncovalent dimerization of ubiquitin buries an area of ~600 Å on average.[185] Therefore, formation of noncovalent dimers of ubiquitin may be favored in solution, where the hydrophobic effect drives the binding of two interfaces, and then the noncovalently bound species is able to survive transfer to the gas phase under gentle instrument conditions.

Further evidence supporting the formation of a hydrophobic interface between ubiquitin ions comes from recent studies revealing the hydrophobic region of the native-

state structure of ubiquitin to be the most common interaction site in ubiquitination events.[176] While it is reasonable to presume that the presence of water would facilitate the binding of these regions, when water mediates this interaction during desolvation, it is likely that "hot spots" form within the interface.[163] Such regions have been shown to contribute significantly to the stability of the bound species, in part, by occluding water from the hydrophobic interface. In the case of ubiquitin, the side chains of Leu-8, Ile-44, and Val-70 have been shown to form a hydrophobic patch in the β-sheet region of the protein that participates strongly in protein-binding events.[171,185,187] Wand and coworkers have shown that the water molecules solvating these hydrophobic sites exhibit restricted hydration dynamics, similar to what is expected for protein binding sites.[171] Additionally, reports by Liu *et al.* on noncovalent dimerization of ubiquitin in solution pointed to residues surrounding Leu-8, Ile-44, and Val-70 as the primary sites of binding within the hydrophobic interface.[185] Therefore, we propose that the hydrated ubiquitin dimer observed here results from the water-mediated binding of two hydrophobic interfaces encompassing the β-sheet region of the protein, specifically the "hot spots" formed from the side chains of Leu-8, Ile-44, and Val-70.

Ubiquitin contains twelve basic residues, most of which are likely protonated in acidic solutions and located near the surface of the native state structure, isolated from the hydrophobic region of the molecule (see **Figure 35**).[172,185] Interestingly, a number of these hydrophilic sites are located in close proximity to the β-sheet region of the molecule, surrounding the hydrophobic core. These hydrophilic sites are expected to be solvated and may serve as initiators of dimer formation. Recent studies of diammonium

cations have shown experimental evidence for the structural implications of forming stable water bridges between ammonium ions where the stability provided by solvation offsets the effects of Coulombic repulsion and induced folding of the ions within a water droplet.[128,131] In addition to the energy gain associated with the buried hydrophobic surface area, water bridging between protonated lysine and/or arginine side chains of ubiquitin ions could be aiding in the stabilization of noncovalently bound dimers. Since it is likely that water would be excluded from a hydrophobic dimer interface, the most favorable hydration sites on the protein surface are assumed to be the exposed charged groups.[104] The location of many of these charged groups, at the periphery of the proposed binding interface, suggests that water molecules could potentially form a ring-like orientation around the hydrophobic interface. Similar hydration behavior has been observed for protein-protein interfaces[170] and the stabilization of these sites through the formation of "water bridges" between hydrophilic sites would assist in the facilitation of the water-mediated binding event responsible for formation of the ubiquitin dimer.
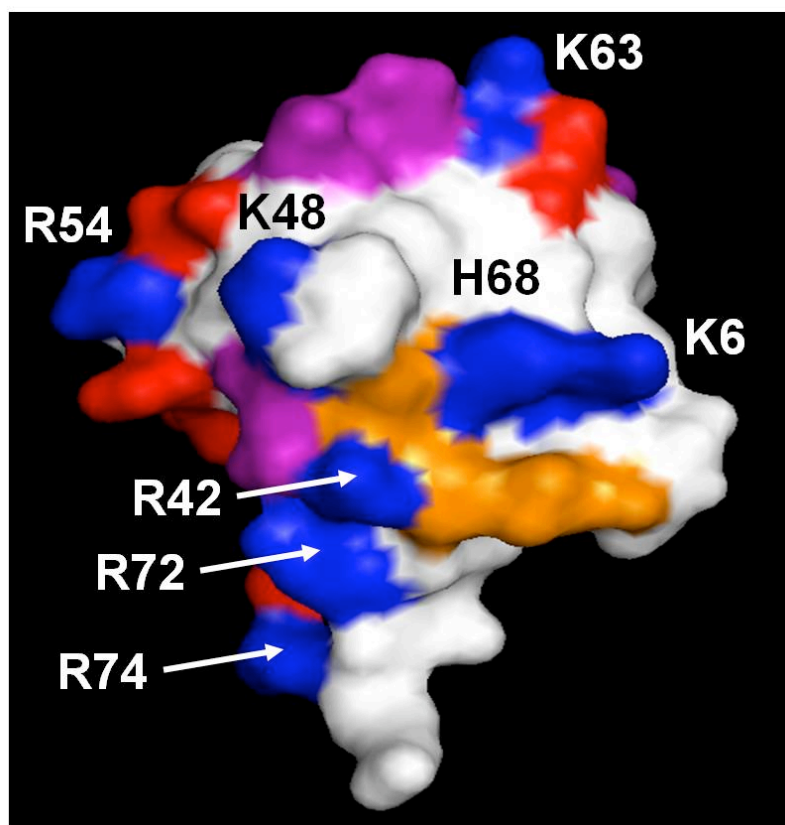
Figure 35. Structure of the N-state conformer of ubiquitin illustrating the hydrophobic region (orange) and surrounding basic residues (blue). The acidic residues (red) and glutamines (purple) are also shown. Expected sites of hydration include the protonated side chains of the exposed basic residues. The location of K6, K11 (not visible), R42, K48, H68, R72, and R74 around the hydrophobic binding region suggests that these hydrophilic sites may serve as initiators of dimer formation.

6.4 Conclusions

Probing the effects of solvation on the conformer preferences of ubiquitin under native state conditions identified a water-mediated protein-protein binding event leading to the formation of noncovalently bound dimers in solution. Interestingly, the absence of extensively hydrated N-state $[M + 7H]^{7+}$ ions suggests that monomeric ubiquitin ions are formed by dehydration of the dimer and subsequent dissociation. This observation is not

totally unexpected considering the recent report by Liu *et al.* on the formation of noncovalently bound dimers of ubiquitin in solution,[185] which, under gentle instrument conditions afforded by cryo-IM-MS, can be preserved upon transfer to the gas phase. Water plays a key role in determining structural preferences of proteins as well as structure/function relationships, and there is growing evidence indicating that the formation of protein-protein "hot spots" amidst hydrophobic binding regions is largely dependent on the initial presence and ultimate occlusion of water. Although insights about protein hydration and water-mediated processes have been gleaned from molecular dynamics simulations, there are few experimental tools for understanding the effects of water on protein structure and protein-protein interactions. Additional work including MD simulations and site-specific amino acid mutations are needed to further characterize the structure of the ubiquitin dimer ion and would potentially elucidate specific interaction points within the hydrophobic binding interface. The cryo-IM-MS approach adds a new dimension to studies of hydrated protein ions and may ultimately shed light on many water-mediated processes that dictate the structure/function of proteins.

7. FUTURE DIRECTIONS, OUTLOOK AND CONCLUSIONS

7.1 Small Ion Hydration Studies

Initial cryo-IM-MS studies of singly protonated water clusters (Chapter 2) revealed distinct structural transitions corresponding to different H-bonding motifs. It has been shown that the structures of the H-bonded networks of interconnected water molecules are highly dependent on the nature of the core ion in the cluster. Therefore, varying the core ion from a proton to other small charge carriers may induce distinct differences in the H-bond network of water molecules solvating the ion. Williams and coworkers have published a number of recent papers on the hydration of small ions (Gdm$^+$, Na$^+$, La^{3+}, K$^+$, Li$^+$, etc.) in aqueous nanodroplets studied by infrared photodissociation spectroscopy.[70,71,188,189] Results showed that certain ion cores promoted the formation of stable clathrate cage structures when solvated by specific numbers of water molecules. Understanding the formation and structure(s) of these clathrate cages will have implications on many industrial processes, owing to the fact that clathrate cage hydrates have been shown to form around small natural gas molecules such as methane.[190] These water cages are thought to have the potential to play significant roles in many industrial applications including gas storage and transportation and energy recovery.

Mass spectra from initial cryo-IM-MS studies on Na$^+$ and Gdm$^+$ (**Figure 36**) show that hydrated cluster ions of the type [M + H]$^+$(H$_2$O)$_n$ can be formed by ESI. For both ions, protonated water clusters, H$^+$(H$_2$O)$_n$, are also formed. Magic number cluster

ions are not observed for either ion, consistent with previous studies.[42,70] Two-dimensional mobility plots would likely deconvolute the two trendlines of cluster ions, revealing any structural transitions associated with each. Therefore, extension of these studies to include mobility data would elucidate any structural changes occurring as a function of cluster size for the hydrated ions. Determining the structures of a number of small cluster ions would expand our understanding of the factors that influence specific versus nonspecific hydration preferences. This would potentially have implications in understanding the hydration behavior of many peptides and proteins, as biomolecular ions containing lysine (ammonium ion) or arginine (guanidinium ion) have been shown to exhibit specific or nonspecific solvation around the charged group, respectively.
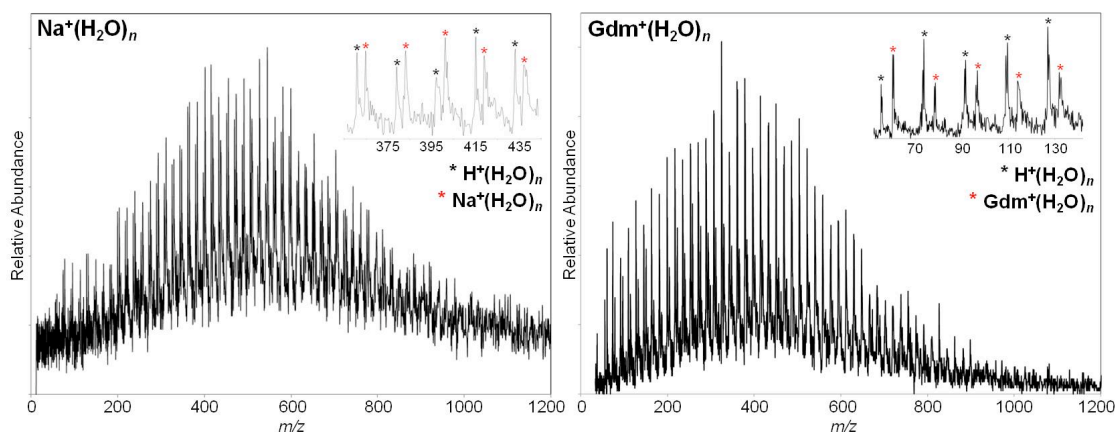
Figure 36. Mass spectra of $Na^+(H_2O)_n$ and $Gdm^+(H_2O)_n$ ions collected at a heated capillary temperature of 343 K. Protonated water clusters, $H^+(H_2O)_n$, are also present in both spectra; peaks labeled in the insets with blue asterisks correspond to $H^+(H_2O)_n$ ions. The inset on the left spectrum contains $Na^+(H_2O)_n$ (n = 19 to 23) and $H^+(H_2O)_n$ (n = 20 to 24) ions. The inset on the right spectrum contains $Gdm^+(H_2O)_n$ (n = 0 to 4) and $H^+(H_2O)_n$ (n = 3 to 7) ions.

In addition, expanding the number of small ions studied via cryo-IM-MS to include other Hofmeister cations would also lead to an increased understanding of the structure and dynamics of biological molecules in aqueous environments. The Hofmeister series is a classification of ions based on their observed effects on protein stability in aqueous environments, specifically their ability to either "salt-in" or "salt-out" a protein ion.[191,192] While the series has been well established for some time, there is still some debate over the nature of the interactions between these ions with proteins in water. Hofmeister ions are generally believed to either organize or disrupt the local structure of water around a biomolecule, but in some cases, direct ion-protein interactions have been reported as well.[193,194] It is likely that a combination of ion-protein and ion-water interactions play a role in protein stability. Developing a better understanding of the affects of small charge carriers on the structure of water, thorough cryo-IM-MS studies, will resolve some of the lingering questions related to peptide/protein structure and stability.

7.2 Hydration Behavior of Lysine- and Arginine-Containing Peptides

Previous studies have repeatedly shown a strong dependence of the presence and nature of charge-carrying species on the structures of hydrated ions.[42,46,94] Hydration of the ammonium ion ($-NH_3^+$) versus the guanidinium ion ($-Gdm^+$) will highlight some of the key differences between specific and nonspecific hydration and the structural implications of each. In Chapter 3, these differences were briefly discussed for two peptide ions, bradykinin (BK) and gramicidin S (GS). As explained, these studies of

exclusively lysine- or arginine-containing peptide ions showed that nonspecific solvation of BK ions resulted in structural stability during desolvation whereas specific solvation of GS led to the formation of stable magic number clusters. Hydration of substance P (SP) (RPKPQQFFGLM-NH$_2$) ions, containing both lysine and arginine, did not show evidence for formation of magic number clusters, likely due to interplay between the localized charge sites during the evaporative process of ESI. It would be interesting to explore whether conformational preferences for SP would change as a result of mutating arginine for lysine (R1K) or lysine for arginine (K3R). Studies of the diammonium cations presented in Chapter 3 showed that water bridging between ammonium ions induced conformational changes, i.e., unfolding of the ion during desolvation. Therefore the presence of multiple protonated lysine residues within a larger peptide ion may induce similar structural changes.

Evidence for this can be seen in preliminary studies performed on the reverse-sequence SP (rSP) (MLGFFQQPKPR-NH$_2$) peptide ion. CCS profiles for the [M + 3H]$^{3+}$ ion of rSP are shown in **Figure 37** and compared to CCS profiles for SP. As discussed previously, the compact conformer of SP is stabilized by intramolecular interactions between the charged residues and Q^5/Q^6 or F^7/F^8. Disruption of these interactions was shown to result in elongation of the ion to form the extended conformer family. Contributing to this elongation was the increased Coulombic repulsion between the charged sites localized on the N-terminus of the ion, observed once the intramolecular interactions were disrupted. In an attempt to highlight the dependence of charge site location on the formation of the compact conformer **A**, rSP was used to

separate the charged sites to the N-terminus, K^9, and R^{11}.[102] As shown in **Figure 37**, this resulted in the formation of a single conformer family that was assigned to an extended conformer resembling conformer **B** for SP. Cryo-IM-MS data of rSP $[M + 3H]^{3+}$ ions, shown in **Figure 38**, reveals a deviation in the trendline of clusters tracing to the dehydrated conformer population. It appears that at large cluster sizes ($[M + 3H]^{3+}$ $(H_2O)_n$ ($n > 30$)), ions initially adopt a compact conformer population before elongation occurs prior to complete desolvation. This transition, although less distinct, appears to occur around ($n = 30$) and is similar to the unfolding transition observed for diammonium cations (Chapter 3). In this case, water could be bridging between the ammonium ion on the N-terminus of rSP and the ammonium ion of lysine in position 9, when the droplet size is large enough to compensate for Coulombic repulsion. This would potentially explain the distinct differences between the conformer preferences of SP and rSP during dehydration observed by cryo-IM-MS.
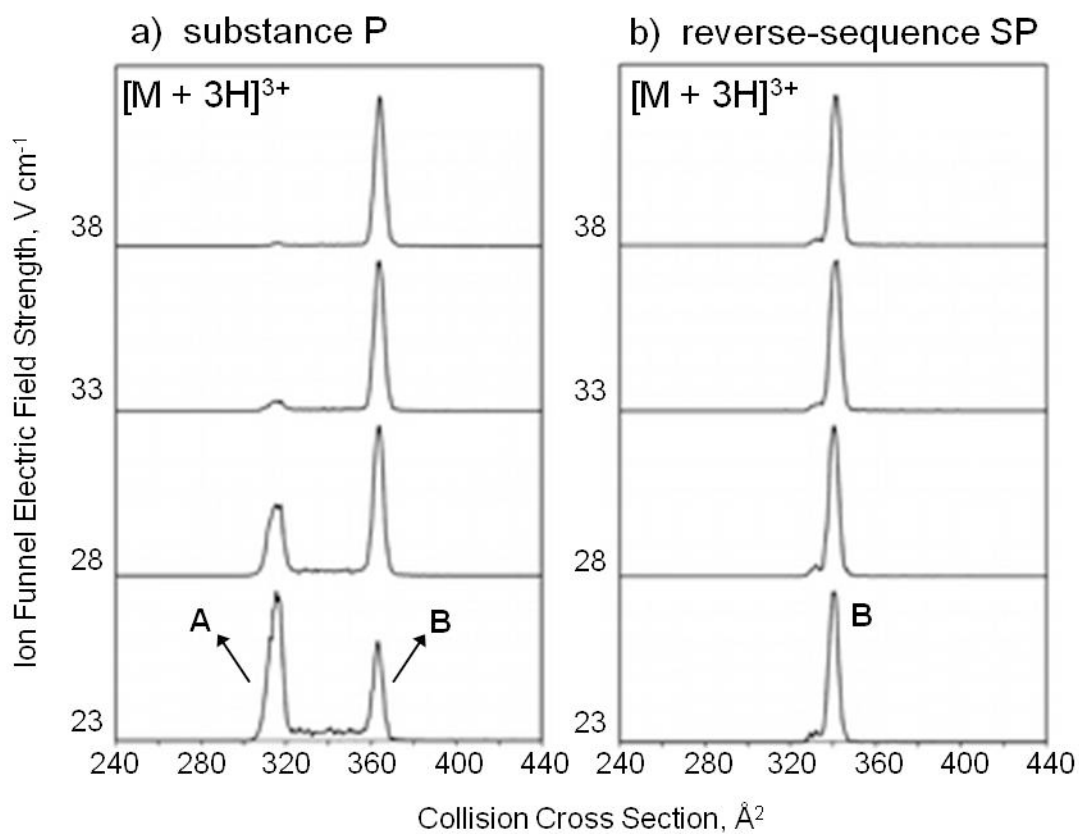
Figure 37. CCS distributions of a) SP and b) reverse-sequence SP shown as a function of electric field strength in a periodic focusing ion funnel. At the lowest electric field (23 V cm^{-1}), the kinetically-trapped conformer **A** is preserved for SP. As the field strength increases, the conformer distribution rearranges to form conformer **B**. For reverse-sequence SP, the absence of any structural changes upon heating indicates that the single conformer distribution observed corresponds to an elongated conformer **B**.
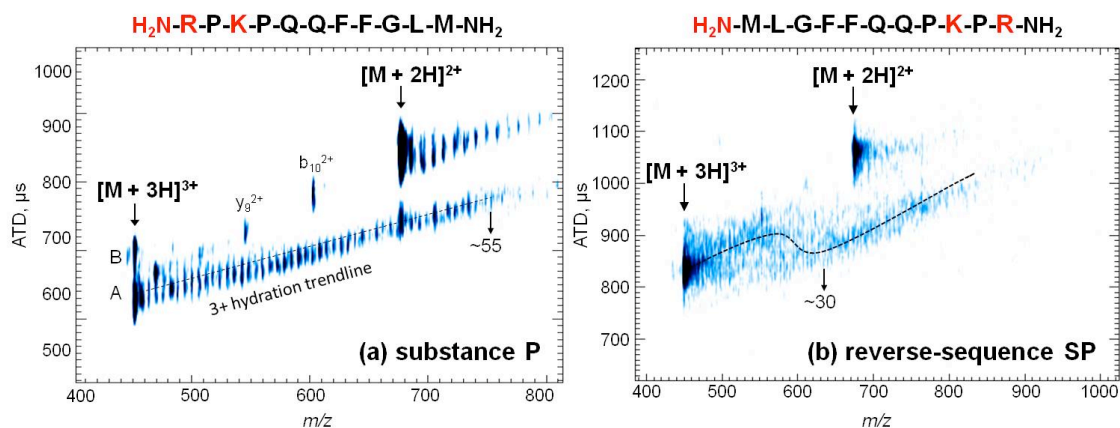
Figure 38. Two-dimensional contour plots of ATD versus *m/z* for (a) SP and (b) reverse-sequence SP collected at a heated capillary temperature of 356 K and 346 K, respectively.

Similar studies could be performed on a number of different arginine- and lysine-containing peptide ions. Bradykinin (RPPGFSPFR) provides a good model system in which a number of R-to-K mutants (R1K, R9K, and R1,9K) could be probed by cryo-IM-MS to examine the effects of hydration on the $-NH_3^+$ and $-Gdm^+$ ions even further. While water bridging between arginine residues on bradykinin either is unfavorable or does not cause any major conformational changes during desolvation, this may change when arginine is replaced by lysine. Another model peptide system available to systematically compare the hydration of $-NH_3+$ and $-Gdm^+$ is the helical peptide $E^1AAX^4AAA^7AAA^{10}$, where X = K or R. Methylation of E^1 will allow the potential effects of salt bridge formation to be examined,[195] while the presence of R versus K will potentially result in conformational differences due to both interactions with water and E^1. Additionally, peptides have been synthesized in which the unit –EAAX- is located in the middle of the peptide ($-E^4AAX^7-$) and on the C-terminus of the peptide ($-E^7AAX^{10}$).

110

This will allow the effects of charge location on conformer preferences and hydration to be examined as well. Cryo-IM-MS studies of these systems have the potential to gain valuable insights into the factors contributing to conformational diversity of peptide ions and how hydration affects these preferences.

7.3 Role of Solvent on Cis/Trans Preferences of Proline-Containing Peptides

Most amino acids typically adopt the *trans* configuration due to thermodynamic favorability, but proline is unique in the fact that it can adopt both *cis* and *trans* peptide bonds dependent on its environment.[196] As a result, polyproline peptides have been shown to exist in two helical forms in solution referred to as polyproline I (PPI) and polyproline II (PPII). The PPI helix contains all *cis* configurations and is stable in hydrophobic environments such as nonpolar solutions. Alternatively, the PPII helix contains all *trans* configurations and is favored in hydrophilic aqueous solutions. The stability of both helices results from varying effects; H-bond networks of water molecules stabilize PPII by bridging between the backbone carbonyl groups on adjacent prolines, while the stability of PPI is attributed to van der Waals forces. Therefore, solvent should play a large role in dictating the conformational preferences of polyproline resulting from varying *cis*/*trans* preferences.

Gas-phase studies of polyproline helices have shown that while ions retain memory of their solution-phase structures, *cis*/*trans* isomerization leads to the interconversion of PPI and PPII conformations and the formation of several distinct conformer families.[197] Clemmer and coworkers recently used IM-MS to study the

conformational changes induced during the transition from PPI to PPII for a 13-residue polyproline peptide (Pro13).[197-199] This conversion (PPI → PPII) was achieved by changing the solution environment from 1-propanol to water and collecting IM-MS data as a function of time. Results showed that Pro13 $[M + 2H]^{2+}$ ions transition through a series of distinct intermediate structures en route to forming the PPII all-*trans* helix. Folding is induced by the *cis-trans* isomerization of specific residues.

Cryo-IM-MS can potentially be used to further examine the role solvent plays on the *cis*/*trans* preferences of proline-containing peptide ions. Based on past studies, one would expect that spraying Pro13 from aqueous solutions would generate the all-*trans* helix that would maintain stability in water during the desolvation process of ESI. The ATD of Pro13 $[M + 2H]^{2+}$ ions (**Figure 39**) generated by cryo-IM-MS from 100% water shows that ions do not exist in a single conformational family. The ATD appears broad, consisting of at least two main conformer families, suggesting that the peptide may not adopt the all-*trans* helix exclusively. In addition, the 2-D plot of ATD versus *m/z* shows that the $[M + 2H]^{2+}$ ion of Pro13 does not form abundant hydrated cluster ions. At low capillary temperatures, (388 K) very few waters are preserved on the ion ($n < 15$) suggesting that the hydrated conformer population generated from aqueous solution may not be stable during the desolvation process. This result is somewhat surprising since the PPII helix should be favored in aqueous solutions resulting from stabilization from interactions with water molecules. Initial cryo-IM-MS results, however, do not indicate formation of a stable hydrated PPII helix from aqueous solution, suggesting that the conformer may be more hydrophobic than initially expected.

Figure 39. Two-dimensional contour plot of ATD versus *m/z* for [M + 2H]$^{2+}$ ions of Pro13 sprayed from a solution of pure water with 0.1% formic acid at a heated capillary temperature of 338 K. Pro12 [M + 2H]$^{2+}$ ions are also present in low abundance. The inset contains the mass-selected ATD for Pro 13 [M + 2H]$^{2+}$ ions.

In an attempt to increase the capacity for hydration of the Pro13 peptide, mutant ions were formed in which basic residues were added to the N-terminus of the peptide. Specific peptides generated were HisPro13 and LysPro13, in which a histidine and lysine were added to the N-terminus of the 13-residue polyproline, respectively. Initial cryo-IM-MS studies (**Figure 40 and 41**) show that addition of a basic residue, in both cases, does not appear to alter the hydration behavior of the peptides significantly from that of Pro13. Again, this result is somewhat surprising considering that protonated lysine or histidine should hydrate by a large number of water molecules, considering that

the number of charged functional groups has been shown previously to correlate well with the total number of water adducts observed. In this case, the hydrophobicity of the polyproline chain may be inhibiting the basic residue from hydrating. Mutating the peptides even further to introduce a hydrophilic region may stabilize the peptide in the presence of water. Additional experiments invoking different solvent environments may also shed light on the effects of *cis*/*trans* configurations on the conformational preferences of polyproline peptides.
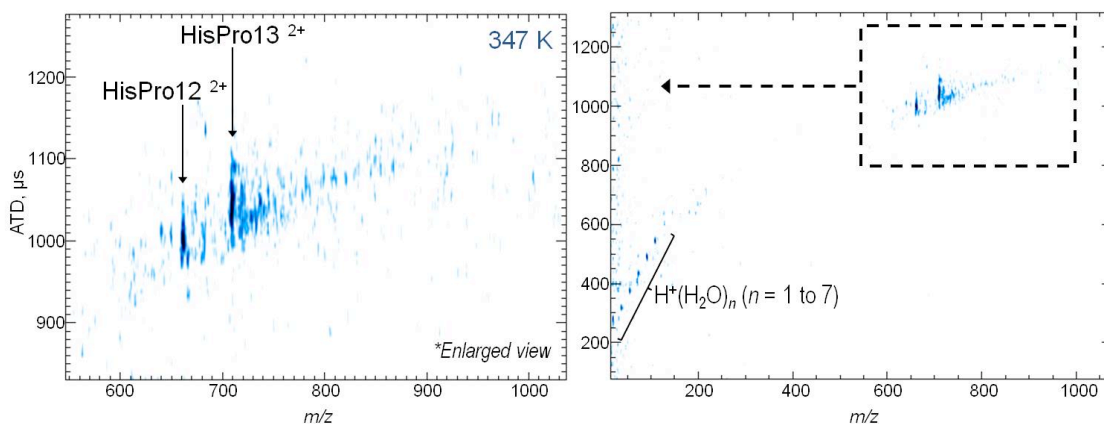
Figure 40. Two-dimensional contour plot of ATD versus *m/z* for [M + 2H]$^{2+}$ ions of HisPro13 sprayed from a solution of pure water with 0.1% formic acid at a heated capillary temperature of 347 K. HisPro12 [M + 2H]$^{2+}$ ions are observed in low abundance. The plot on the left contains an enlarged view of the highlighted region from the full plot on the right.
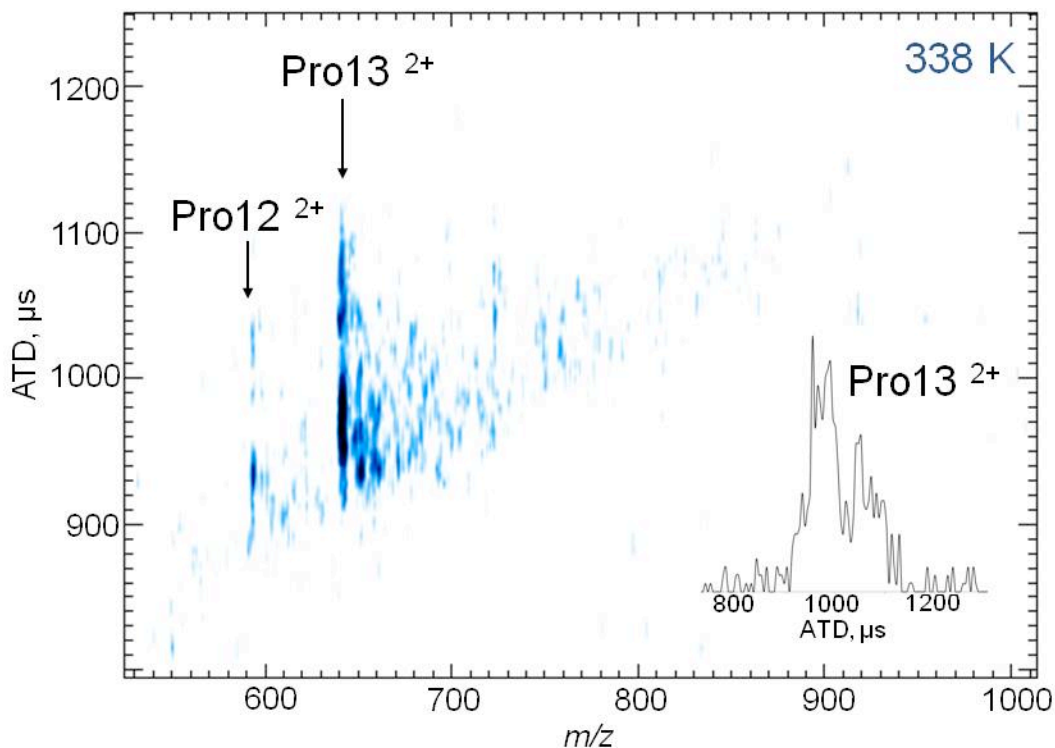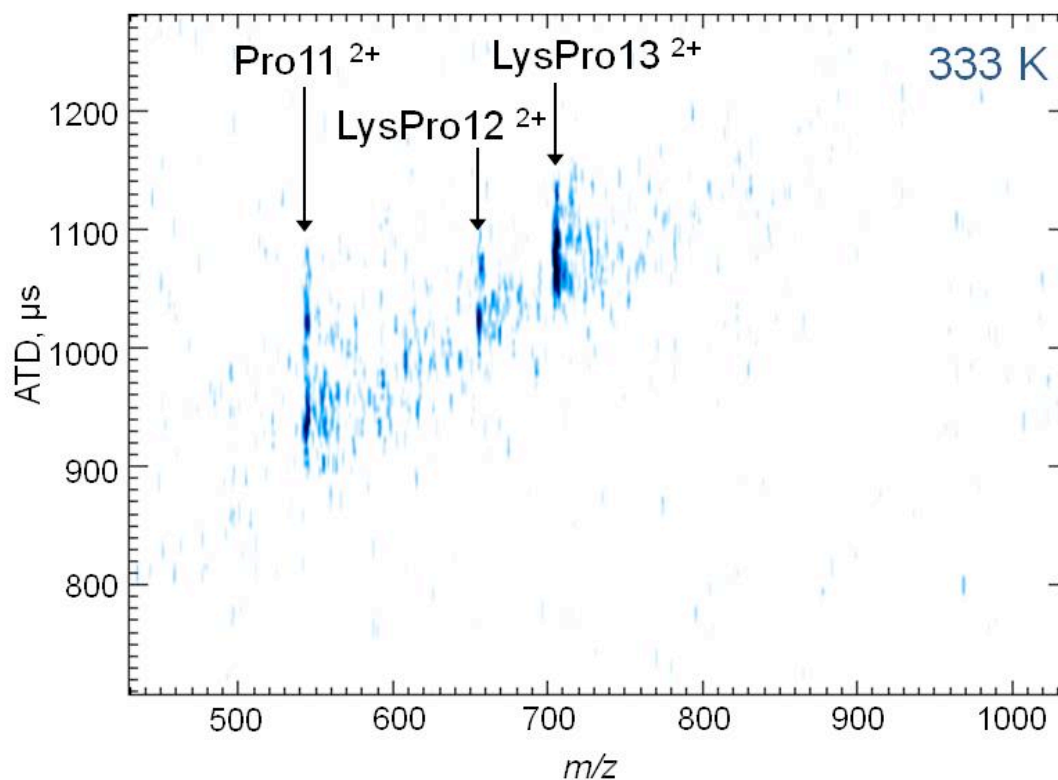
Figure 41. Two-dimensional contour plot of ATD versus *m/z* for [M + 2H]$^{2+}$ ions of LysPro13 sprayed from a solution of pure water with 0.1% formic acid at a heated capillary temperature of 333 K. LysPro12 and Pro11 [M + 2H]$^{2+}$ ions are observed in low abundance.

There are a number of proline-rich biologically relevant peptides and proteins that will undoubtedly be affected by *cis*/*trans* preferences. We have previously shown that conformer preferences for bradykinin (RPPGFSPFR) are highly dependent on *cis*/*trans* preferences of proline.[139,200] Mutation of the prolines with alanine indicated that multiple conformations of the ion resulted from specific combinations of *cis* and *trans* configurations of the three proline residues in the peptide. Alanine-for-proline amino acid mutations are used to lock the residue into a *trans* configuration while minimizing the steric effects imposed on the peptide ion structure. Conformational dependence on

proline was also revealed in studies of substance P (RPKPQQFFGLM-NH$_2$) mutant ions in which the prolines in positions 2 and 4 were mutated with alanine. In this case, it was shown that *cis/trans* isomerization of both proline residues contributed to the conformational heterogeneity of the [M + 3H]$^{3+}$ ion population.[102] Understanding the hydration behavior of these ions will elucidate more insight into the dynamics of *cis/trans* isomerization of proline residues in biomolecules and what affect this has on structural preferences.

7.4 Final Outlook

Cryo-IM-MS provides an unparalleled glimpse into the structural evolution of biomolecules as they undergo the final stages of desolvation during the transition from solution to the gas phase. Conformational changes that occur during these late stages of desolvation can be correlated to the number of water molecules adducted onto peptide or protein ions, providing new insights into the origins of gas-phase ion conformations generated during ESI. Collectively, the results presented herein illustrate that the evaporative process will vary for different peptides and proteins depending, most fundamentally, on amino acid sequence. Extension of these studies to other biological systems, both small and large, will serve to resolve lingering questions regarding the effects of hydration on structure and the intricate role water plays in regulating biological functionality.

REFERENCES

(1)   Langevin, P. *Ann. Chim. Phys.* **1903**, *28*, 289.

(2)   Thomson, J. J. *Science* **1913**, *37*, 360.

(3)   Bowers, M. T.; Kemper, P. R.; von Helden, G.; van Koppen, P. A. M. *Science* **1993**, *260*, 1446.

(4)   Jarrold, M. F. *J. Phys. Chem.* **1995**, *99*, 11.

(5)   Clemmer, D. E.; Hudgins, R. R.; Jarrold, M. F. *J. Am. Chem. Soc.* **1995**, *117*, 10141.

(6)   Jarrold, M. F. *Annu. Rev. Phys. Chem.* **2000**, *51*, 179.

(7)   Ruotolo, B. T.; Gillig, K. J.; Stone, E. G.; Russell, D. H. *J. Chromatogr. B* **2002**, *782*, 385.

(8)   Dugourd, P. H., R. R.; Clemmer, D. E.; Jarrold, M. F. *Rev. Sci. Instrum.* **1997**, *68*, 1122.

(9)   Wyttenbach, T.; Bowers, M. T. *Mod. Mass Spectrom.* **2003**, *225*, 207.

(10)   Giles, K. P., S. D.; Worthington, K. R.; Little, D.; Wildgoose, J. L.; Bateman, R. H. *Rapid Commun. Mass Spectrom.* **2004**, *18*, 2401.

(11)   Kurulugama, R. T. N., F. M.; Lee, S. J.; Valentine, D. E.; Clemmer, D. E. *J. Am. Soc. Mass Spectrom.* **2009**, *20*, 729.

(12)   Valentine, S. J. S., S. T.; Kurulugama, R. T.; Nachtigall, F. M.; Clemmer, D. E. *J. Am. Soc. Mass Spectrom.* **2009**, *20*, 738.

(13)   de la Mora, J. F. d. J., L.; Eichler, T.; Rosell, J. *Trends Anal. Chem.* **1998**, *17*, 328.

(14)   Guevremont, R. *Can. J. Anal. Sci. Spectrosc.* **2004**, *49*, 105.

(15)   Shvartsburg, A. A.; CRC Press: Boca Raton, FL, 2009.

(16)   Srebalus, C. A. L., J.; Marshall, W. S.; Clemmer, D. E. *Anal. Chem.* **1999**, *71*, 3918.

(17) Mason, E. A.; McDaniel, E. W. *Transport Properties of Ions in Gases*; John Wiley & Sons, Inc.: New York, NY, 1998.

(18) Mesleh, M. F.; Hunter, J. M.; Shvartsburg, A. A.; Schatz, G. C.; Jarrold, M. F. *J. Phys. Chem.* **1996**, *100*, 16082.

(19) Wyttenbach, T. v. H., G; Bowers, M. T. *J. Am. Chem. Soc.* **1996**, *118*, 8355.

(20) Wyttenbach, T.; Pierson, N. A.; Clemmer, D. E.; Bowers, M. T. *Annu. Rev. Phys. Chem.* **2014**, *65*, 175.

(21) Erikson, H. A. *Phys. Rev.* **1914**, *3*, 151.

(22) Chanin, L. M. B., M. A. *Phys. Rev.* **1957**, *106*, 473.

(23) Kemper, P. R. B., M. T. *J. Phys. Chem.* **1991**, *95*, 5134.

(24) May, J. C.; Russell, D. H. *J. Am. Soc. Mass Spectrom.* **2011**, *22*, 1134.

(25) Rokushika, S. H., H.; Baim, M. A.; Hill, H. H. *Anal. Chem.* **1985**, *57*, 1902.

(26) Silveira, J. A.; Servage, K. A.; Gamage, C. M.; Russell, D. H. *J. Phys. Chem. A* **2013**, *117*, 953.

(27) Karas, M.; Hillenkamp, F. *Anal. Chem.* **1988**, *60*, 2299.

(28) Fenn, J. B.; Mann, M.; Meng, C. K.; Wong, S. F.; Whitehouse, C. M. *Science* **1989**, *246*, 64.

(29) Fenn, J. B. *Angew. Chem. Int. Edit.* **2003**, *42*, 3871.

(30) Dole, M.; Mack, L. L.; Hines, R. L. *J. Chem. Phys.* **1968**, *49*, 2240.

(31) Kebarle, P.; Verkerk, U. H. *Mass Spectrom. Rev.* **2009**, *28*, 898.

(32) Konermann, L.; Ahadi, E.; Rodriguez, A. D.; Vahidi, S. *Anal. Chem.* **2013**, *85*, 2.

(33) Mack, L. L.; Kralik, P.; Rheude, A.; Dole, M. *J. Chem. Phys.* **1970**, *52*, 4977.

(34) Breuker, K.; McLafferty, F. W. *P Natl. Acad. Sci. U.S.A.* **2008**, *105*, 18145.

(35) Loo, J. A. *Mass Spectrom. Rev.* **1997**, *16*, 1.

(36) Ruotolo, B. T.; Robinson, C. V. *Curr. Opin. Chem. Biol.* **2006**, *10*, 402.

(37) Breuker, K.; Bruschweiler, S.; Tollinger, M. *Angew. Chem. Int. Edit.* **2011**, *50*, 873.

(38) Iribarne, J. V.; Thomson, B. A. *J. Chem. Phys.* **1976**, *64*, 2287.

(39) Nguyen, S.; Fenn, J. B. *Proc. Natl. Acad. Sci. U.S.A.* **2007**, *104*, 1111.

(40) Hall, Z.; Politis, A.; Bush, M. F.; Smith, L. J.; Robinson, C. V. *J. Am. Chem. Soc.* **2012**, *134*, 3429.

(41) Gidden, J. B., J. E.; Bowers, M. T. *J. Am. Chem. Soc.* **2001**, *123*, 5610.

(42) Lee, S. W.; Freivogel, P.; Schindler, T.; Beauchamp, J. L. *J. Am. Chem. Soc.* **1998**, *120*, 11758.

(43) Rizzo, T. R.; Stearns, J. A.; Boyarkin, O. V. *Int. Rev. Phys. Chem.* **2009**, *28*, 481.

(44) Nagornova, N. S.; Rizzo, T. R.; Boyarkin, O. V. *Science* **2012**, *336*, 320.

(45) Jarrold, M. F. *Acc. Chem. Res.* **1999**, *32*, 360.

(46) Wyttenbach, T.; Bowers, M. T. *Chem. Phys. Lett.* **2009**, *480*, 1.

(47) Rodriguez-Cruz, S. E.; Klassen, J. S.; Williams, E. R. *J. Am. Soc. Mass Spectrom.* **1997**, *8*, 565.

(48) Searcy, J. Q.; Fenn, J. B. *J. Chem. Phys.* **1974**, *61*, 5282.

(49) Shi, Z.; Ford, J. V.; Wei, S.; Castleman, A. W. *J. Chem. Phys.* **1993**, *99*, 8009.

(50) Miyazaki, M.; Fujii, A.; Ebata, T.; Mikami, N. *Science* **2004**, *304*, 1134.

(51) Shin, J. W.; Hammer, N. I.; Diken, E. G.; Johnson, M. A.; Walters, R. S.; Jaeger, T. D.; Duncan, M. A.; Christie, R. A.; Jordan, K. D. *Science* **2004**, *304*, 1137.

(52) Guan, S. M., A. G. *J. Am. Soc. Mass Spectrom.* **1996**, *7*, 101.

(53) Silveira, J. A.; Gamage, C. M.; Blase, R. C.; Russell, D. H. *Int. J. of Mass Spectrom.* **2010**, *296*, 36.

(54) May, J. C.; Russell, D. H. In *Ion Mobility Spectrometry-Mass Spectrometry: Theory and Applications*; Wilkins, C. L., Trimpin, S., Eds.; CRC Press: Boca Raton, FL, 2011.

(55)   Konig, S. F., H. M. *J. Am. Soc. Mass Spectrom.* **1998**, *9*, 814.

(56)   Sun, W., Texas A&M University, 2007.

(57)   Wu, C.-C.; Lin, C.-K.; Chang, H.-C.; Jiang, J.-C.; Kuo, J.-L.; Klein, M. L. *J. Chem. Phys.* **2005**, *122*.

(58)   Yeh, L. I.; Okumura, M.; Myers, J. D.; Price, J. M.; Lee, Y. T. *J. Chem. Phys.* **1989**, *91*, 7319.

(59)   Okumura, M.; Yeh, L. I.; Myers, J. D.; Lee, Y. T. *J. Phys. Chem.* **1990**, *94*, 3416.

(60)   Yeh, L. I.; Lee, Y. T.; Hougen, J. T. *J. Mol. Spectrosc.* **1994**, *164*, 473.

(61)   Jiang, J.-C.; Wang, Y.-S.; Chang, H.-C.; Lin, S. H.; Lee, Y. T.; Niedner-Schatteburg, G.; Chang, H.-C. *J. Am. Chem. Soc.* **2000**, *122*, 1398.

(62)   Headrick, J. M.; Diken, E. G.; Walters, R. S.; Hammer, N. I.; Christie, R. A.; Cui, J.; Myshakin, E. M.; Duncan, M. A.; Johnson, M. A.; Jordan, K. D. *Science* **2005**, *308*, 1765.

(63)   Holland, P. M.; Castleman, A. W. *J. Chem. Phys.* **1980**, *72*, 5984.

(64)   Nagashima, U.; Shinohara, H.; Nishi, N.; Tanaka, H. *J. Chem. Phys.* **1986**, *84*, 209.

(65)   Wei, S.; Shi, Z.; Castleman, A. W. *J. Chem. Phys.* **1991**, *94*, 3268.

(66)   Khan, A. *Chem. Phys. Lett.* **2000**, *319*, 440.

(67)   Hodges, M. P.; Wales, D. J. *Chem. Phys. Lett.* **2000**, *324*, 279.

(68)   Chang, T. M.; Prell, J. S.; Warrick, E. R.; Williams, E. R. *J. Am. Chem. Soc.* **2012**, *134*, 15805.

(69)   Chang, T. M.; Cooper, R. J.; Williams, E. R. *J. Am. Chem. Soc.* **2013**, *135*, 14821.

(70)   Cooper, R. J.; Chang, T. M.; Williams, E. R. *J. Phys. Chem. A* **2013**, *117*, 6571.

(71)   O'Brien, J. T.; Williams, E. R. *J. Am. Chem. Soc.* **2012**, *134*, 10228.

(72) Schindler, T.; Berg, C.; NiednerSchatteburg, G.; Bondybey, V. E. *Chem. Phys. Lett.* **1996**, *250*, 301.

(73) Wang, Y. S.; Tsai, C. H.; Lee, Y. T.; Chang, H. C.; Jiang, J. C.; Asvany, O.; Schlemmer, S.; Gerlich, D. *J. Phys. Chem. A* **2003**, *107*, 4217.

(74) Wong, R. L.; Paech, K.; Williams, E. R. *Int. J. Mass Spectrom.* **2004**, *232*, 59.

(75) Lin, C. K.; Wu, C. C.; Wang, Y. S.; Lee, Y. T.; Chang, H. C.; Kuo, J. L.; Klein, M. L. *Phys. Chem. Chem. Phys.* **2005**, *7*, 938.

(76) Mizuse, K.; Fujii, A. *J. Phys. Chem. A* **2012**, *116*, 4868.

(77) Fujii, A.; Mizuse, K. *Int. Rev. Phys. Chem.* **2013**, *32*, 266.

(78) Silveira, J. A.; Fort, K. L.; Kim, D.; Servage, K. A.; Pierson, N. A.; Clemmer, D. E.; Russell, D. H. *J. Am. Chem. Soc.* **2013**, *135*, 19147.

(79) Servage, K. A.; Silveira, J. A.; Fort, K. L.; Russell, D. H. *J. Phys. Chem. Lett.* **2014**, *5*, 1825.

(80) Shvartsburg, A. A.; Jarrold, M. F. *Chem. Phys. Lett.* **1996**, *261*, 86.

(81) Jarrold, M. F. http://www.indiana.edu/~nano/software.html

(82) Chang, H. C.; Wu, C. C.; Kuo, J. L. *Int. Rev. Phys. Chem.* **2005**, *24*, 553.

(83) Berry, R. S. *Chem. Rev.* **1993**, *93*, 2379.

(84) Agmon, N. *Chem. Phys. Lett.* **1995**, *244*, 456.

(85) Zwier, T. S. *Science* **2004**, *304*, 1119.

(86) Kulig, W.; Agmon, N. *J. Phys. Chem. B* **2013**, *118*, 278.

(87) Mizuse, K.; Fujii, A. *Phys. Chem. Chem. Phys.* **2011**, *13*, 7129.

(88) Heine, N.; Fagiani, M. R.; Rossi, M.; Wende, T.; Berden, G.; Blum, V.; Asmis, K. R. *J. Am. Chem. Soc.* **2013**, *135*, 8266.

(89) Bragg, W. H. *Proc. Phys. Soc. Lond.* **1922**, *34*, 0098.

(90) Shultz, M. J.; Tuan Hoang, V.; Meyer, B.; Bisson, P. *Acc. Chem. Res.* **2012**, *45*, 15.

(91)   Buch, V.; Sigurd, B.; Paul Devlin, J.; Buck, U.; Kazimirski, J. K. *Int. Rev. Phys. Chem.* **2004**, *23*, 375.

(92)   Pradzynski, C. C.; Forck, R. M.; Zeuch, T.; Slavíček, P.; Buck, U. *Science* **2012**, *337*, 1529.

(93)   Mizuse, K.; Mikami, N.; Fujii, A. *Angew. Chem. Int. Edit.* **2010**, *49*, 10119.

(94)   Wyttenbach, T.; Liu, D.; Bowers, M. T. *Int. J. Mass Spectrom.* **2005**, *240*, 221.

(95)   Barran, P. E.; Polfer, N. C.; Campopiano, D. J.; Clarke, D. J.; Langridge-Smith, P. R. R.; Langley, R. J.; Govan, J. R. W.; Maxwell, A.; Dorin, J. R.; Millar, R. P.; Bowers, M. T. *Int. J. Mass Spectrom.* **2005**, *240*, 273.

(96)   Wyttenbach, T.; Bowers, M. T. *Ann. Rev. Phys. Chem.* **2007**, *58*, 511.

(97)   Pierson, N. A.; Chen, L. X.; Valentine, S. J.; Russell, D. H.; Clemmer, D. E. *J. Am. Chem. Soc.* **2011**, *133*, 13810.

(98)   Gross, D. S.; Williams, E. R. *J. Am. Chem. Soc.* **1995**, *117*, 883.

(99)   Sterner, J. L.; Johnston, M. V.; Nicol, G. R.; Ridge, D. P. *J. Am. Soc. Mass Spectrom.* **1999**, *10*, 483.

(100) Skinner, O. S.; McLafferty, F. W.; Breuker, K. *J. Am. Soc. Mass Spectrom.* **2012**, *23*, 1011.

(101) Wyttenbach, T.; Bowers, M. T. *J. Phys. Chem. B* **2011**, *115*, 12266.

(102) Fort, K. L.; Silveira, J. A.; Pierson, N. A.; Servage, K. A.; Clemmer, D. E.; Russell, D. H. *J. Phys. Chem. B* **2014**, *118*, 14336.

(103) Servage, K. A.; Silveira, J. A.; Fort, K. L.; Russell, D. H. *J. Phys. Chem. B* **2015**, *119*, 4693.

(104) Liu, D.; Wyttenbach, T.; Barran, P. E.; Bowers, M. T. *J. Am. Chem. Soc.* **2003**, *125*, 8458.

(105) Misaizu, F.; Sanekata, M.; Fuke, K.; Iwata, S. *J. Chem. Phys.* **1994**, *100*, 1161.

(106) Robertson, W. H.; Diken, E. G.; Price, E. A.; Shin, J.-W.; Johnson, M. A. *Science* **2003**, *299*, 1367.

(107) Walters, R. S.; Pillai, E. D.; Duncan, M. A. *J. Am. Chem. Soc.* **2005**, *127*, 16599.

(108) Cooper, T. E.; O'Brien, J. T.; Williams, E. R.; Armentrout, P. B. *J. Phys. Chem. A* **2010**, *114*, 12646.

(109) O'Brien, J. T.; Williams, E. R. *J. Phys. Chem. A* **2011**, *115*, 14612.

(110) Wyttenbach, T.; Paizs, B.; Barran, P.; Breci, L.; Liu, D.; Suhai, S.; Wysocki, V. H.; Bowers, M. T. *J. Am. Chem. Soc.* **2003**, *125*, 13768.

(111) Lemoff, A. S.; Bush, M. F.; Wu, C.-C.; Williams, E. R. *J. Am. Chem. Soc.* **2005**, *127*, 10276.

(112) Drayß, M. K.; Blunk, D.; Oomens, J.; Polfer, N.; Schmuck, C.; Gao, B.; Wyttenbach, T.; Bowers, M. T.; Schäfer, M. *Int. J. Mass Spectrom.* **2009**, *281*, 97.

(113) Gao, B.; Wyttenbach, T.; Bowers, M. T. *J. Phys. Chem. B* **2009**, *113*, 9995.

(114) Meot-Ner, M.; Field, F. H. *J. Am. Chem. Soc.* **1974**, *96*, 3168.

(115) Klassen, J. S.; Blades, A. T.; Kebarle, P. *J. Phys. Chem.* **1995**, *99*, 15509.

(116) Lemoff, A. S.; Bush, M. F.; Williams, E. R. *J. Am. Chem. Soc.* **2003**, *125*, 13576.

(117) Ye, S. J.; Moision, R. M.; Armentrout, P. B. *Int. J. Mass Spectrom.* **2005**, *240*, 233.

(118) Wincel, H. *J. Phys. Chem. A* **2007**, *111*, 5784.

(119) Gao, B.; Wyttenbach, T.; Bowers, M. T. *J. Am. Chem. Soc.* **2009**, *131*, 4695.

(120) Donald, W. A.; Leib, R. D.; Demireva, M.; Williams, E. R. *J. Am. Chem. Soc.* **2011**, *133*, 18940.

(121) Klassen, J. S.; Blades, A. T.; Kebarle, P. *J. Am. Chem. Soc.* **1994**, *116*, 12075.

(122) Blades, A. T.; Klassen, J. S.; Kebarle, P. *J. Am. Chem. Soc.* **1996**, *118*, 12437.

(123) Bush, M. F.; Prell, J. S.; Saykally, R. J.; Williams, E. R. *J. Am. Chem. Soc.* **2007**, *129*, 13544.

(124) Khan, A. *Chem. Phys. Lett.* **2001**, *338*, 201.

(125) Diken, E. G.; Hammer, N. I.; Johnson, M. A.; Christie, R. A.; Jordan, K. D. *J. Chem. Phys.* **2005**, *123*, 164309.

(126) Douady, J.; Calvo, F.; Spiegelman, F. *J. Chem. Phys.* **2008**, *129*, 154305.

(127) Willow, S. Y.; Singh, N. J.; Kim, K. S. *J. Chem. Theory Comput.* **2011**, *7*, 3461.

(128) Demireva, M.; O'Brien, J. T.; Williams, E. R. *J. Am. Chem. Soc.* **2012**, *134*, 11216.

(129) Yang, X.; Fu, Y.-J.; Wang, X.-B.; Slavíček, P.; Mucha, M.; Jungwirth, P.; Wang, L.-S. *J. Am. Chem. Soc.* **2004**, *126*, 876.

(130) Jahangiri, S.; Legris-Falardeau, V.; Peslherbe, G. H. *Chem. Phys. Lett.* **2015**, *621*, 85.

(131) Servage, K. A.; Fort, K. L.; Silveira, J. A.; Shi, L.; Clemmer, D. E.; Russell, D. H. *J. Am. Chem. Soc.* **2015**, *137*, 8916.

(132) Heck, A. J. R.; van den Heuvel, R. H. H. *Mass Spectrom. Rev.* **2004**, *23*, 368.

(133) Hall, Z.; Robinson, C. V. *J. Am. Soc. Mass Spectrom.* **2012**, *23*, 1161.

(134) Fort, K. L.; Silveira, J. A.; Russell, D. H. *Anal. Chem.* **2013**, *85*, 9543.

(135) Silveira, J. A.; Jeon, J.; Gamage, C. M.; Pai, P.-J.; Fort, K. L.; Russell, D. H. *Anal. Chem.* **2012**, *84*, 2818.

(136) Valentine, S. J.; Counterman, A. E.; Clemmer, D. E. *J. Am. Soc. Mass Spectrometry* **1999**, *10*, 1188.

(137) Dupradeau, F.-Y.; Pigache, A.; Zaffran, T.; Savineau, C.; Lelong, R.; Grivel, N.; Lelong, D.; Rosanski, W.; Cieplak, P. *Phys. Chem. Chem. Phys.* **2010**, *12*, 7821.

(138) Chen, L. X.; Shao, Q.; Gao, Y. Q.; Russell, D. H. *J. Phys. Chem. A* **2011**, *115*, 4427.

(139) Pierson, N. A.; Chen, L. X.; Russell, D. H.; Clemmer, D. E. *J. Am. Chem. Soc.* **2013**, *135*, 3186.

(140) Auge, S.; Bersch, B.; Tropis, M.; Milon, A. *Biopolymers* **2000**, *54*, 297.

(141) Gayen, A.; Goswami, S. K.; Mukhopadhyay, C. *Biochim. Biophys. Acta-Biomembr.* **2011**, *1808*, 127.

(142) Mihalca, R.; Kleinnijenhuis, A. J.; McDonnell, L. A.; Heck, A. J. R.; Heeren, R. M. A. *J. Am. Soc. Mass Spectrom.* **2004**, *15*, 1869.

(143) Gill, A. C.; Jennings, K. R.; Wyttenbach, T.; Bowers, M. T. *Int. J. Mass Spectrom.* **2000**, *195–196*, 685.

(144) Prell, J. S.; Chang, T. M.; O'Brien, J. T.; Williams, E. R. *J. Am. Chem. Soc.* **2010**, *132*, 7811.

(145) Prell, J. S.; Correra, T. C.; Chang, T. M.; Biles, J. A.; Williams, E. R. *J. Am. Chem. Soc.* **2010**, *132*, 14733.

(146) Garand, E.; Kamrath, M. Z.; Jordan, P. A.; Wolk, A. B.; Leavitt, C. M.; McCoy, A. B.; Miller, S. J.; Johnson, M. A. *Science* **2012**, *335*, 694.

(147) Steinberg, M. Z.; Elber, R.; McLafferty, F. W.; Gerber, R. B.; Breuker, K. *Chem. Bio. Chem.* **2008**, *9*, 2417.

(148) Schindler, T.; Berg, C.; Niednerschatteburg, G.; Bondybey, V. E. *Chem. Phys. Lett.* **1994**, *229*, 57.

(149) Kebarle, P. *J. Mass Spectrom.* **2000**, *35*, 804.

(150) Iavarone, A. T.; Williams, E. R. *J. Am. Chem. Soc.* **2003**, *125*, 2319.

(151) Silveira, J. A.; Ridgeway, M. E.; Park, M. A. *Anal. Chem.* **2014**, *86*, 5624.

(152) Schnier, P.; Gross, D.; Williams, E. *J. Am. Soc. Mass Spectrom.* **1995**, *6*, 1086.

(153) Stephenson, J. L.; McLuckey, S. A. *J. Am. Chem. Soc.* **1996**, *118*, 7390.

(154) Williams, E. R. *J. Mass Spectrom.* **1996**, *31*, 831.

(155) Pitteri, S. J.; McLuckey, S. A. *Mass Spectrom. Rev.* **2005**, *24*, 931.

(156) Bowers, J. J.; Hodges, B. D. M.; Saad, O. M.; Leary, J. A.; McLuckey, S. A. *Int. J. Mass Spectrom.* **2008**, *276*, 153.

(157) McLuckey, S. A.; Stephenson, J. L. *Mass Spectrom. Rev.* **1998**, *17*, 369.

(158) Winger, B. E.; Lightwahl, K. J.; Smith, R. D. *J. Am. Soc. Mass Spectrom.* **1992**, *3*, 624.

(159) Hunter, E. P. L.; Lias, S. G. *J. Phys. Chem. Ref. Data* **1998**, *27*, 413.

(160) Wolf, J. F.; Staley, R. H.; Koppel, I.; Taagepera, M.; McIver, R. T.; Beauchamp, J. L.; Taft, R. W. *J. Am. Chem. Soc.* **1977**, *99*, 5417.

(161) Schroeder, O. E.; Andriole, E. J.; Carver, K. L.; Colyer, K. E.; Poutsma, J. C. *The J. Phys. Chem. A* **2003**, *108*, 326.

(162) Ladbury, J. E. *Chem. Biol.* **1996**, *3*, 973.

(163) Bogan, A. A.; Thorn, K. S. *J. Mol. Biol.* **1998**, *280*, 1.

(164) Papoian, G. A.; Ulander, J.; Eastwood, M. P.; Luthey-Schulten, Z.; Wolynes, P. G. *Proc. Natl. Acad. Sci. U.S.A.* **2004**, *101*, 3352.

(165) Levy, Y.; Onuchic, J. N. *Proc. Natl. Acad. Sci. U.S.A.* **2004**, *101*, 3325.

(166) Levy, Y.; Onuchic, J. N. *Ann. Rev. Biophys. Biomole. Struct.* **2006**, *35*, 389.

(167) Chandler, D. *Nature* **2002**, *417*, 491.

(168) Hummer, G.; Tokmakoff, A. *J. Chem. Phys.* **2014**, *141*, 22D101.

(169) Halle, B. *Philos. Trans. R. Soc. London, Ser. B* **2004**, *359*, 1207.

(170) Rodier, F.; Bahadur, R. P.; Chakrabarti, P.; Janin, J. *Proteins* **2005**, *60*, 36.

(171) Nucci, N. V.; Pometun, M. S.; Wand, A. J. *J. Am. Chem. Soc.* **2011**, *133*, 12326.

(172) Duboué-Dijon, E.; Laage, D. *J. Chem. Phys.* **2014**, *141*, 22D529.

(173) Pal, S. K.; Zewail, A. H. *Chem. Rev.* **2004**, *104*, 2099.

(174) Servage, K. A.; Silveira, J. A.; Fort, K. L.; Clemmer, D. E.; Russell, D. H. *J. Phys. Chem. Lett.* **2015**, *6*, 4947.

(175) Hershko, A.; Ciechanover, A. *Ann. Rev. Biochem.* **1998**, *67*, 425.

(176) Winget, J. M.; Mayor, T. *Mol. Cell* **2010**, *38*, 627.

(177) Lenkinski Re Fau - Chen, D. M.; Chen Dm Fau - Glickson, J. D.; Glickson Jd Fau - Goldstein, G.; G, G. *Biochim. Biophys. Acta.* **1977**, *494*, 126.

(178) Vijay-Kumar S Fau - Bugg, C. E.; Bugg Ce Fau - Cook, W. J.; WJ, C. *J. Mol. Biol.* **1987**, *194*, 531.

(179) Shi, H.; Atlasevich, N.; Merenbloom, S.; Clemmer, D. *J. Am. Soc. Mass Spectrom.* **2014**, *25*, 2000.

(180) Wilkinson, K. D.; Mayer, A. N. *Arch. Biochem. Biophys.* **1986**, *250*, 390.

(181) Harding, M. M.; Williams, D. H.; Woolfson, D. N. *Biochem.* **1991**, *30*, 3120.

(182) Chen, S.-H.; Russell, D. *J. Am. Soc. Mass Spectrom.* **2015**, *26*, 1433.

(183) Shi, H.; Clemmer, D. E. *J. Phys. Chem. B* **2014**, *118*, 3498.

(184) Shi, H.; Pierson, N. A.; Valentine, S. J.; Clemmer, D. E. *J. Phys. Chem. B* **2012**, *116*, 3344.

(185) Liu, Z.; Zhang, W.-P.; Xing, Q.; Ren, X.; Liu, M.; Tang, C. *Angew. Chem. Int. Ed.* **2012**, *51*, 469.

(186) Vallone, B.; Miele, A. E.; Vecchini, P.; Chiancone, E.; Brunori, M. *Proc. Natl. Acad. Sci. U.S.A.* **1998**, *95*, 6103.

(187) Peters, J. M.; Harris, J. R.; Finley, D. *Ubiquitin and the Biology of the Cell*; Plenum Press: New York, 1998.

(188) Cooper, R. J.; Heiles, S.; DiTucci, M. J.; Williams, E. R. *J. Phys. Chem. A* **2014**, *118*, 5657.

(189) Heiles, S.; Cooper, R. J.; DiTucci, M. J.; Williams, E. R. *Chem. Sci.* **2015**, *6*, 3420.

(190) Sloan, E. D. *Nature* **2003**, *426*, 353.

(191) Xie, W. J.; Gao, Y. Q. *J. Phys. Chem. Lett.* **2013**, *4*, 4247.

(192) Merenbloom, S. I.; Flick, T. G.; Daly, M. P.; Williams, E. R. *J. Am. Soc. Mass Spectrom.* **2011**, *22*, 1978.

(193) Paterova, J.; Rembert, K. B.; Heyda, J.; Kurra, Y.; Okur, H. I.; Liu, W. S. R.; Hilty, C.; Cremer, P. S.; Jungwirth, P. *J. Phys. Chem. B* **2013**, *117*, 8150.

(194) Jungwirth, P.; Winter, B. In *Ann. Rev. Phys. Chem.*; Annual Reviews: Palo Alto, 2008; Vol. 59, p 343.

(195) Xiao, C.; Perez, L. M.; Russell, D. H. *Analyst* **2015**, *140*, 6933.

(196) Counterman, A. E.; Clemmer, D. E. *J. Phys. Chem. B* **2004**, *108*, 4885.

(197) Shi, L. Q.; Holliday, A. E.; Shi, H. L.; Zhu, F. F.; Ewing, M. A.; Russell, D. H.; Clemmer, D. E. *J. Am. Chem. Soc.* **2014**, *136*, 12702.

(198) Shi, L.; Holliday, A. E.; Glover, M. S.; Ewing, M. A.; Russell, D. H.; Clemmer, D. E. *J. Am. Soc. Mass Spectrom.* **2016**, *27*, 22.

(199) Shi, L.; Holliday, A. E.; Bohrer, B. C.; Kim, D.; Servage, K. A.; Russell, D. H.; Clemmer, D. E. *J. Am. Soc. Mass Spectrom.* **2016**, *27*, 1037.

(200) Pierson, N. A.; Clemmer, D. E. *Int. J. Mass Spectrom.* **2015**, *377*, 646.